
Design and analysis of parachute triggering algorithms for re-entry vehicles

Master thesis report
Barend Ording
1147153

Daily Supervisors

Ir. G.F. Brouwer
M. Sudars MSc.Ing

TU Delft
Thales Alenia Space Italy

Exam Committee

Prof. Dr. E.K.A. Gill
Ir. G.F. Brouwer
M. Sudars MSc.Ing
Ir. B.T.C Zandbergen
Dr. Ir. E. Mooij

TU Delft
TU Delft
Thales Alenia Space Italy
TU Delft
TU Delft



Delft University of Technology

Faculty of Aerospace Engineering
Chair of Space Systems Engineering

This page has been left blank intentionally

Preface

This report is the thesis work of Barend Ording. The thesis is a required task in order to obtain a Master of Science degree at Delft University of Technology. The thesis started half December 2009 and is finished after a colloquium and a thesis defense at August 31st.

This report reflects a theoretical investigation carried out at Thales Alenia Space Italy in cooperation with TU Delft in order to improve the Descent and Landing System (DLS) triggering algorithms for ballistic flight and to set a baseline for a lifting re-entry flight in order to support the existing and upcoming ESA EXPERT and IXV re-entry missions. This investigation elaborates on the expected accuracy of DLS triggering methods for a ballistic and a lifting re-entry mission and investigates whether the landing footprint can be reduced by changing the moment of the parachute deployment.

The results of this investigation were presented at the AIAA Astrodynamics Specialist conference, which was held in Toronto from 2 to 5 August 2010. A paper was made which is included in the proceedings of this conference.

Summary

Most re-entry vehicles utilize a Descent and Landing System (DLS) for a safe descent through the lowest part of the atmosphere. It usually requires deployment in a certain suitable range of flight conditions, which has to be estimated by limited means of navigation. The investigation performed is a comparison of currently used trigger methods and triggering algorithms which are based on correlation between in-flight measurements and the DLS triggering conditions for a ballistic re-entry vehicle, where the correlations have been extracted by multiple Monte Carlo campaigns. This approach gives an improvement of the estimation of the deployment conditions of a factor of two over direct measurements of the Mach number. The Mach number is determined to be the most critical parameter for the parachute deployment, because its opening range is the smallest compared to the dynamic pressure and the altitude.

Furthermore a sensor sensitivity analysis is performed for a lifting entry trajectory in order to support an upcoming ESA re-entry mission. The velocity drift appears to be the dominant dispersion by a factor ten for the Mach estimation, if the Mach estimation is performed by estimating the drag using axial deceleration measurements. Such a method is the preferred method for the estimation of the deployment conditions, because it has an expected error of less than Mach 0.1. For the lifting-re-entry mission, a strategy was developed to have redundant parachute deployment triggering if a certain system on the vehicle fails. This strategy involves the use of an Inertial Measurement Unit, Global Positioning System measurements and as last resort, a static pressure probe. Furthermore it appeared that the vehicle can estimate its state using no inputs from the guidance navigation and control system for four minutes.

Finally a case study has been performed to investigate the possibility to reduce the footprint by a dynamic parachute opening window. This has found to be ineffective on Earth, but could be effective for Mars re-entry using a parachute able to deploy beyond Mach 2.5, which would reduce the footprint 15 to 25 kilometers if the NASA MER missions are used as a reference; this would be a reduction of 30 to 50 % of the footprints of current missions. A higher opening velocity is already desired in order to be able to land on the Martian highlands. Modified parachute designs can be developed to incorporate both benefits.

Table of contents

| | |
|--|----|
| Preface | 4 |
| Summary | 5 |
| Table of contents | 6 |
| List of abbreviations | 8 |
| List of symbols | 8 |
| List of figures | 8 |
| List of tables | 11 |
| Introduction | 13 |
| 1 Background for parachute triggering for re-entry vehicles | 15 |
| 1.1 Investigation plan | 15 |
| 1.2 Typical re-entry characteristics | 16 |
| 1.2.1 The choice between a ballistic or lifting trajectory | 18 |
| 1.3 Parachute triggering opening window | 18 |
| 1.3.1 Measured parameters | 19 |
| 1.3.2 Parachute stages | 19 |
| 1.3.3 Parachute types | 19 |
| 1.3.4 ARD example parachutes sequence | 20 |
| 1.3.5 Premature triggering prevention | 21 |
| 1.4 Sensors | 22 |
| 1.4.1 GPS | 22 |
| 1.4.2 Pressure sensors | 22 |
| 1.4.3 Timer | 23 |
| 1.4.4 Inertial measurement unit (IMU) | 23 |
| 1.4.5 Temperature | 23 |
| 1.4.6 Angle of attack measurement | 23 |
| 1.5 Modeling | 24 |
| 1.5.1 Monte Carlo Analysis | 24 |
| 1.5.2 Defining the uncertainties | 24 |
| 1.5.3 The atmosphere models | 25 |
| 1.5.4 Statistical mathematics used | 28 |
| 1.6 Table of historical data | 28 |
| 2 Algorithm analysis for a ballistic re-entry | 29 |
| 2.1 Algorithm development procedure | 29 |
| 2.1.1 Correlated algorithm flow diagram | 29 |
| 2.2 Test case scenario | 30 |
| 2.2.1 The nominal ballistic trajectory | 33 |
| 2.3 Flight path dispersions | 33 |
| 2.4 Selection of characteristic points for triggering algorithms | 36 |
| 2.4.1 Time measurement | 36 |
| 2.4.2 G-load measurements | 37 |
| 2.4.3 Pressure | 39 |
| 2.4.4 Static pressure | 40 |
| 2.4.5 Dynamic and total pressure | 41 |
| 2.5 Sensitivity of the points of interest | 43 |
| 2.5.1 Specific contributions of the uncertainties | 43 |

| | | |
|-------|---|-----|
| 2.5.2 | Correlations of the algorithms | 45 |
| 2.6 | Performance of the algorithms | 47 |
| 2.7 | High fidelity modeling | 52 |
| 2.7.1 | Simulink flow diagram | 52 |
| 2.7.2 | Nominal and off-nominal trajectory high fidelity modeling results | 53 |
| 2.8 | Conclusions on the ballistic re-entry algorithm development | 55 |
| 3 | The lifting re-entry case | 57 |
| 3.1 | The lifting re-entry flight path | 57 |
| 3.2 | Flight path dispersions | 60 |
| 3.3 | Measurements used | 61 |
| 3.3.1 | Quick measurement system trade-off | 62 |
| 3.3.2 | Drag derived measurements | 64 |
| 3.3.3 | Constant temperature Mach estimation | 65 |
| 3.3.4 | Altitude estimation | 66 |
| 3.4 | Main error sources | 68 |
| 3.4.1 | IMU sensitivity | 68 |
| 3.4.2 | Calculation of the error due to wind | 70 |
| 3.4.3 | Alternative estimation of the velocity | 71 |
| 3.5 | Nominal trajectory Mach estimation results | 72 |
| 3.5.1 | Monte Carlo results | 73 |
| 3.6 | Off-nominal | 73 |
| 3.6.1 | In case of total loss of the IMU | 74 |
| 3.6.2 | Static pressure triggering | 75 |
| 3.6.3 | Ballistic re-entry | 76 |
| 3.7 | Parachute triggering logic | 77 |
| 3.8 | Conclusions | 79 |
| 4 | Footprint reduction | 80 |
| 4.1.1 | Applicability for footprint reduction study | 80 |
| 4.1.2 | Footprint reduction deployment control | 80 |
| 4.1.3 | Modeling of the parachute in FMST | 81 |
| 4.2 | Earth ballistic re-entry footprint reduction | 81 |
| 4.3 | MER footprint reduction | 83 |
| 4.3.1 | MER footprint reconstruction | 83 |
| 4.3.2 | Footprint reduction | 90 |
| 4.3.3 | Footprint reduction limited on parachute capabilities | 91 |
| 4.3.4 | Footprint reduction using g-force correlations only | 93 |
| 4.4 | Conclusions | 98 |
| 5 | Conclusions | 99 |
| 6 | Recommendations | 102 |
| | Bibliography | 103 |
| | Appendix A, Matlab algorithms and FMST data extraction | 105 |

List of abbreviations

| | |
|----------|---|
| AoA | = Angle of Attack |
| ARD | = Advanced Re-entry Demonstrator |
| CFD | = Computational Fluid Dynamics |
| DOF | = Degree Of Freedom |
| DLS | = Descent and Landing System |
| EXPERT | = European Experimental Reentry Testbed |
| FMST | = Flight Mechanics Simulation Tool |
| GNC | = Guidance Control and Navigation |
| GPS | = Global Positioning System |
| GRAM | = Global Reference Atmospheric Model |
| IMU | = Inertial Measurement Unit |
| IXV | = Intermediate eXperimental Vehicle |
| MC | = Monte Carlo |
| MER | = Mars Exploration rover |
| PDF | = Probability Density Function |
| TPS | = Thermal Protection System |
| TU Delft | = Technical University Delft |

List of symbols

| | |
|------------|---|
| C_A | = Longitudinal axis aerodynamic force coefficient |
| C_D | = Aerodynamic force coefficient |
| D | = Drag force |
| d | = Derivative |
| H | = Altitude |
| M | = Mach number |
| m | = Vehicle mass |
| P_{dyn} | = Dynamic pressure |
| P_{stat} | = Static pressure |
| R | = Specific gas constant |
| R | = Coefficient of determination |
| S_{ref} | = Vehicle reference surface |
| T | = Temperature |
| V | = Vehicle velocity |
| Γ | = Longitudinal non-gravitational acceleration |
| γ | = Specific heat ratio |
| ρ | = Air density |
| σ | = Standard deviation |

List of figures

Figure 1. *Re-entry profiles of a ballistic and a lifting re-entry on Earth and a ballistic re-entry on Mars.* 17

Figure 2. *Mach numbers of a ballistic and a lifting re-entry on Earth and a ballistic re-entry on Mars.* 18

| | |
|--|----|
| Figure 3. A lifting parafoil carrying the X-38 vehicle is displayed on the left, a ballistic parachute carrying a Soyuz capsule on the right ¹⁹ . | 20 |
| Figure 4. The ARD parachute deployment sequence. | 21 |
| Figure 5. Uncertainty bounds of temperature. Comparison between GRAM derived uncertainties and Russian atmospheric uncertainties FOCT T24631-81. | 25 |
| Figure 6. Uncertainty bounds of density. Comparison between GRAM derived uncertainties and Russian atmospheric uncertainties FOCT T24631-81. | 26 |
| Figure 7. Monte Carlo example of 100 US-76 standard atmospheres and the GRAM derived uncertainty model. | 26 |
| Figure 8. Monte Carlo example of 100 US-76 standard atmospheres and the Russian FOCT T24631-81 uncertainty model. | 27 |
| Figure 9. Monte Carlo example of 100 Martian atmospheres and the GRAM derived uncertainty model. | 27 |
| Figure 10. Algorithm development flow diagram | 29 |
| Figure 11. Correlated algorithm functional flow diagram | 30 |
| Figure 12. The EXPERT re-entry vehicle ²⁰ . | 30 |
| Figure 13. The parachute opening constraints. | 32 |
| Figure 14. The Earth ballistic re-entry profiles. All y-axis values are multiplied by the value provided in the legend. | 33 |
| Figure 15. Trajectory dispersions by Monte Carlo simulation | 34 |
| Figure 16. Dispersion discrepancy, created by the transition of a Gaussian to a uniform uncertainty distribution. | 35 |
| Figure 17. Pressure dispersions by Monte Carlo simulation. | 36 |
| Figure 18. The g-load curve of the nominal ballistic re-entry trajectory with points of investigation. | 37 |
| Figure 19. Correlation example of the time of occurrence of the g-load peak with the initial flight path angle. | 39 |
| Figure 20. The static pressure curve of the nominal ballistic re-entry trajectory with points of investigation | 40 |
| Figure 21. The dynamic pressure curve of the nominal ballistic re-entry trajectory with its point of investigation. | 41 |
| Figure 22. The total pressure curve of the nominal ballistic re-entry trajectory with points of investigation. | 42 |
| Figure 23. Correlations of the algorithms to the dispersions. Measured values are on the y-axis, desired outputs for each specific measurement principle are on the x-axis. | 45 |
| Figure 24. Parachute trigger Mach dispersions. On the left side the Mach dispersion of a single threshold trigger is shown, the right side shows the dispersion of a correlated algorithm | 47 |
| Figure 25. Parachute trigger altitude dispersions. On the left side the altitude dispersion of a single threshold trigger is shown, the right side shows the dispersion of a correlated algorithm. | 48 |
| Figure 26. Correlation plots of the parachute opening windows of dynamic pressure and altitude. | 50 |
| Figure 27. Correlation plots of the parachute opening windows of dynamic pressure and Mach number. | 51 |
| Figure 28. Flow diagram of a high fidelity g-slope triggering algorithm. | 52 |

| | |
|---|----|
| Figure 29. Mach dispersion as a function of the sensor's noise, with and without the use of a filter. | 53 |
| Figure 30. Results of the high fidelity modeling of g-load based triggering systems. | 54 |
| Figure 31. Results of the high fidelity modeling of a static pressure triggering mechanism (left) and a drag derived measurement system (right). | 55 |
| Figure 32. The Horus-2b re-entry vehicle ⁷ . | 57 |
| Figure 33. The Earth lifting re-entry profiles. All y-axis values are multiplied by the value provided in the legend. | 58 |
| Figure 34. G-load dispersions by Monte Carlo simulation. | 61 |
| Figure 35. Pressure dispersions by Monte Carlo simulation. | 61 |
| Figure 36. Total g-load curve (left) and g-load curves separated in components (right). | 64 |
| Figure 37. Simulink drag derived Mach estimation scheme. | 65 |
| Figure 38. Altitude estimation by DDA. The blue line is the as-flown trajectory; the green line indicates the measured altitude. | 67 |
| Figure 39. C_A modeling discrepancy between the simulated C_A and the simulated measured C_A . | 67 |
| Figure 40. Relative error ratios of the Mach number as a function of the velocity drift (left) and the temperature uncertainty. | 68 |
| Figure 41. Mach dispersion as a function of the velocity drift. | 70 |
| Figure 42. Velocity estimation using a drag derived measurement and a static pressure probe. | 71 |
| Figure 43. Lifting re-entry Mach profile with Mach estimation methods. Both Mach estimation profiles will converge to an acceptable error below Mach 5, which is more than sufficient for parachute deployment. | 72 |
| Figure 44. 10 Monte Carlo trajectories (upper left) and their measured values (lower left) The Mach estimation dispersion at Mach 1.6 is short in the histogram (right). | 73 |
| Figure 45. Histogram of the Mach dispersion when static pressure triggering is used. | 76 |
| Figure 46. Drag derived Mach estimation of a ballistic re-entry for a lifting re-entry vehicle. | 76 |
| Figure 47. Mach estimation system indicating redundancy. | 77 |
| Figure 48. Parachute triggering system at logics level. | 78 |
| Figure 49. Terminal trajectories with parachute deployment at different Mach numbers. | 82 |
| Figure 50. Footprint reduction capability as a function of the parachute opening window. | 83 |
| Figure 51. Exploded view of the MER re-entry vehicle ²¹ . | 84 |
| Figure 52. The MER ballistic re-entry profiles. All y-axis values are multiplied by the value provided in the legend. | 86 |
| Figure 53. Parachute phase quadratic regression modeling. | 87 |
| Figure 54. Footprint contributions of different types of uncertainties. | 88 |
| Figure 55. Spirit footprint as defined by ref ⁵ . | 89 |
| Figure 56. MER A (Spirit) reconstructed footprint together with the real and the planned landing site. | 90 |
| Figure 57. MER B (Opportunity) reconstructed footprint together with the real and the planned landing site. | 90 |
| Figure 58. Footprint reduction possible using qualified Viking parachutes. | 92 |

| | |
|---|----|
| Figure 59. Footprint reduction possible, using a parachute capable of deployment up till Mach 3. | 92 |
| Figure 60. Footprint reduction possible as a function of the maximum parachute deployment Mach number and the Mach opening window. | 93 |
| Figure 61. Correlations of the selected g-load thresholds to the downrange and the desired deployment conditions. R^2 vales are: 0.81 ,0.89 0.92,0.87 from upper left to right and down left to right respectively. | 95 |
| Figure 62. Footprint reduction using a parachute capable of deployment up till Mach 3 and g-load correlations only. | 95 |
| Figure 63. 2D histogram of the landing site dispersion for nominal deployment only (upper) and using g a parachute capable of deployment up till Mach 3 and g-load correlations only (lower). | 96 |
| Figure 64. Mach dispersions of the g-load correlated deployments. The three dispersions clearly indicate the 3 separate instants of deployment, depending on the required downrange. | 97 |
| Figure 65. Altitude dispersions of the g-load correlated deployments. The altitude dispersion at the deployment is around 1.7 Km 3σ for of all three different Mach numbers. | 97 |
| Figure 66. Dynamic pressure dispersions of the g-load correlated deployments. Current Viking maximum deployment dynamic pressure is 1100 Pa; the high Mach number parachute should be able to withstand 1300 Pa. | 97 |

List of tables

| | |
|--|----|
| Table 1. Historical data of sensor accuracy. | 25 |
| Table 2. Historical data of re-entry vehicles with trigger and parachute deployment information. | 28 |
| Table 3. The EXPERT derived ballistic re-entry FMST input data. | 32 |
| Table 4. The inertial matrix of the EXPERT derived hypothetical vehicle. | 32 |
| Table 5. The aerodynamic database of the EXPERT derived hypothetical vehicle. | 32 |
| Table 6. Sensitivity of the points of interest to specific uncertainties; the dispersions are a 3σ percentage of the nominal value. | 44 |
| Table 7. The nominal input and output values and thresholds used for all algorithms. | 46 |
| Table 8. The results of all the algorithm performance test. | 48 |
| Table 9. Off-nominal de-orbiting initial re-entry conditions. | 55 |
| Table 10. Simulation initial conditions and uncertainties of the Monte Carlo simulation. | 59 |
| Table 11. The inertial matrix of the Horus 2b vehicle. | 60 |
| Table 12. The C_D database of the Horus 2-b vehicle. | 60 |
| Table 13. The C_L database of the Horus 2-b vehicle. | 60 |
| Table 14. Quick trade-off table for different methods of measuring the deployment conditions. | 63 |
| Table 15. Worst case Mach estimations for the velocity estimation drift and temperature deviations. | 66 |
| Table 16. Sensitivity results of different measurement errors of the deployment conditions. | 69 |

| | |
|--|----|
| Table 17. <i>Real conditions for deployment at Mach 1.6.</i> | 70 |
| Table 18. <i>Drag measured with and without wind.</i> | 70 |
| Table 19. <i>Measured Mach number with wind.</i> | 70 |
| Table 20. <i>Estimation error of the velocity using a drag derived measurement and a static pressure probe.</i> | 72 |
| Table 21. <i>Mach dispersions of the two different estimation methods.</i> | 73 |
| Table 22. <i>Mach estimation errors of open loop estimation. From Mach 6 on, there is sufficient accuracy for successful deployment.</i> | 75 |
| Table 23. <i>Simulation initial conditions and uncertainties of the MER Monte Carlo simulation.</i> | 85 |
| Table 24. <i>The aerodynamic database of the MER vehicle.</i> | 86 |
| Table 25. <i>Ellipse sizes of the footprint contributions of different types of uncertainties.</i> | 88 |
| Table 26. <i>Real landing and deployment conditions compared with the calculated conditions.</i> | 89 |
| Table 27. <i>Correlations of different g-load thresholds to the downrange and the desired deployment conditions.</i> | 94 |

Introduction

Most re-entry vehicles utilize a DLS for a safe descent through the lowest part of the atmosphere. It usually requires deployment of a parachute in a certain suitable range of flight conditions. The investigation goal is to find a simple, suitable, and precise solution to DLS system activation, while the deployment window may be very limited and the re-entry vehicles may not employ advanced navigation systems.

This DLS trigger system can range from a simple preset timer to much more complex system, employing multiple sensors and capability to respond to off-nominal flight conditions.

Determination of the deployment conditions and constrains may not be straightforward and must be estimated onboard the vehicle by combining various measurements. However adding complexity might lead to a more versatile system, but might reduce reliability.

Due to their mission characteristics the ballistic and lifting re-entry vehicles have been considered separately. The DLS triggering system architectures must be able to deal with off-nominal scenarios. The obtained results allow making a DLS triggering system architecture trade-off based on nature of the a-priori know mission uncertainties.

The performance and reliability is assessed by Monte Carlo simulation campaigns where a set of 3 or 6 degree-of-freedom trajectory simulations have been performed by an in-house high-fidelity flight mechanics simulation tool on real mission derived re-entry vehicles. Part of the work is devoted to studies of possible landing footprint size reduction by utilization of advanced navigation systems and high-mach supersonic drogues. This should be beneficial for recovery operations on earth and landing accuracy on other planets.

Vehicles models, environmental models and trajectories were already available; the investigation solely aims on the parachute triggering itself. Only for a Mars re-entry case an atmosphere model was developed.

In order to have a clear understanding of the contents and the goal of the investigation, a mission need statement is stated:

“Thales seeks to expand the knowledge in parachute triggering algorithms suitable for mission available sensors, sensor requirements and within the mission specific accuracy, reliability with off-nominal adaptively to set a baseline for future missions.”

To support the mission need statement 3 goals are set to show the priority applicable to parachute triggering algorithms:

1. *The probability of a failure of the parachute triggering algorithm should have a failure probability less than 0.27%. Failure is understood as DLS triggering outside the specified window even though DLS system may still operate successfully there. The 0.27% failure rate originates from a 3 standard*

deviations success rate of 99.73%, which is usually used and accepted by the Thales customers.

2. *The algorithm should be able to deal with off-nominal flight paths.* Such conditions are off-nominal de-orbiting or spinning ballistic re-entry of a lifting vehicle.
3. *Reduce the landing area footprint by advanced processing and utilization of sensor information.* This goal should be considered as optional in case time resources allow performing it. However an overview of possible methodologies to achieve this goal is suggested to be included in form of an additional chapter.

The mission need statement and the 3 goals were determined prior to the investigation in order to have defined bounds on the end result of contents of the investigation.

There are 3 investigation chapters in this report. Chapter 2 describes an earth ballistic re-entry case and chapter 3 describes an Earth lifting re-entry case where the primary and the secondary goals will be elaborated, the third goal is investigated separately in chapter 4. But first, chapter 1 will give insight in the background information required for the investigation.

1 Background for parachute triggering for re-entry vehicles

In order to start the investigation a plan and background information are needed. This chapter provides an overview of the problem approach and gives the background information required.

1.1 Investigation plan

The investigation is the development of a measurement setup. The first steps to perform are the steps taken for the development for any other measurement setup:

1. Determine what to measure.
2. Determine how to measure.
3. Design of measurement setups. A measurement setup will not actually be build, but will be modeled. So the third step will be to develop a modeling strategy. For these steps this chapter will provide the necessary background information.

There are three disciplines required for the generation of re-entry parachute triggering algorithms:

- 1) Re-entry characteristics. Different types of re-entry have differences in overall mission complexity and for this reason, require different algorithm development strategies.
- 2) Sensors. The sensors used are important parameters for the achieved accuracy and implementation on the vehicle. The selection of sensors strongly depends on mission environment and characteristics.
- 3) Modeling. The investigation of parachute triggering for re-entry vehicles is performed very broad in its initial phase, but should have an accurate performance estimate at the end of the investigation. This could be performed by extracting parameters from already available software capable of modeling re-entries together with Monte Carlo analysis.

For the Monte Carlo analysis a list of parameters and their uncertainties has to be defined for the following sections of the model:

- Vehicle characteristics. These are models delivered by Thales Alenia Space Italy for the earth re-entry vehicle cases and for the Mars re-entry case they are extracted from literature^{1,6,5,18}.
- Initial conditions. They are based on the upcoming ESA re-entry missions "EXPERT" and "IXV", and found in literature from ARD and MER missions^{3,6,12,5,18}.
- Environment. These uncertainties are already incorporated in the simulation software.

With the use of the Monte Carlo simulations the dispersions of the parachute opening parameters will be extracted. This way the performance to determine the success rate of the triggering mechanism can be determined. Since the investigation is based on hypothetical missions, not a complete system design will be made, but the sensor performance requirements for similar missions will determined.

After a broad selection round, the best performing triggering algorithms will be implemented in a high fidelity model to check nominal and off-nominal performance. This analysis is performed for a ballistic and a lifting re-entry trajectory. Finally opportunities for footprint reduction will be investigated.

1.2 Typical re-entry characteristics

The possibilities for the development of the triggering algorithm differ with the type of re-entry trajectory flown. This difference originates from the amount of control performed during the trajectory. There are three main categories of re-entry trajectories:

1. Ballistic re-entry
2. Lifting re-entry
3. Skipping re-entry

The definition of a ballistic re-entry is a re-entry where no lift is generated. This also implicates there is no active control during the re-entry, because there is no lift vector to manipulate in order to change the vehicle's course. For this reason the insertion conditions, the vehicle's ballistic coefficient and planet with its specific atmosphere completely defines the to-be flown trajectory, in contrary to the lifting re-entry, where the vehicle's GNC system actively manipulates the vehicle's attitude and trajectory throughout the flight. A skipping re-entry is a series of lifting re-entries where the vehicle flies out of the atmosphere one or more times until its final descent. During these skips no parachute is used and the final descent can be considered to be a general lifting re-entry. For this reason the skipping re-entry is not applicable to parachute triggering investigation.

Figure 1 shows four re-entry characteristics of the three re-entry trajectories used in the investigation:

- 1) A ballistic re-entry trajectory on Earth
- 2) A ballistic re-entry trajectory on Mars
- 3) A lifting re-entry trajectory on Earth

The first thing to notice in all plots is the duration of the flight; the lifting re-entry lasts far longer by definition; the average descent rate of the lifting trajectory is much lower due to its lift. In the altitude profiles of Figure 1, it can be seen that the lifting vehicle keeps the same altitude for some amount of time. During this phase, the vehicle is performing roll and bank maneuvers to tilt the lift vector in order not to skip out of the atmosphere but to loose its kinetic energy in the upper layers of the atmosphere. Since the earth-ballistic and the earth-lifting re-entry have to decelerate from about the same velocity to zero, the deceleration and thus the g-loads have to be higher for the ballistic re-entry. This can be seen in the g-loads profile of Figure 1. The insertion velocity for a Mars re-entry will be lower than on earth, this is due to the Mars thin atmosphere and lower gravity. If the velocity of a vehicle is too high, the vehicle will go through the atmosphere and fly out again to leave the planet's orbit. This insertion velocity is a function of the planets gravity field and its atmosphere. Furthermore it can be seen that the Mars ballistic re-entry has about a third of the total g-loads and a 100th of the dynamic pressure with

respect to the Earth ballistic re-entry. This is related to the Martian atmosphere, which is about 100 times rarer than Earth's atmosphere, the low Martian gravity field and the vehicle has a 1.3 times lower entry velocity. Hence the Martian entry vehicles usually have a low ballistic coefficient.

Since the lifting re-entry vehicle loses most of its velocity in the rarer layer of the atmosphere, the dynamic pressure is lower than the ballistic trajectory and because the dynamic pressure is the main factor to generate the g-forces, the $-g$ -forces are lower. Characteristic for a lifting re-entry is the actual dynamic pressure maximum on the very end of the flight, when the vehicle sinks in the thicker layers of the atmosphere.

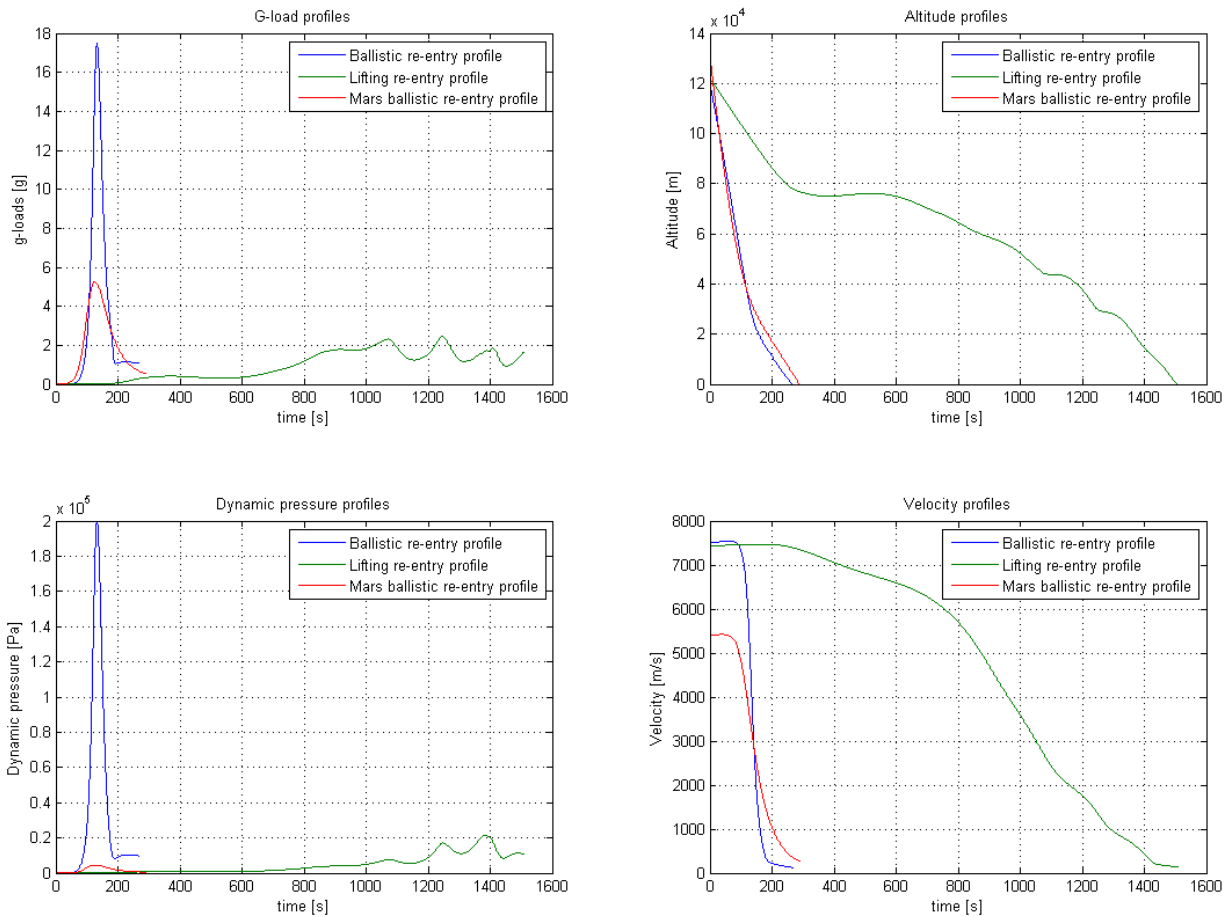


Figure 1. Re-entry profiles of a ballistic and a lifting re-entry on Earth and a ballistic re-entry on Mars.

Despite the velocity is lower and the molar mass of the Martian atmosphere is higher, the maximum Mach number reached on Mars is higher than on Earth, because the specific heat ratio is lower and the atmosphere is far colder. Figure 2 shows the Mach profile for all the re-entry cases investigated. The Mach number will be an important unit in the investigation since it will be assumed the Mach opening window will be the smallest.

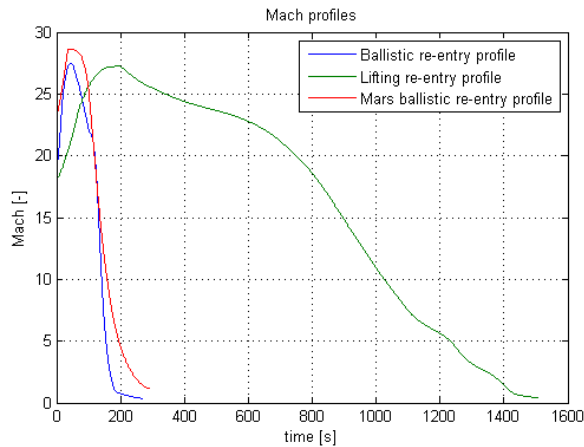


Figure 2. Mach numbers of a ballistic and a lifting re-entry on Earth and a ballistic re-entry on Mars.

1.2.1 The choice between a ballistic or lifting trajectory

A lifting re-entry vehicle with wings has many operational advantages over a non-lifting vehicle. Primarily, the re-entry loads can be minimized to almost any desired level, with flexibility in landing site selection. The vehicle has the ability to deviate its re-entry trajectory to reach selected landing sites "cross range" from the orbital track, and to fine tune de-orbit propulsion system induced errors. Ballistic vehicles can only de-orbit to selected sites which are on the orbital ground track. A lifting re-entry has a lower peak heat flux, but a higher heat load, which requires a different type of TPS (thermal protection system). A disadvantage of the lifting shape over the non-lifting shape lies in the complexity and high cost associated with the guidance, navigation and control (GNC) of the lifting vehicle. A failure of the GNC system could render the vehicle uncontrollable and cause it to diverge a great distance off course. The simple, blunt-body configuration similar to the NASA Biosatellite, the Air Force Discoverer, and the Chinese capsule shapes is the shape most often used. Once re-entry has been initiated, the body essentially falls uncontrolled through the atmosphere with little excursion from the nominal trajectory; however, there is the penalty of higher g-loadings than a lifting shape.

1.3 Parachute triggering opening window

The parachute systems deployment starts when the most severe part of the re-entry has passed. Parachute opening windows of the first stage are generally bounded by the Mach number and the dynamic pressure. The upper boundary of the parachute deployment is generally bounded by the parachute itself, which cannot sustain a certain Mach number or dynamic pressure. The lower deployment bound is usually defined by the lowest Mach number on which the vehicle remains stable or at which the parachute is still able to inflate. Based on these assumptions, the Mach number opening window of the first stage remains in general somewhere between 2 to 0.5. It must also be considered that stability characteristics can change from the supersonic region to subsonic speeds; when the vehicle is not stable at subsonic

speeds, the lower Mach boundary increases from 0.5 to 1.2, where the transonic region starts. Combinations of altitude and airspeed should lead to the required Mach number and dynamic pressure for parachute deployment. An example of parachute opening window requirements can be seen in Figure 13 in paragraph 2.2.

Parachute triggering can also be based on specific trajectory features earlier in the re-entry phase with a timer delay. This way the triggering is specific to the flown trajectory, while having an accurate measurement point. For this reason, the whole ballistic trajectory has to be investigated.

1.3.1 Measured parameters

Drogue parachute manufacturers restrict the usage of their parachutes in certain range of Mach number, dynamic pressure and altitude, in order to guarantee structural integrity, proper inflation, stability and successful functionality of full DLS chain. The altitude is not necessarily a criterion, but might if the total deployment sequence takes more time to complete before impacting the surface. The main measurement to trigger the parachute depends on two parameters:

- The deployment windows of every parameter
- The measurement accuracy of the specific parameter.

The decision priority on which parameter to trigger depends on the characteristics of the parachute. In general it could be stated that the parameter with the smallest opening window has to be the prime estimated value, this not only involves the parachute but also the stability characteristics of the vehicle. In this test case the Mach number estimation will be of most importance and secondary the dynamic pressure. Measurement methods presented will be able to estimate both.

1.3.2 Parachute stages

In general, a parachute sequence consists of supersonic pilot which can be deployed by a mortar, rocket or a slug, followed by a supersonic drogue stage. The drogue is followed by one or more intermediate stages. The final stage has to make sure the vehicle has a gentle touchdown on the ground or in the water. On Mars, up till this moment only one parachute stage was used, which is assisted by retrograde rocket stage or impact cushioned by an airbag at touchdown. Triggering of the first phase depends on pre-defined conditions of the re-entry which have to be estimated. Later stages are generally triggered using a timer, because after the first phase deployment dispersions are very small. The investigation performed focuses on the estimation of the conditions to deploy the first phase. The parachute deployment sequence of ARD is described and displayed in subparagraph 1.3.4.

1.3.3 Parachute types

The re-entry vehicle parachute subsystem is designed to reduce the re-entry vehicle's vertical velocity and provide a relatively soft touchdown. For systems that have parachutes, two types could be used for this application: a ballistic type and a lifting parafoil. The advantages of a ballistic parachute are less complexity and

reduced weight because fewer lines and no actuators are required; no active control and navigation system is required. The lifting parafoil has three advantages over the conventional:

- 1) Being able to reduce the dispersions associated with the de-orbit and re-entry trajectories by using its maneuverability to glide to a pre-determined point
- 2) Having the capability of being manually controlled to minimize landing area impact dispersions.
- 3) By flaring, to reduce the vehicle impact shock at touchdown.

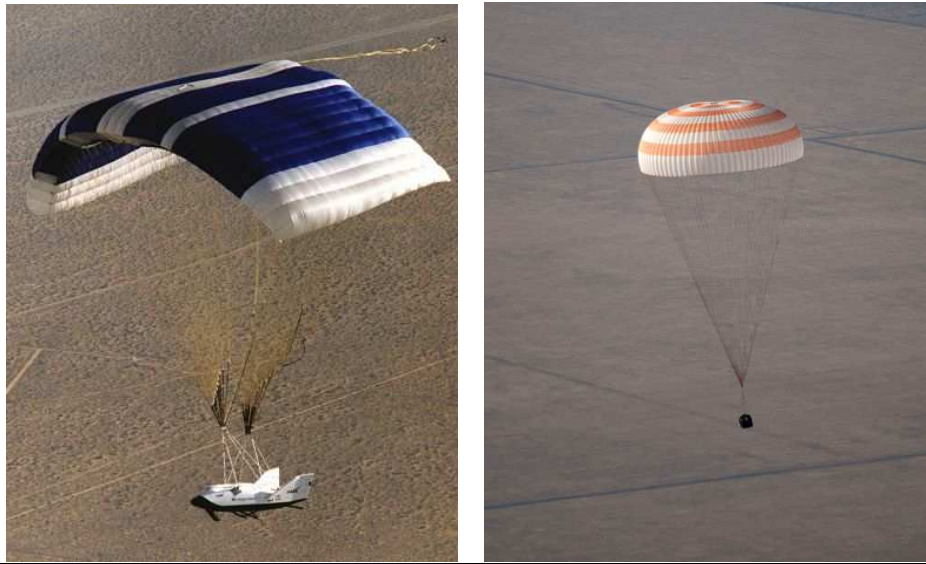


Figure 3. A lifting parafoil carrying the X-38 vehicle is displayed on the left, a ballistic parachute carrying a Soyuz capsule on the right¹⁹.

1.3.4 ARD example parachutes sequence

Up till now, there has been one ESA re-entry mission flown. This mission was the re-entry of the Advanced Re-entry Demonstrator (ARD). To give an indication of a parachute deployment sequence, the ARD parachute deployment sequence is described below.

The ARD recovery sequence started at about 14 km altitude corresponding to an opening Mach number of about 0.6. The sequence dealt with:

- The mortar firing that deployed a pilot chute, Mach number had to range between 0.6 and 0.8 and dynamic pressure between 4500 Pa and 5700 Pa, while altitude between 7.3 and 17.3 km
- 2 s after the pilot chute pulled-off a drogue chute that stabilized the capsule preparing for the main deployment
- The 3 main chutes were then deployed with 2 reefing stages between 1.7 km and 8 km for a Mach number ranging between 0.16 and 0.26 and a dynamic pressure of 1650 Pa. This chutes cluster was sized in order to ensure an impact velocity in the sea of 6.7 m/s in order to mitigate g-load at sea impact,

one bridle was cut just before impact so that the capsule presents a non horizontal attitude with respect to the sea.

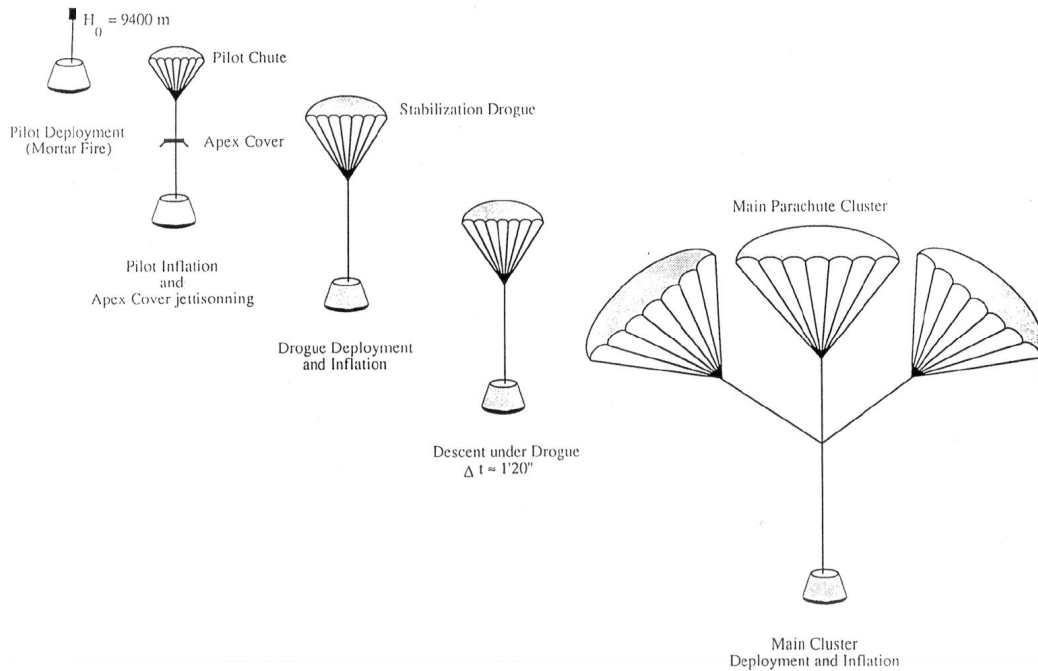


Figure 4. The ARD parachute deployment sequence.

1.3.5 Premature triggering prevention

During the integration, launch and operations of a re-entry vehicle, it might occur that the parachute trigger system measures the conditions to deployment the parachute, for example a g-load measurement triggering the parachute during launch or a pressure sensor measuring above an activation threshold of the pressure at several kilometers altitude, during the system integration at sea level. Such premature activation can very likely cause a total mission failure and for this reason premature triggering protection is necessary. To prevent the parachute triggering system from premature activation at any stage, an activation sequence should be build-in. This sequence should have activation flags at:

1. Pre-launch. In order not to activate the system during integration of the vehicle.
2. Launch. The system should not deploy on the launch loads which it has to endure.
3. Post-de-orbiting. An entry point is defined after the de-orbit engines are cut off. This entry point is the formal point at which the re-entry starts. The sensors and timers can be activated from this point.

These steps should be taken prior to where this investigation for the development of parachute triggering algorithms starts; at the re-entry insertion point.

1.4 Sensors

There are two categories of measurements of the vehicle's state: Intrusive and non-intrusive measurements. Their difference is that intrusive measurements are immersed into the free flow, while non-intrusive measurements have no direct interaction with the environment. Intrusive sensors have limited implementability on re-entry vehicles, since the environment around the vehicle is moving from one extreme, cold vacuum, to another: extreme dynamic pressure combined with high temperatures which only very specific materials can withstand for even only a limited amount of time. In other words, measuring the direct environment is practically impossible throughout the total trajectory.

For a wide investigation of algorithms, it is assumed the vehicle could be equipped with 3-axis accelerometers, g-switches, gyros, air data probes, GPS and pressure gauges. Using the properties of these measurements during the trajectory, the accuracy of these measurements is determined. The lifting vehicle should be able to estimate or measure its attitude, velocity and position vectors.

This paragraph will describe the sensor options which are considered to fly on re-entry missions. The presented options are:

- GPS
- Pressure sensors
- Timer
- Inertial measurement
- Temperature
- Angle of attack measurement

The parachute can be triggered by sensors thresholds, peak values, integral values, or combinations in cooperation with other sensors and timers.

1.4.1 GPS

GPS can be used as supportive measurements for parachute triggering, especially to increase the landing area footprint accuracy. It is not been used because of reliability reasons. During the high heat flux phase of the re-entry, ionization of the air makes it impossible to receive the GPS signal. After this blackout, there is a chance the GPS does not acquire the signal on time. To ensure a high reliability the sensors should be carried onboard. It can be used for altitude measurements with redundant measurement devices. Of course this system works only for an earth re-entry, where the GPS signal is available.

1.4.2 Pressure sensors

Three kinds of pressures can be measured: The static pressure, the dynamic pressure and the total pressure. The static pressure is the pressure of the environment around the vehicle and thus contains no information on the vehicle's state, only the altitude can be estimated with it. It can be measured by static pressure probes, generally placed at multiple positions on the vehicle. It does not have to be in contact to the direct flow: Using compressible flow equations, the real atmospheric pressure can be extracted. Detailed knowledge of the flow around the vehicle is necessary.

The dynamic pressure is the pressure which the vehicle “senses” while it is flying through the atmosphere and pushing against the air on its path. It can be measured with a Pitot-static probe, which has to be positioned in the free flow.

The total pressure is the sum of the static and the dynamic pressure. It can also be measured directly by bringing the airflow to a full stop (with respect to the vehicle) and measure the pressure rise.

Both the Pitot-static probe and the total pressure probe require exposure to the free flow. Because the velocity is in the order of km/s the flow becomes 1500 K and over when it comes in contact with the vehicle, which makes it nearly impossible to produce a probe ably to withstand such conditions. Since parachute deployment is at much lower velocity a deployable probe for the terminal descent phase might be considered. This increases complexity and therefore decreases the reliability.

1.4.3 Timer

The use of a timer is very simple and therefore very fault tolerant. However it is not able to respond to any changes from the programmed nominal flight path and can only be used when the dispersions of the trajectory are small. So it is not very accurate and cannot respond to any off-nominal situations. To increase accuracy a timer can also be triggered on measurements of a different sensor, e.g. a specific g-load or pressure level.

1.4.4 Inertial measurement unit (IMU)

An Inertial Measurement Unit is a device which measures acceleration and angular accelerations along three axes to determine the vehicle’s movement and attitude. For unmanned vehicles, an IMU is generally the main device used for navigation and controlling the vehicle. Inertial measurements can be used for parachute triggering. G-load triggering is used multiple times before.

1.4.5 Temperature

Up till this moment, temperature measurements are not used for parachute triggering. Measuring stagnation pressure might be interesting, but this estimation of stagnation temperatures might not have sufficient accuracy because thermal fluxes are low at supersonic speeds and the vehicle might still have an afterglow from the heat flux encountered before, these remaining heat fluxes are often not very thoroughly investigated for the terminal descent phase whereas such a method would require elaborate a-priori temperature knowledge. However, using compressible flow calculations, both information about the Mach number and the ambient temperature could very well be extracted from direct or indirect temperature measurements.

1.4.6 Angle of attack measurement

The angle of attack can be a criterion for parachute deployment. A high angle of attack can introduce extra loads on the parachute deployment phase, because of the

'wrist effect'. This is the moment there exists at the attachment points of the parachute on the vehicle. The angle of attack can be measured by vanes, pressure differences or can be estimated by the IMU.

1.5 Modeling

The re-entry trajectory and the sensors are to be modeled. The modeling of the re-entry is performed by FMST, 'Flight Mechanics Simulation Tool'. FMST is a Matlab coded package, which has preset vehicle models, gravity and atmospheric models in order to perform trajectory simulations, batch and Monte Carlo analysis of aerospace vehicles. Sensor models are coded into the FMST package. A Martian atmosphere model was generated specifically for the performed investigation. The triggering algorithms have been inserted into FMST. These algorithms range from simple data extraction to make specific correlations afterwards, to Simulink models in order to have a realistic implantation including sensors measurement errors.

1.5.1 Monte Carlo Analysis

The core of the investigation is the Monte Carlo analysis. A Monte Carlo analysis is a repeated computation from which a specified set of input variables have some statistical distribution. The same simulation is performed for a defined number of runs, whereas the dispersed parameters create a slightly different solution on every run. This leads to a corridor of solutions with a corresponding certainty of this corridor. For example, the aerodynamic coefficient is determined in wind tunnel tests and/or CFD calculations; this coefficient can only be determined within some error margin. This error margin can be put in the Monte Carlo analysis to simulate a flying vehicle, encountering slightly more or less drag depending on the variation of the drag coefficient, which will lead to slightly different trajectories.

The strength of the use of Monte Carlo simulations is its ability to incorporate measurement errors and modeling errors, the downside is that it leaves an uncertainty in the end result.

1.5.2 Defining the uncertainties

In order to predict the success rate if the parachute deployment, the uncertainties must be defined. There are three kinds of uncertainty in this model:

1. Measurement errors. In reality sensors are never perfect and have a measurement error. This can be a random error and/or a bias. During the investigation, accuracy will be defined as a function of the sensor error in order to set a requirement for a sensor for a future mission. To get an initial indication on sensor performance, historical data is collected and presented in Table 1.
2. Modeling error. There are estimations and assumptions made on the vehicle and the environment. For example the vehicle characteristics as C_p , C_D are never exact values. Also the atmosphere is modeled, which is of course different from the true conditions.

- Initial conditions. The launcher or de-orbit stage has a specified range of injection conditions, for example the altitude and the flight path angle differ slightly. This has implications for the rest of the trajectory.

| Data from mission | Instrument errors | Full scale | Rel std dev | Bias | Unit | Remark |
|-------------------|-------------------|------------|---------------------------------------|-----------------------|------------------|-----------------------------------|
| ARD | GPS | 500 | - | - | m | For altitude measurement |
| Huygens | Total pressure | 1 | - | - | % | 4-16 millibar Range 0 -1600 hpa |
| ARD | Accelerometer | 0,5 | - | - | m/s ² | |
| Stardust | G-switch | - | 10 | - | % | 3 σ , uniform distribution |
| Stardust | Timer | - | 1 | - | % | 3 σ , uniform distribution |
| Huygens | Accelerometer | - | 54.72*ACC(m/s) ² -0.992 | - | % | 3 σ , CASU instrument |
| Huygens | Accelerometer | 1 | | 1e-4 m/s ² | % | HASI instrument |

Table 1. Historical data of sensor accuracy.

1.5.3 The atmosphere models

One of the atmosphere models used in FSMT is the standard US 76 Extended atmosphere¹¹. For this atmosphere two uncertainty models are applied. One is an unofficial model based on the GRAM atmosphere uncertainty model, the other model is a Russian global uncertainty model: GOCT 24631-8. Atmospheres are generated by a random band of atmosphere temperatures and densities. The bounds of these atmospheric uncertainties are displayed in Figure 5 and Figure 6.

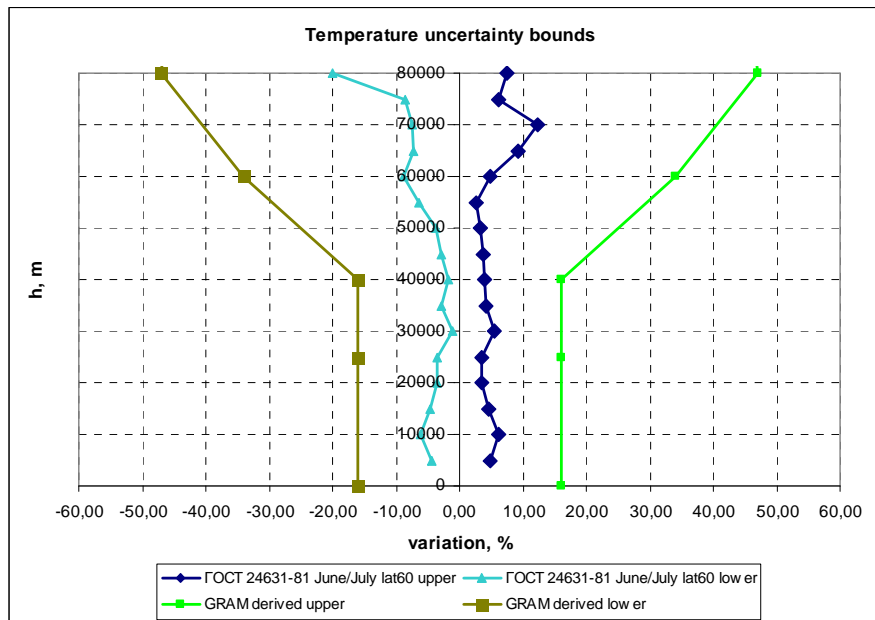


Figure 5. Uncertainty bounds of temperature. Comparison between GRAM derived uncertainties and Russian atmospheric uncertainties GOCT T24631-81.

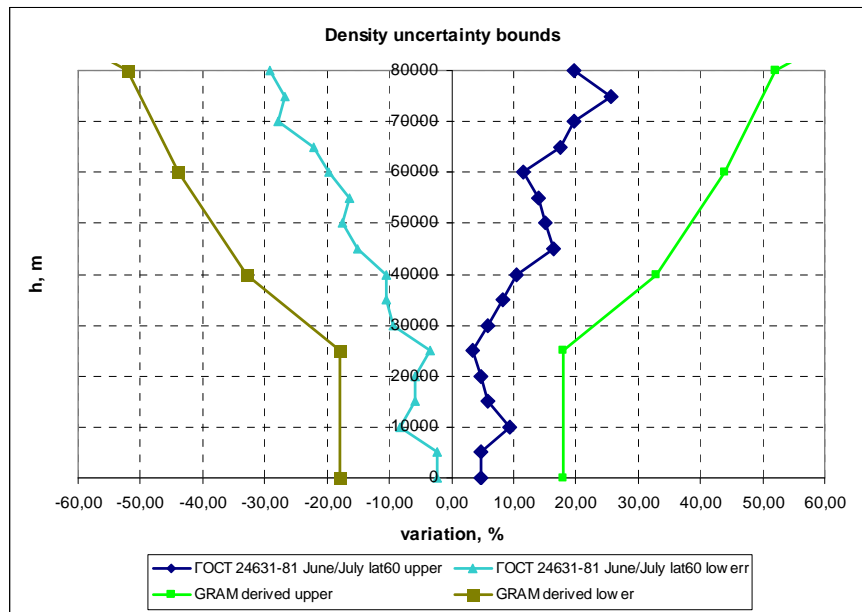


Figure 6. Uncertainty bounds of density. Comparison between GRAM derived uncertainties and Russian atmospheric uncertainties ГOCT T24631-81.

Example results of the atmosphere models are presented in Figure 7 and Figure 8. The blue lines are 100 atmospheres generated using the presented uncertainty models and the red line indicates the standard US 76 model. On the temperature profile, the green and salmon coloured lines provide examples of such randomly generated atmospheres.

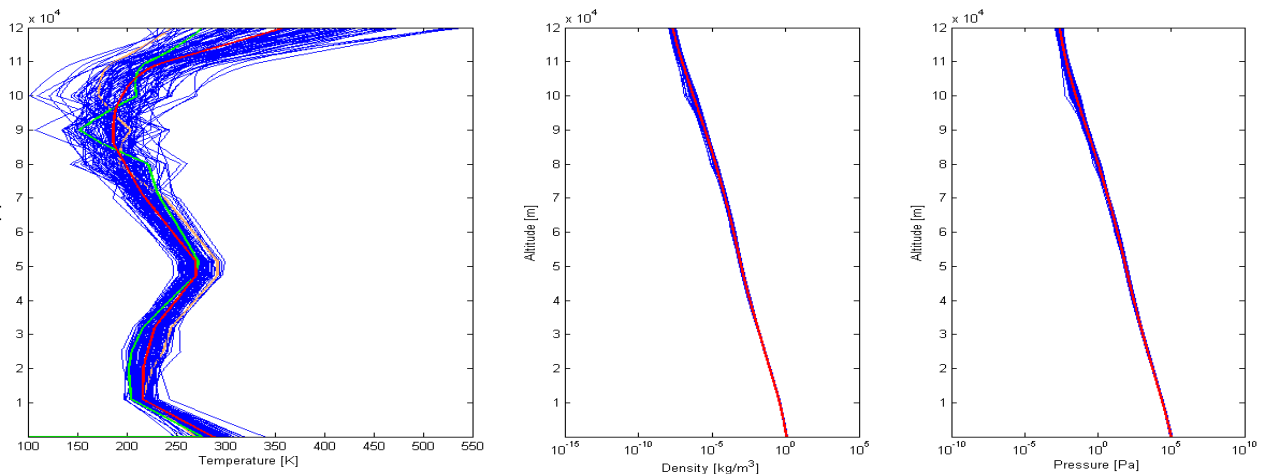


Figure 7. Monte Carlo example of 100 US-76 standard atmospheres and the GRAM derived uncertainty model.

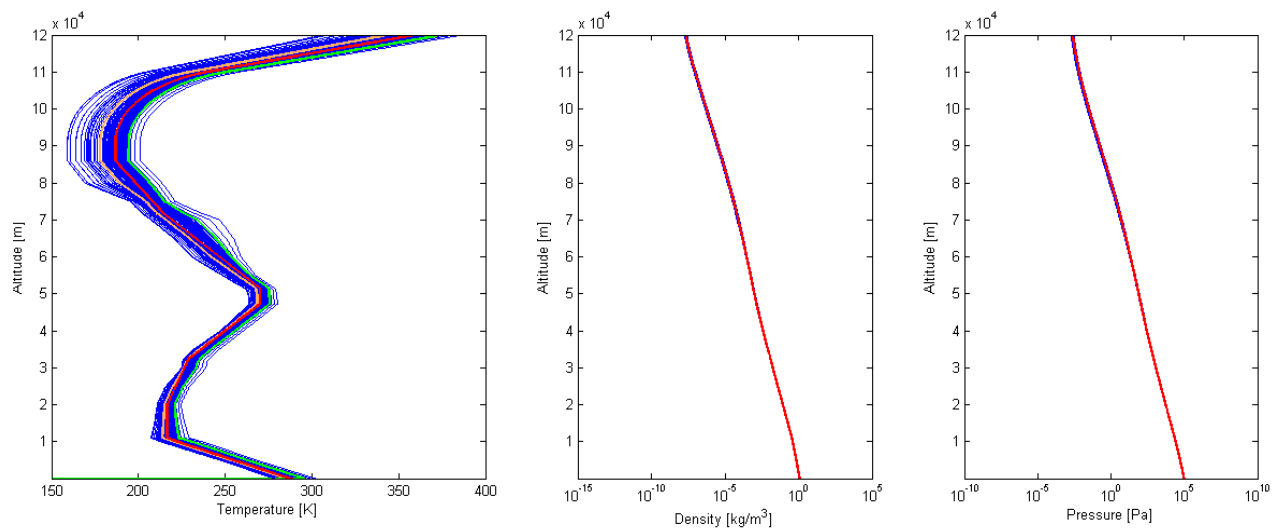


Figure 8. Monte Carlo example of 100 US-76 standard atmospheres and the Russian GOCT T24631-81 uncertainty model.

For the Mars footprint reduction case, an atmosphere model was to be constructed. The model generated is based on references^{1,5,18} and is shown in Figure 9. There is less known of the Martian atmosphere and events like global dust storms can change the atmospheric properties significantly, so the atmospheric uncertainties are high. For this reason the GRAM derived uncertainty model is used. Paragraph 4.3.1 will investigate whether this model is comparable to models used by references^{1,5,18}.

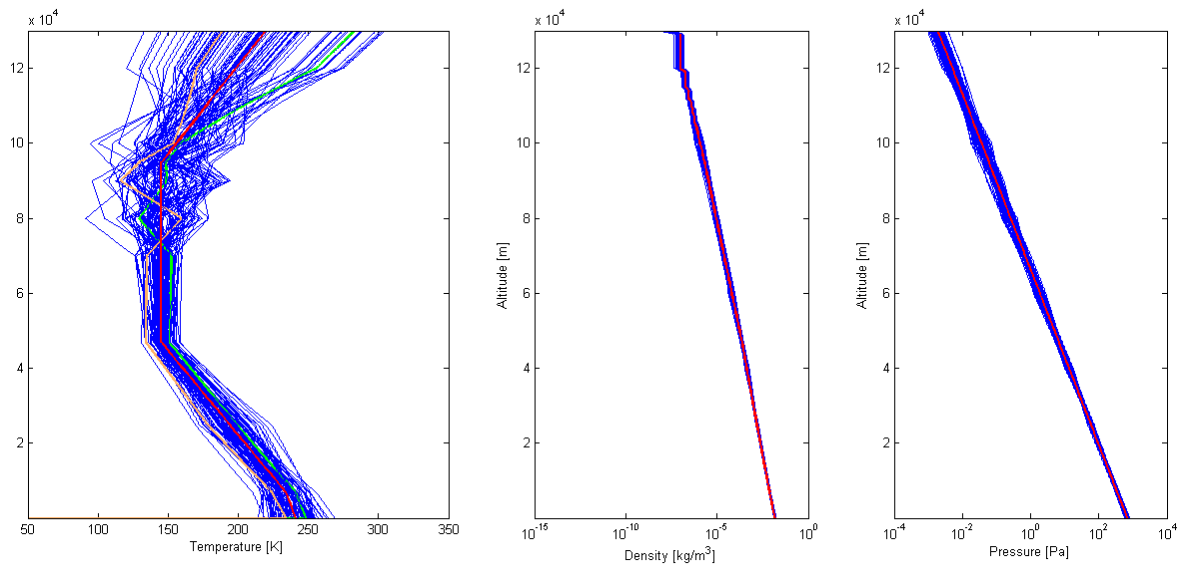


Figure 9. Monte Carlo example of 100 Martian atmospheres and the GRAM derived uncertainty model.

1.5.4 Statistical mathematics used

With the Monte Carlo simulations, two types of statistical distributions are used for input: the uniform distribution and the Gaussian distribution. All outputs are assumed to be Gaussian and the Matlab standard deviation calculation is used. This can be mathematically inaccurate, because there are large deviations from the standard distribution, e.g. deviating kurtosis. However, for comparison between the algorithms this assumption is valid; the smaller the deviation, the more accurate the results are. This can be easily checked by the Monte Carlo analysis, because the amount of failures of a certain Monte Carlo analysis can be counted. This is a very simple method to determine the true performance and avoids mathematical complexity. A result to verify this methodology is presented in Table 8 in paragraph 2.6.

1.6 Table of historical data

In order to learn from previous successful and unsuccessful missions and to check conclusions made, a table is generated with relevant data of previous re-entry missions. The difference between unmanned and manned vehicles is that the manned vehicles have a manual deployment button in case of an emergency, for example, angle of attack oscillation escalation.

| Vehicle | Celestial body | Re-entry type | Primary sensor for 1st stage triggering | Secondary sensors | Deployment Mach | deployment altitude [km] | Deployment dynamic pressure [Pa] |
|----------|----------------|---------------|---|--|-------------------|--------------------------|----------------------------------|
| ARD | Earth | Lifting | IMU and GPS | IMU and DDA | 0,45 - 0.8 | 6 - 12,8, nominal 9.4 | |
| Phoenix | Mars | Ballistic | Dynamic pressure, Timer | Radar | 1,70 | 12,70 | 490 |
| EXPERT | Earth | Ballistic | Timer | | 1.3 - 2.1 | | 1500 - 3500 |
| MSL | Mars | Lifting | | | 2,00 | 6,50 | 750 |
| Beagle 2 | Mars | Ballistic | G-switch trigger on g-peak time | | | | |
| MER | Mars | Ballistic | Timer | | 1,77 | 7,40 | 725-750 |
| Stardust | Earth | Ballistic | G-switch and 2 timers | | 1.2-1.6 | 32,00 | |
| Pre-X | Earth | Lifting | - | | 1,50 | 26,00 | |
| Genesis | Earth | Ballistic | G-switch at 3 g | Redundant sensors, pressure gauge for altitude check and a timer | 1.6 - 2.0 | 33,00 | |
| Apollo | Earth | Skipping | Static pressure | Manual override | | 7,60 | |
| Mercury | Earth | Ballistic | | Manual override | | 6,40 | |
| Viking | Mars | Lifting | | | 1,10 | 5,79 | 350 |
| MPF | Mars | Ballistic | | | 1,57 | 9,40 | 585 |
| Pares | Earth | Ballistic | Altitude measurement | | 1,50 | 21 to 22 | 7300 |
| Huygens | Titan | Ballistic | Timer | G-switch | 1,50 | 159,00 | |
| Soyuz | Earth | Ballistic | Static pressure | | | | |
| Raduga | Earth | Ballistic | Static pressure | | 1 - 2 nominal 1.5 | 13 - 17, nominal 15.5 | 2000 - 3000 |

Table 2. Historical data of re-entry vehicles with trigger and parachute deployment information.

2 Algorithm analysis for a ballistic re-entry

This chapter describes the development and performance test of parachute triggering algorithms for a ballistic re-entry by means of a test case and Monte Carlo simulations. The investigation is based on the characteristics of the vehicle and its trajectory. Because this investigation is in its exploration phase, sensor characteristics will not yet be taken into account. From the result of this methodology exploration study, high fidelity models are made which can conclude about sensor requirements.

2.1 Algorithm development procedure

The development of the algorithms is based on the investigation of specific points of interest along the re-entry trajectory. First the flight dispersions are investigated to identify points of interest. Then these points are assigned as points to activate either a direct triggering mechanism or to store to make a correlation with some other points of interest. These correlations can be used to make an adaptive algorithm. Figure 10 displays the steps taken for the ballistic re-entry algorithm development.

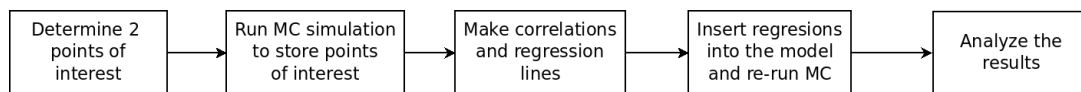


Figure 10. Algorithm development flow diagram

2.1.1 Correlated algorithm flow diagram

These correlations are coded to algorithms from which the flow diagram is displayed in Figure 11. These simple linear logics can be used with a microcontroller or with an analogue circuit board, from which capacitors and resistors are sufficient to build a timer and linear regression. Such simplicity is desired in order to provide a high reliability of the system. All these algorithms contain a time interval measurement and a correlation, which calculates the time from the measured time interval to the deployment time, which depends on the dispersions. After the interval measurement is completed, at least 10 seconds are available for calculation and possible signal noise suppression. A further advantage of introduction of a time delay before the deployment is the elimination of measurement errors induced by the angle of attack oscillations, which remain small above Mach 2, for this reason it is beneficial to measure not at the last second, but at the point where the vehicle is the most stable, and the correlation is the highest.

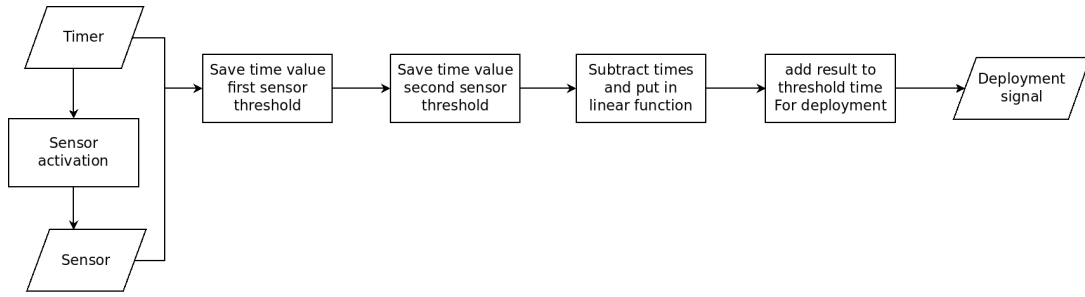


Figure 11. Correlated algorithm functional flow diagram

2.2 Test case scenario

In this paragraph all the inputs for a Monte Carlo simulation for a ballistic re-entry are defined. The case analyzed is a capsule with a ballistic trajectory. It is an EXPERT vehicle derived capsule and is showed in Figure 12. This hypothetical mission is based on the original 3rd EXPERT mission, which would have been an EXPERT like capsule re-enter from full orbital velocity. The initial conditions will be determined together with their uncertainties. The uncertainties of the initial conditions are specified by the launcher or the de-orbit stage injection accuracy. The driving uncertainties are the flight path angle, the aerodynamic uncertainties, the mass and its distribution and the atmospheric variation.

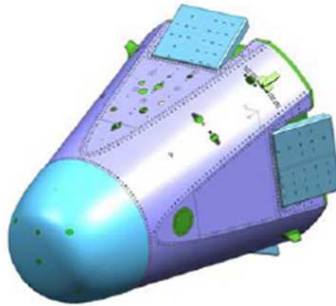


Figure 12. The EXPERT re-entry vehicle²⁰.

All conditions and uncertainties are listed in Table 3. The data is based on the EXPERT mission and the ARD mission.

| Nominal conditions ballistic re-entry | Lower limit | Upper limit | Distr. | Unit | Remark |
|---------------------------------------|---|-------------|--------|------------|---|
| Vehicle | Model similar but not equal to the EXPERT capsule | | | | |
| Mass | 490 | -14.7 | 14.7 | 3 σ | kg |
| Inertia matrix | See Table 4 | -10 | 10 | 3 σ | % Unit applies to the uncertainties, inertia unit is kg/m ³ |
| Aerodynamic | See Table 5 for drag coefficients | | | | |
| $\Delta CA < Mach 2$ | - | -5 | 20 | Uniform | % This parameter defines only the dispersion, the aerodynamic value itself is calculated during the simulation |
| $\Delta CN < Mach 2$ | - | -10 | 10 | Uniform | % This parameter defines only the dispersion, |

| Nominal conditions ballistic re-entry | Lower limit | Upper limit | Distr. | Unit | Remark | |
|---------------------------------------|---|-------------|--------|------------|--|--|
| | | | | | the aerodynamic value itself is calculated during the simulation | |
| $\Delta C_m < \text{Mach } 2$ | - | -10 | 10 | Uniform | % | This parameter defines only the dispersion, the aerodynamic value itself is calculated during the simulation |
| $\Delta C_A \geq \text{Mach } 2$ | 0 | -5 | 5 | 3σ | % | This parameter defines only the dispersion, the aerodynamic value itself is calculated during the simulation |
| $\Delta C_N \geq \text{Mach } 2$ | 0 | -5 | 5 | 3σ | % | This parameter defines only the dispersion, the aerodynamic value itself is calculated during the simulation |
| $\Delta C_m \geq \text{Mach } 2$ | 0 | -10 | 10 | 3σ | % | This parameter defines only the dispersion, the aerodynamic value itself is calculated during the simulation |
| Scenario | GEO position NED (North Eastern Down) speed, VEL attitude | | | | | |
| Altitude | 120000 | 500 | 500 | 3σ | m | Dispersions from report of James T.A. Chartres, Hopper spec |
| Latitude | 59.3 | 0 | | | deg | Is only applicable for footprint |
| Longitude | 22.5 | 0 | | | deg | Is only applicable for footprint |
| Velocity | 7500 | -10 | 10 | 3σ | m/s | Dispersions from report of James T.A. Chartres, Hopper spec |
| Heading | 356 | 0 | | | deg | Is only applicable for footprint |
| Flight path angle | -5 | -0.2 | 0.2 | 3σ | deg | Error from the ARD programme |
| Mission time | 250 | | | | s | |
| Attitude | | | | | | |
| alpha | 0 | | | | deg | Value not used in ballistic point mass re-entry simulation |
| beta | 0 | | | | deg | Value not used in ballistic point mass re-entry simulation |
| phi_aero | 0 | | | | deg | Value not used in ballistic point mass re-entry simulation |
| roll_dot | 0 | | | | deg | Value not used in ballistic point mass re-entry simulation |
| pitch_dot | 0 | | | | deg | Value not used in ballistic point mass re-entry simulation |
| yaw_dot | 0 | | | | deg | Value not used in ballistic point mass re-entry simulation |
| alpha bias | 0 | -2 | 2 | 3σ | deg | Due to aeroshape's asymmetric imperfections and lateral deviation of CoG from centerline |
| alpha bias direction | 0 | -180 | 180 | Uniform | deg | Due to aeroshape's asymmetric imperfections and lateral deviation of CoG from centerline |
| Environment | | | | | | |
| Atmosphere | US 76 | | | | | ГОСТ Т24631-81 uncertainty model |
| Parachute opening conditions | Parachute opening variables depend on each other, see Figure 13 | | | | | |
| Altitude | 16000 | -1000 | 1000 | NA | m | |
| Mach number | 1.7 | -0.2 | 0.2 | NA | - | |
| Dynamic pressure | 20600 | | | | n/m ² | Is described as a function of Altitude, see Figure 13 |
| Simulation properties | A basic earth model is used with J2 gravitational model | | | | | |

| Nominal conditions ballistic re-entry | | Lower limit | Upper limit | Distr. | Unit | Remark |
|---------------------------------------|-----------|-------------|-------------|--------|------|--------------------|
| Solver | ODE 4 | | | | - | Runge-Kutta method |
| Time start | 0 | | | | s | |
| Time step | 0.1 | | | | s | Fixed time step |
| Scope decimation | 1 | | | | s | |
| Julian date | 2455742.5 | | | | - | 30 june 00:00 UTC |

Table 3. The EXPERT derived ballistic re-entry FMST input data.

Parameters not listed in the table are the inertia matrix and the aerodynamic database. They are provided in the following table:

| Intertia matrix | | kg*m ³ |
|-----------------|-----|-------------------|
| 60 | 0.2 | 0.5 |
| 0.2 | 120 | 0.5 |
| 0.5 | 0.5 | 120 |

Table 4. The inertial matrix of the EXPERT derived hypothetical vehicle.

The aerodynamic characteristics are depended on the Mach number. The following table lists the C_D values used:

| | | | | | | | | | | | |
|-------|-------|------|------|------|-------|------|------|------|------|------|------|
| M | 0.1 | 0.3 | 0.6 | 0.7 | 0.8 | 0.85 | 0.95 | 1.05 | 1.1 | 1.2 | 1.32 |
| C_D | 0.435 | 0.44 | 0.45 | 0.46 | 0.5 | 0.52 | 0.65 | 0.86 | 0.85 | 0.81 | 0.74 |
| M | 1.45 | 2 | 3 | 5 | 6 | 10 | 14 | 16 | 20 | 30 | |
| C_D | 0.71 | 0.58 | 0.44 | 0.38 | 0.365 | 0.35 | 0.35 | 0.35 | 0.35 | 0.35 | |

Table 5. The aerodynamic database of the EXPERT derived hypothetical vehicle.

Finally the parachute opening window is depicted. The opening window is a function of the Mach number, the altitude and the dynamic pressure.

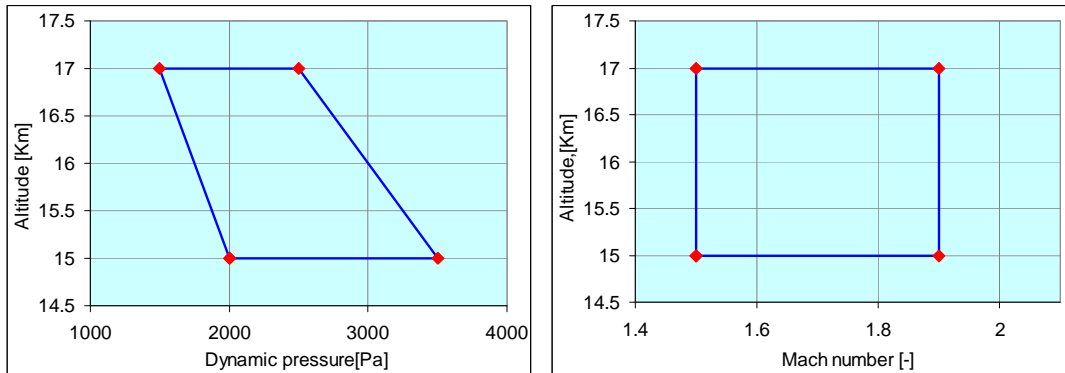


Figure 13. The parachute opening constraints.

All this data provided is inserted into FMST as a 3 DOF model. By definition of a ballistic re-entry, the AoA will always be zero in the simulation. The AoA bias will be treated as a disturbance. The results are presented in the next paragraph.

2.2.1 The nominal ballistic trajectory

Figure 14 presents a combined plot of the main characteristics of the nominal trajectory of the ballistic re-entry. The capsule is unmanned, so g-forces are allowed to go far beyond 10. The g-load peak and the dynamic pressure peak are occurring at the same time because the g-loads are induced by the dynamic pressure. The initial velocity of 7500 m/s is a typical velocity for an Earth re-entry insertion point. The shape of these curves is completely defined by the vehicle's specifications, the entry conditions and the Earth environment; the vehicle 'falls' uncontrolled back to the surface.

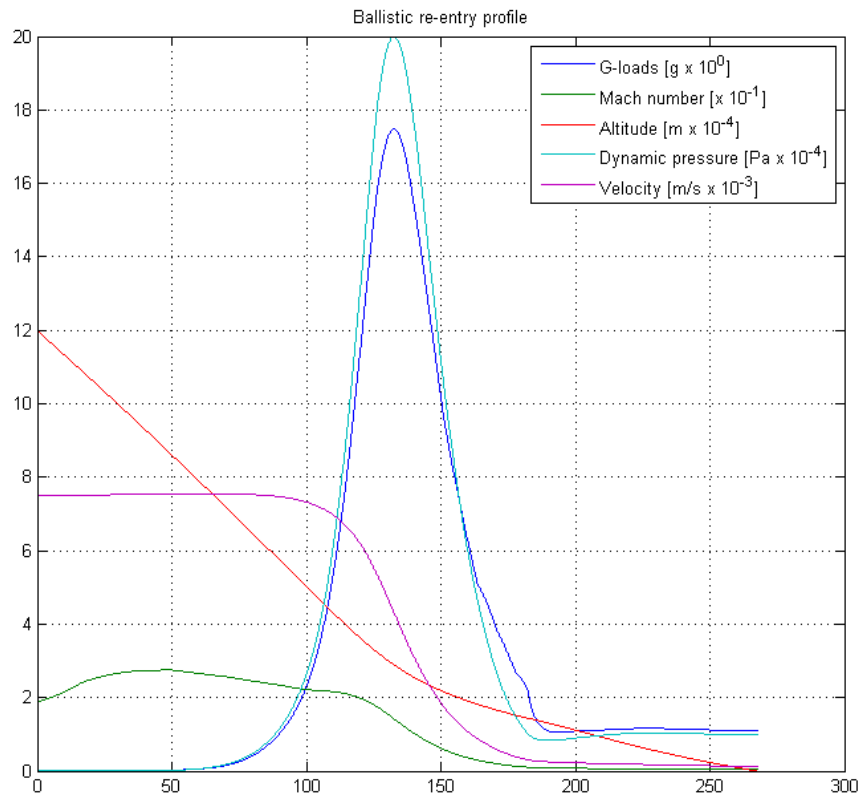


Figure 14. The Earth ballistic re-entry profiles. All y-axis values are multiplied by the value provided in the legend.

2.3 Flight path dispersions

In order to design a triggering mechanism, the flight path and its uncertainty corridor must be analyzed. This paragraph presents the characteristics of the defined re-entry conditions.

The flight path characteristics are investigated on relations between Mach number, g-loads, dynamic, total and static pressure. These parameters are investigated because their properties belong to either the parachute restrictions (Mach number and pressure) or are candidates for onboard measurements (g-load and pressures). Since the parachute specification has the narrowest range in Mach number, the triggering design will be aimed to stay within these bounds. The altitude and dynamic pressure are related to the maximum forces the parachute is able to handle.

Figure 15 shows the relations of g-load, time and total pressure with the Mach number. It can be seen that before interaction with the atmosphere the dispersions are small, because the dispersions are only induced by the initial conditions. At the point where there is the most interaction, the g-load and pressure peaks, the dispersions are the largest.

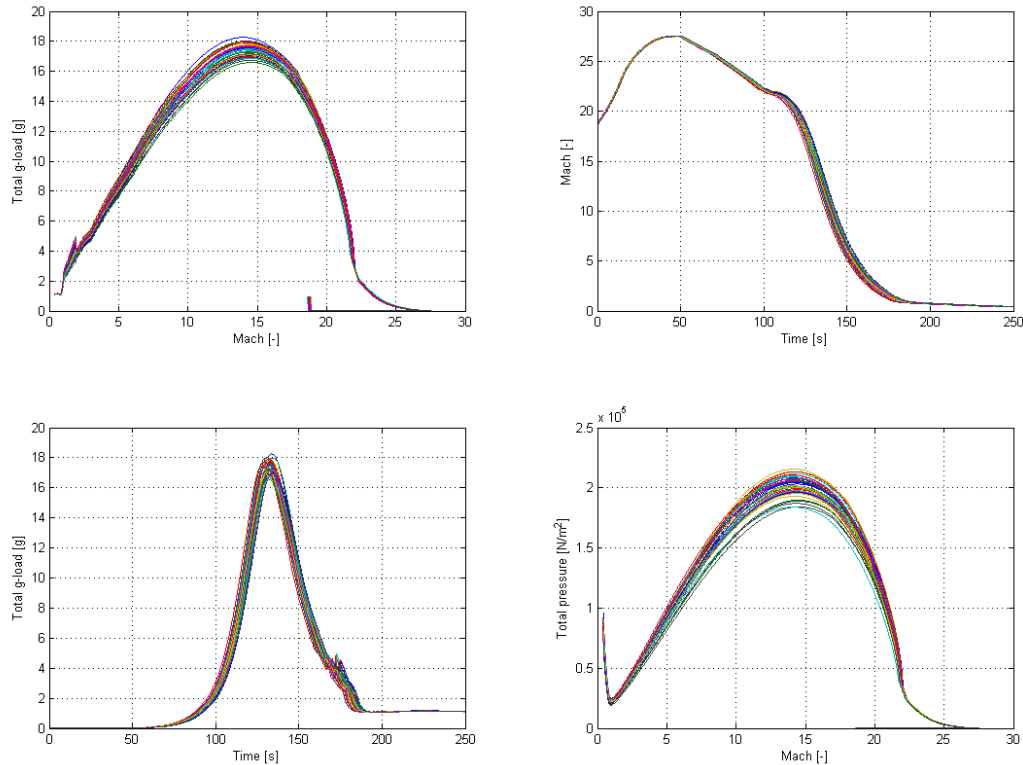


Figure 15. *Trajectory dispersions by Monte Carlo simulation*

Points with either very small or very large dispersions are interesting to investigate. Points with small dispersions are 'stable' points where the conditions are relatively well known. So measuring such a point provides accurate information at the current state of the trajectory. The largely dispersed regions might also be very interesting, if one of the largely dispersed parameters has a correlation which can be measured easily, an accurate and adaptive algorithm can be created.

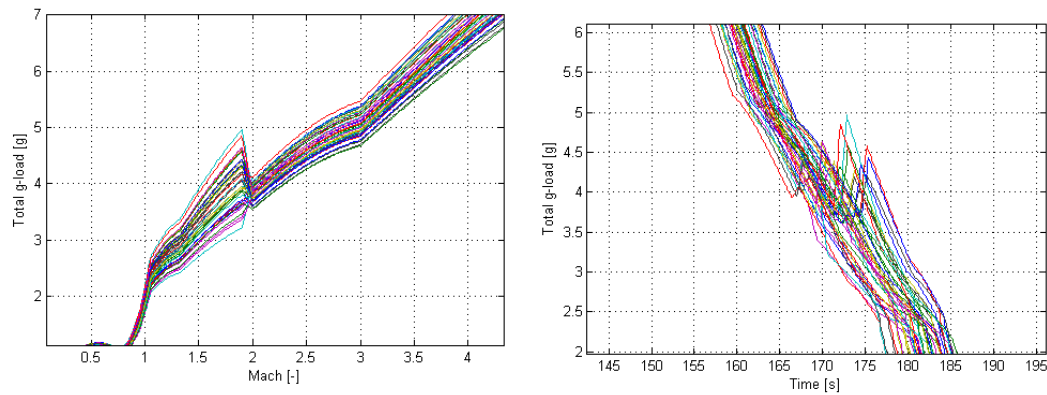


Figure 16. *Dispersion discrepancy, created by the transition of a Gaussian to a uniform uncertainty distribution.*

Figure 15 shows a discrepancy at the g-loads at the end of the trajectory, this discrepancy is magnified in Figure 16. At the point where Mach 2.0 is reached a sudden step can be seen. This step does not happen in reality and is a modeling discrepancy. From Mach 2.0 the uncertainties are higher because between Mach 2 and subsonic flow, the properties change significantly. So what is seen in the picture is not the actual flight corridor, but the region of uncertainty. For the design of a triggering algorithm, this increased uncertainty comes at an unfortunate point, since the nominal deployment is at Mach 1.7; this discrepancy comes at only 3 seconds before the nominal deployment and this uncertainty is uniformly distributed, therefore it will be hard to adapt to it. The total pressure depicted in Figure 15 in the right lower corner and the static and dynamic pressures shown in Figure 17 do not have this discrepancy, because they are independent of the vehicle's shape.

Figure 17 shows that total pressure curves are very similar to the dynamic pressure curve. They only differ at the last part, where the static pressure becomes significant. The static pressure is already significant during the deployment phase so for some points of investigation, total and dynamic pressures are investigated separately.

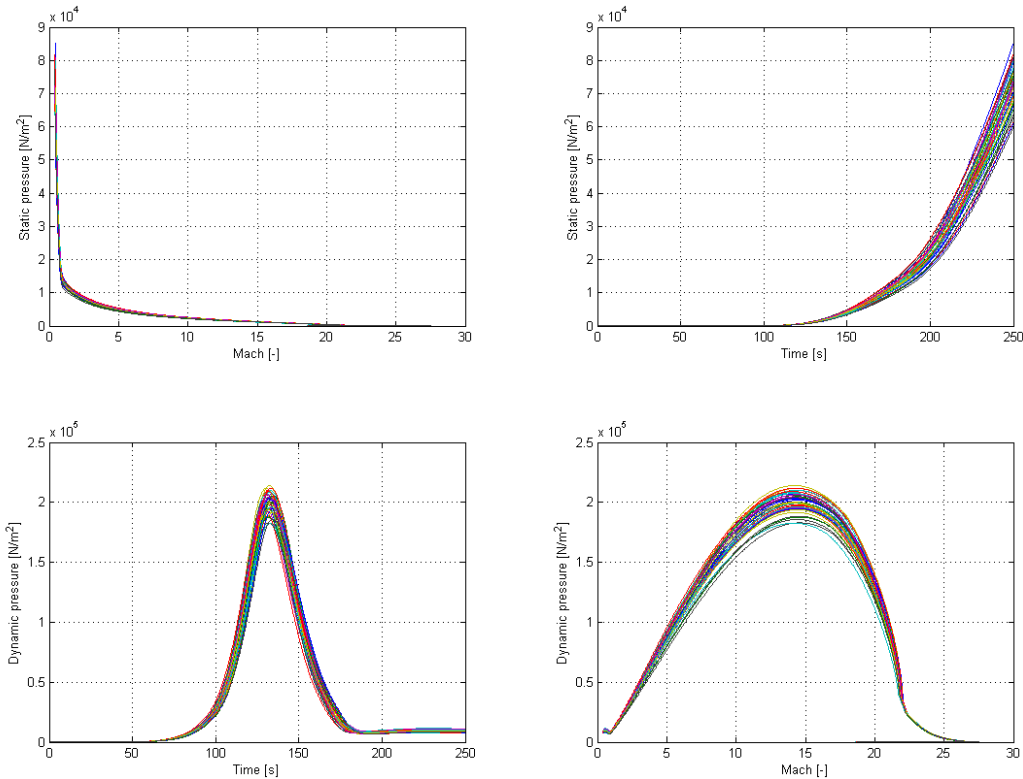


Figure 17. Pressure dispersions by Monte Carlo simulation.

2.4 Selection of characteristic points for triggering algorithms

This paragraph presents 22 cases for parachute triggering algorithms. These cases are developed to be based on different sensor types, the simulation uncertainties and on their correlation to trajectory characteristics. The algorithms will be judged on their performance and implementability.

2.4.1 Time measurement

Throughout the mission a timer is running to measure and to trigger events. Using this timer is the simplest method to trigger the parachute. For this reason it is used in small sounding rockets. However, this method is not adaptable to any input from the environment and can only be used when the trajectory is known accurately.

Case 1: Mission timer

It will be investigated if the current dispersions are small enough to use a timer. If this is the case, this trigger is preferable, because of its simplicity. The timer is simulated at T_0 at the simulation. During the real mission the exact time of the initial conditions is known within certain accuracy. This is taken into account in the simulation.

2.4.2 G-load measurements

The measurement of g-forces is a simple measurement which does not require any interaction with the vehicle's environment. Especially for the extreme aero thermal environment around the re-entry vehicle, this is a very important feature. For a ballistic re-entry, the g-load curve has got a very characteristic shape. Measurement points can be put on characteristic points in order to extract information of the as-flown re-entry, taking into account initial conditions, aerodynamic, mass (distribution) and atmospheric uncertainties. Figure 18 shows the nominal g-load curve with 9 points to be investigated. Re-entry characteristics are tried to be correlated with:

- Width of the g-load peak: Points 4,8 and 5,7 measure this characteristic
- The value of the maximum g-load and its time of occurrence: Point 6.
- The duration of the re-entry: Point 1 and 8.
- The slope of the curve: Point 7 and 8.

The values of these particular thresholds can be optimized in a later phase of the development for a particular vehicle with its particular uncertainties.

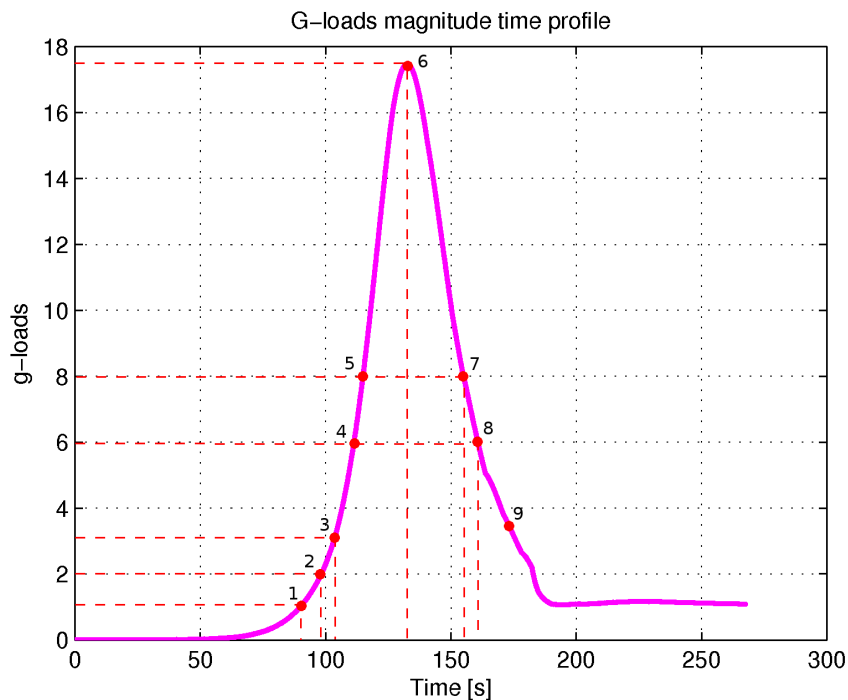


Figure 18. The g-load curve of the nominal ballistic re-entry trajectory with points of investigation.

The first g-load measurement opportunities investigated are thresholds for 1, 2 and 3 G at ascending side of the g-load curve (corresponding to points 1-3 in Figure 18). These low g thresholds are identified as the first opportunity to detect the re-entry phase using accelerometers. As mentioned in paragraph 2.3, the dispersions at these points are relatively small, so they provide good information on the state of the re-entry at that point in time. 3 points are taken to investigate whether the value of the threshold makes a difference. The 1 g value is identified as the first opportunity to measure; the 3 g value might provide better measurement quality because of a

lower relative measurement error. Also the slope of the g-curve is steeper which results to a lower error in measurement time for measuring a threshold.

The value of the g-peak (point 6 Figure 18) is a characteristic for the depth of penetration in the atmosphere. A higher g-peak can mean a higher ballistic coefficient or a steeper flight path angle. The time at which this g-peak occurs is also investigated, because the g-force measurement is qualitative. It is assumed a measurement of time of occurrence is easier and more accurate than the value itself.

Case 2: Direct g-trigger at nominal g-load

Point 9 represents the g-load at parachute deployment. The triggering directly on a specific g-load will also be investigated, because it is identified to be the simplest g-load triggering method and it has been used often on previous missions.

Case 3, 4 and 5: G-load trigger and a timer delay

Besides triggering directly at the nominal g-load, a g-load measurement at a point with less uncertainty than the direct-g trigger point in time can be used to 'calibrate' the mission timer. This is a combination of cases 1 and 2. This performance is investigated for a point in a late phase of the re-entry, case 3 (point 8). It is investigated at early point of the re-entry (point 1), case 4. Finally it is matched to the time the g-peak occurs (point 6); because very simple devices should be able to measure this event and a qualitative measurement like the position of a maximum is very simple.

Case 6: G-peak time and magnitude

Because both the magnitude and the time of occurrence of the maximum g-load are providing information of the trajectory, it might be a very adaptive algorithm, but the performance is hard to predict. This is the reason this specific point (6) is analyzed.

Case 7 and 8: G-switches

Table 2 shows G-switches are often used for ballistic parachute triggering. These G-switches are small cylinders with a spring inside and an electrical conductive mass which make contact at one specific g threshold. Because these switches have been used before, they are also included into the investigation. The time measured for how long the vehicle is above a certain threshold is characteristic for the width of the g-peak, which is a characteristic of the re-entry trajectory. For example a steeper flight path angle will lead to a higher g-load peak, while the peak itself has a smaller width.

In the investigation 6 and 8 g switches are investigated, corresponding to measurement points 4, 5, 7 and 8 for Figure 18. 6 g is 13.1 second before the nominal triggering time. Due to the dispersions this time can be less (± 4.3 sec) and the parachute sequence has to be initiated, so a 13 second margin is defined to be a suitable margin for initial analysis. A higher value is used to investigate whether the height of the threshold is of importance.

Case 9, 10 and 11: G-peak time

The time the g-peak occurs is a qualitative measurement, which is a very reliable measurement. Furthermore it is expected this time has correlation with the dispersions. E.g. the peak-g occurs later when it the flight path angle is smaller than nominal (See Figure 19). Three different cases are studied to investigate the activation of the algorithm: 1 g, 2 g and 3 g (points 1, 2 and 3).

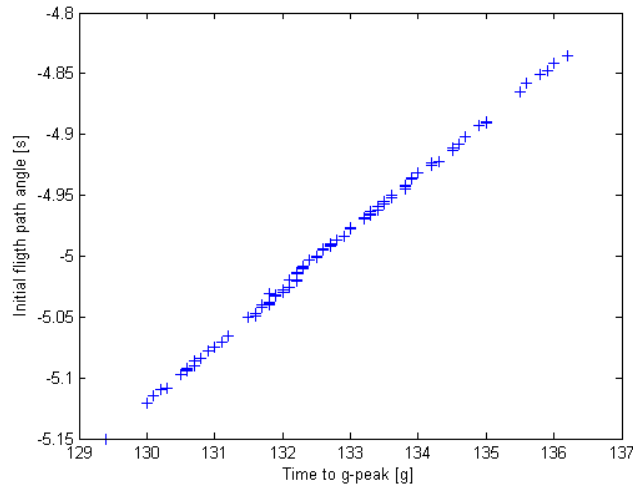


Figure 19. Correlation example of the time of occurrence of the g-load peak with the initial flight path angle.

Case 12, 13 and 14: G-peak magnitude correlation

Similar to the g-peak time, the g-peak magnitude can be used for correlations. Also the 1, 2 and 3 g thresholds are used.

Case 15: Re-entry duration

In order to try to involve all dispersions as much as possible, the first measurable threshold and the threshold the closest to deployment are used. From measurement error point of view this is also interesting, because the relative error becomes smaller when the total measurement duration becomes longer.

Case 16: Deceleration just before triggering

Instead of trying to correlate the complete trajectory to specific measurements, it can also be tried to make a last moment correction on the nominal phase. This is done by measuring the time it takes for the deceleration to go from 8 to 6 G (Figure 18 points 7 and 8). With the 6 G boundary being defined as latest boundary for the reason explained in case 8.

2.4.3 Pressure

Besides measuring the G-force also pressure measurements can and have been used. There are three kinds of pressure measurements:

1. Static pressure
2. Total pressure
3. Dynamic pressure

The dynamic and total pressure curves have very similar characteristics as the g-curve, because the deceleration is caused by the dynamic pressure. However, in the measurements methodology there are differences:

First off all, direct measurement of total pressure at high velocities is almost impossible, because a pressure probe would not survive the heat flux. However, indirect measurements can be performed, like drag derived measurements, which use the axial deceleration component to estimate the dynamic pressure. Furthermore, measurement characteristics differ from g-load; a different flight path might have same g-load, but have very different pressure readings: A higher velocity at a high altitude than nominal leads to similar g-loads, but different pressure readings, because of the difference in trajectory. Finally, the pressure readings are more complicated because they consist of 2 varying parts: Static and dynamic pressure. Therefore it is not expected g-load and pressure readings to have exchangeable correlations, although on first sight they look similar, which can be seen in Figure 14.

2.4.4 Static pressure

This measurement has been used for parachute triggering for both Apollo and Soyuz. It is the only pressure measurement which can be performed directly and without a deployable pressure probe because it does not have to be subjected to the direct flow, unlike a total pressure or Pitot-static probe. The measurement is still not a simple measurement, since the flow field around such a sensor should be understood in order not to measure any remaining dynamic pressure around the vehicle. Figure 20 shows the static pressure the vehicle encounters during its nominal trajectory.

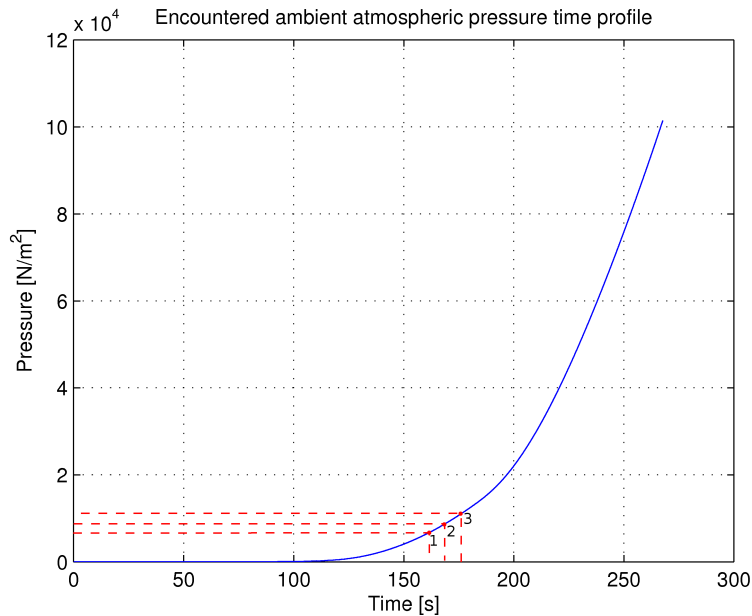


Figure 20. The static pressure curve of the nominal ballistic re-entry trajectory with points of investigation

Case 17: Direct deployment at nominal static pressure value

Again, first the simplest method is applied: Trigger directly on a preprogrammed nominal static pressure value (point 3). This method is expected to have a good performance on altitude deployment. However, this does not guarantee accurate Mach number and dynamic pressure values.

Case 18: Static pressure rate

To make an adaptive algorithm using static pressure measurements, the rate of increase of static pressure is investigated. Two pre-set single-value preset pressure probes are simple hardware and can still provide more accurate result than a single measurement point. For this algorithm, point 1 and 2 of Figure 20 are correlated to the time of deployment, around 13 seconds later, for similar reasons as the last g-point measurement.

2.4.5 Dynamic and total pressure

Measurement of total pressure and dynamic pressure are taken together, because they are almost similar. Even in the way they are measured: The total pressure is measured and for the dynamic pressure the static pressure is subtracted. Furthermore differences only apply in the later phase of the re-entry, since in the low density upper atmosphere layer, the static pressure is negligible. In order to investigate whether there is any difference in the measurements both types of pressures are investigated; the measurement of the total pressure yields information about the velocity (dynamic pressure) and the altitude (static pressure), it is investigated whether this measurement might have better correlation to the deployment conditions. Figure 21 and Figure 22 depict the dynamic and total pressure curves throughout the re-entry.

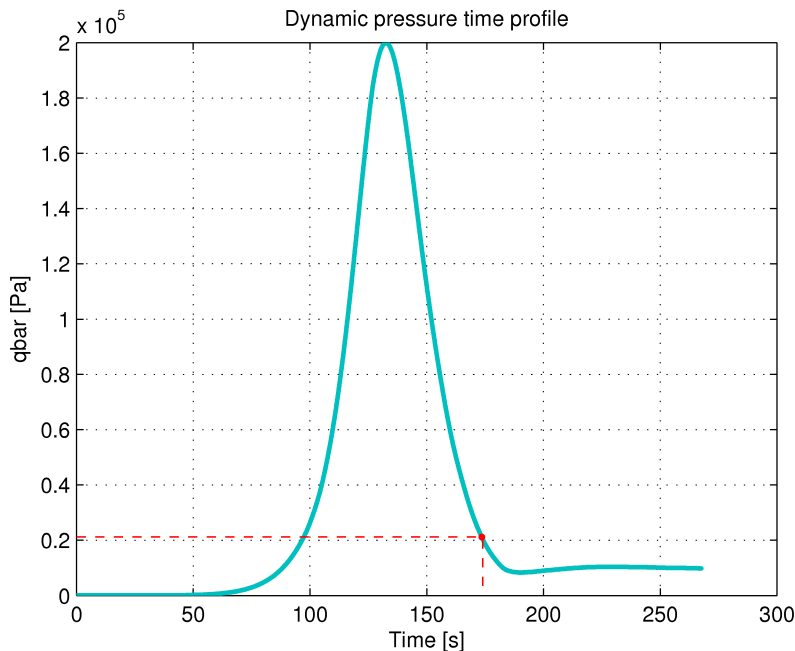


Figure 21. *The dynamic pressure curve of the nominal ballistic re-entry trajectory with its point of investigation.*

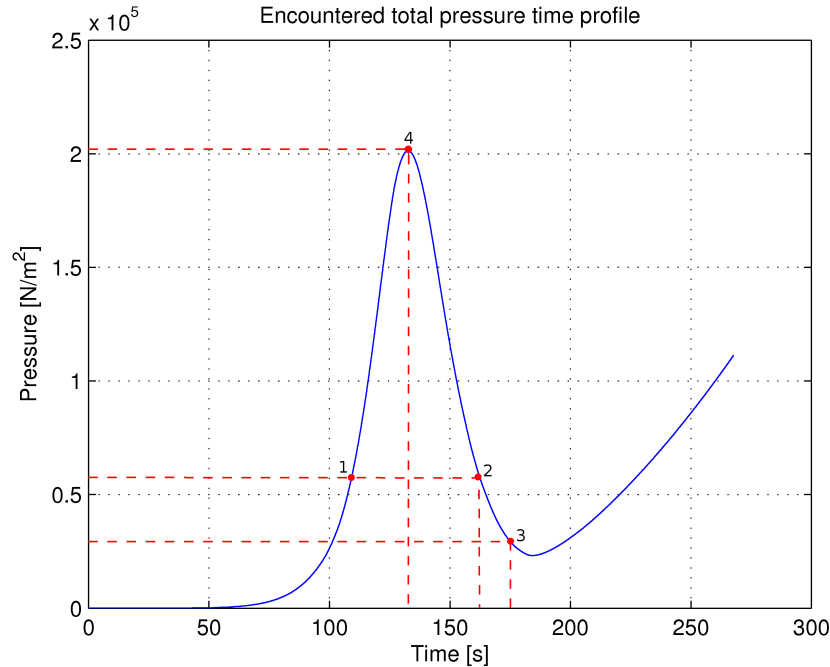


Figure 22. The total pressure curve of the nominal ballistic re-entry trajectory with points of investigation.

Case 19: Direct deployment at nominal total pressure

To have a similar reference to all other measurement methods, also the nominal total pressure value is used for a direct triggering mechanism. Point 3 in Figure 21, indicates this instant.

Case 20: Direct deployment at nominal dynamic pressure

The same as for case 19. Since at this phase the vehicle is at relatively low altitude, there is a significant difference between the total pressure and dynamic pressure values. It is investigated whether this will also mean a difference in performance.

Case 21: Total pressure 'switch'

In order to compare pressure readings and g-load readings similar algorithms are tested to investigate if there is a difference in performance due to the reasons mentioned in subparagraph 2.4.3. This total pressure switch, indicated at points 1 and 2 of Figure 22, should be compared to the g switches investigated in case 7 and 8.

Case 22: Total pressure peak value and time

This case is also created to investigate the difference of performance of the measurement method. Since it is expected the pressure peak value has also good correlation to the dispersions, the same algorithm is developed for peak pressure as it is developed for peak g-load in case 6. It is unlikely a pressure probe would be able to directly measure this peak pressure. If such an algorithm should be used, it would be of the drag derived type.

2.5 Sensitivity of the points of interest

All points to investigate are determined. This paragraph will analyze what effect the different dispersions have on the points of interest and how the algorithms correlate to the dispersions. As mentioned in paragraph 2.3 both dispersed and stable points have their own benefits. Important for the dispersed parameters is their correlation. Therefore, besides the dispersion also the correlation will be examined.

2.5.1 Specific contributions of the uncertainties

Table 6 shows the variation of the points of interest influenced by the different contributions of the uncertainty as a percentage of their nominal value. It shows the initial flight path angle has a large contribution for all points. Fortunately this is a parameter which can be correlated very well (see example of Figure 19). The aerodynamic uncertainties have a strong influence on the pressure measurements. This is because the trajectory becomes different because the ballistic coefficient changes. Also the g-load at the parachute deployment has a large dispersion. Its cause is the uniform distribution below Mach 2, as already explained in paragraph 2.3.

Table 6. Sensitivity of the points of interest to specific uncertainties; the dispersions are a 3 σ percentage of the nominal value.

| | Nominal value | Unit | Initial flight path angle | Initial velocity | Initial altitude | Aerodynamic uncertainty | Aoa and bank angle misalignment | Mass uncertainty | Atmospheric variations | All uncertainties |
|---------------------------------------|---------------|------------------|---------------------------|------------------|------------------|-------------------------|---------------------------------|------------------|------------------------|-------------------|
| Time to deployment Mach number | 173.8 | s | 2.91 | 0.108 | 0.404 | 0.418 | 2.541 | 0.149 | 0.156 | 4.36 |
| Dynamic pressure at deployment | 20692 | n/m ² | 1.044 | 0.723 | 0.758 | 7.561 | 9.391 | 3.228 | 1.029 | 14.802 |
| Altitude at Deployment | 16031 | m | 0.299 | 0.118 | 0.111 | 3 | 3.762 | 1.241 | 2.196 | 6.222 |
| G-load at deployment | 3.3709 | - | 0.845 | 0.421 | 0.439 | 28.448 | 9.414 | 0.417 | 0.849 | 32.38 |
| Maximum g-load encountered | 17.477 | g | 2.734 | 0.094 | 0.065 | 0.306 | 5.061 | 0.116 | 3.731 | 7.814 |
| Time to maximum g-load | 132.5 | s | 3.301 | 0.102 | 0.543 | 0.544 | 0.117 | 0.212 | 0.88 | 3.428 |
| Time to 1-g threshold | 89.9 | s | 3.661 | 0 | 0.813 | 1.028 | 0 | 0.403 | 2.089 | 4.28 |
| Time to 2-g threshold | 98.4 | s | 3.661 | 0 | 0.738 | 0.968 | 0.088 | 0.391 | 2.026 | 4.211 |
| Time to 3-g threshold | 103.3 | s | 3.649 | 0.05 | 0.695 | 0.844 | 0.14 | 0.344 | 1.789 | 4.074 |
| Time to first pass 8-g threshold | 115 | s | 3.673 | 0.12 | 0.614 | 0.625 | 0.301 | 0.254 | 0.686 | 3.762 |
| Time last pass 8-g threshold | 155 | s | 2.881 | 0.096 | 0.451 | 0.437 | 0.126 | 0.186 | 0.155 | 2.904 |
| Time to first pass 6-g threshold | 111.4 | s | 3.654 | 0.081 | 0.636 | 0.667 | 0.212 | 0.284 | 1.066 | 3.82 |
| Time last pass 6-g threshold | 160.7 | s | 2.915 | 0.098 | 0.447 | 0.4 | 0.746 | 0.16 | 0.085 | 3.059 |
| Atmospheric density at deployment | 10303 | n/m ² | 0.75 | 0.296 | 0.278 | 7.467 | 9.511 | 3.122 | 4.7 | 15.519 |
| Time to 5000 Pa static pressure | 154.5 | s | 3.351 | 0.131 | 0.448 | 0.771 | 3.039 | 0.306 | 0.554 | 5.215 |
| Time to 7000 Pa static pressure | 162.7 | s | 3.224 | 0.133 | 0.425 | 0.927 | 3.702 | 0.351 | 0.7 | 5.819 |
| Maximum total pressure encountered | 2.01E+05 | n/m ² | 2.73 | 0.097 | 0.065 | 8.47 | 5.094 | 3.249 | 3.744 | 12.383 |
| Time to maximum total pressure | 132.7 | s | 3.318 | 0.093 | 0.53 | 0.52 | 0.113 | 0.26 | 0.821 | 3.426 |
| Time to first pass 60000 Pa threshold | 109.7 | s | 3.659 | 0.038 | 0.652 | 0.217 | 0.191 | 0.106 | 1.243 | 3.789 |
| Time to last pass 60000 Pa threshold | 161.6 | s | 2.911 | 0.093 | 0.448 | 1.28 | 0.838 | 0.49 | 0.09 | 3.395 |

2.5.2 Correlations of the algorithms

In order to have an algorithm which adapts accurately, a strong correlation to the dispersions is desired, although correlation by itself is not conclusive for accuracy. This is because the accuracy is also a function of time. If a last second correction is made, less correlation is needed in order to obtain the same accuracy as a stronger correlating parameter 100 seconds earlier.

It has to be noted only linear regressions are investigated. In some highly dispersed cases, a higher order regression might provide better results, but for the sake of simplicity and to more support this investigation as a proof-of-concept, always just a linear regression will be used.

Figure 23 shows all the correlations from the cases defined in paragraph 2.4. When this figure is compared to Table 6, the importance to make a difference in dispersion and correlation becomes clear: Although the maximum G-load is highly dispersed it is strongly correlated. Such a characteristic promises an algorithm which is both adaptive and accurate.

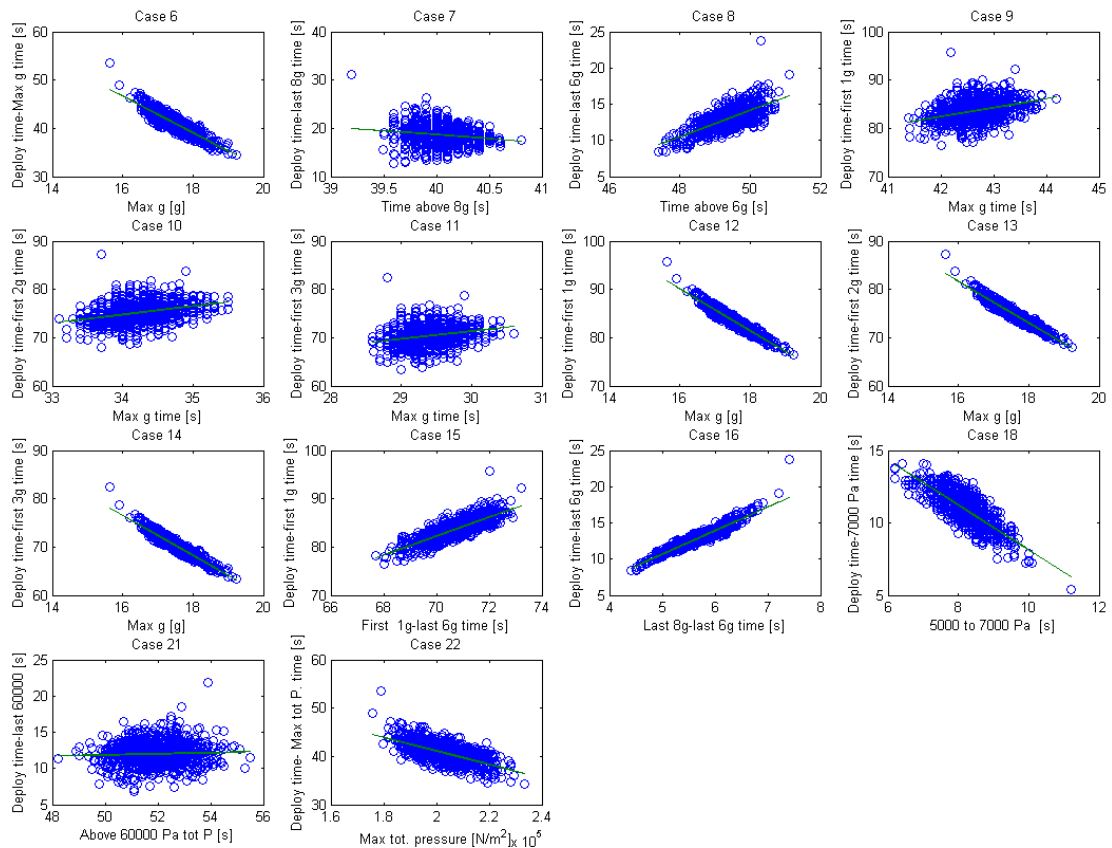


Figure 23. Correlations of the algorithms to the dispersions. Measured values are on the y-axis, desired outputs for each specific measurement principle are on the x-axis.

Table 7 gives an overview of all the cases investigated, with their nominal values and their correlations. All this data is used in FMST to test their performance.

Table 7. The nominal input and output values and thresholds used for all algorithms.

| Case # | First point | Second point | Third point | Correlated with | Value 1 | Unit 1 | Value 2 | Unit 2 | Value 3 | Unit 3 | Value 4 | Unit 4 | Time to trigger | Regres 1st order term | Regres 0th order term | R ² Mach |
|---|---|------------------------------------|-------------|---|----------|------------------|---------|------------------|---------|--------|---------|--------|-----------------|-----------------------|-----------------------|---------------------|
| Timer based | | | | | | | | | | | | | | | | |
| 1 | Nominal time to trigger | - | - | - | 173.8 | s | - | - | - | - | - | - | 173.8 | - | - | - |
| G-load based trigger | | | | | | | | | | | | | | | | |
| 2 | Directly at specific g-load | - | - | - | 3.3709 | g | - | - | - | - | - | - | - | - | - | - |
| 3 | 6g Threshold, last | Time delay | - | - | 6 | g | 160.7 | s | - | - | - | - | 13.1 | - | - | - |
| 4 | 1g threshold, first | Time delay | - | - | 1 | g | 89.9 | s | - | - | - | - | 83.9 | - | - | - |
| 5 | g-peak time | Time delay | - | - | 132.5 | s | - | - | - | - | - | - | 41.3 | - | - | - |
| 6 | g-peak magnitude | g-peak time | Time delay | g-peak time to deployment time | 17.477 | g | 132.5 | s | - | - | - | - | 41.3 | -3.8131 | 107.71 | 0.90717 |
| 7 | G-switch 8g first measurement | G-switch 8g last measurement | Time delay | 8g last measurement to deployment time | 8 | g | 115 | s | 155 | s | - | - | 18.8 | -1.6158 | 83.366 | 0.17862 |
| 8 | G-switch 6g first measurement | G-switch 6g last measurement | Time delay | 6g first measurement to deployment time | 6 | g | 111.4 | s | 160.7 | s | - | - | 13.1 | 1.8353 | -77.599 | 0.72216 |
| 9 | 1g threshold | G-load peak time | Time delay | 1g threshold time to deployment time | 1 | g | 89.9 | s | 132.5 | s | - | - | 83.9 | 1.809 | 6.4902 | 0.39137 |
| 10 | 2g threshold | G-load peak time | Time delay | 2g threshold time to deployment time | 2 | g | 98.4 | s | 132.5 | s | - | - | 75.4 | 1.7711 | 14.591 | 0.34692 |
| 11 | 3g threshold | G-load peak time | Time delay | 3g threshold time to deployment time | 3 | g | 103.3 | s | 132.5 | s | - | - | 70.5 | 1.6276 | 22.555 | 0.26518 |
| 12 | 1g threshold | G-load peak value | Time delay | 1g threshold time to deployment time | 1 | g | 89.9 | s | 17.477 | g | - | - | 83.9 | -4.3366 | 159.51 | 0.96643 |
| 13 | 2g threshold | G-load peak value | Time delay | 2g threshold time to deployment time | 2 | g | 98.4 | s | 17.477 | g | - | - | 75.4 | -4.2707 | 149.95 | 0.96521 |
| 14 | 3g threshold | G-load peak value | Time delay | 3g threshold time to deployment time | 3 | g | 103.3 | s | 17.477 | g | - | - | 70.5 | -4.1511 | 142.99 | 0.95757 |
| 15 | 1g threshold | 6g threshold | Time delay | 6g last measurement to deployment time | 1 | g | 89.9 | s | 155 | s | - | - | 18.8 | 0.97034 | -55.623 | 0.58929 |
| 16 | 8g threshold on declining side | 6g threshold on declining side | Time delay | 6g threshold to deployment time | 8 | g | 6 | g | 155 | s | 160.7 | s | 13.1 | 3.249 | -5.5449 | 0.95744 |
| Static pressure based trigger | | | | | | | | | | | | | | | | |
| 17 | Static pressure | - | - | - | 10302.76 | N/m ² | - | - | - | - | - | - | - | - | - | - |
| 18 | Static pressure 5000 Pa threshold | Static pressure 7000 Pa threshold | Time delay | - | 5000 | N/m ² | 7000 | N/m ² | 154.5 | s | 162.7 | s | 11.1 | -1.5526 | 23.659 | 0.79565 |
| Dynamic/total pressure based trigger | | | | | | | | | | | | | | | | |
| 19 | Directly at specific total pressure | - | - | - | 30994.3 | N/m ² | - | - | - | - | - | - | - | - | - | - |
| 20 | Directly at specific dynamic pressure | - | - | - | 20691.5 | N/m ² | - | - | - | - | - | - | - | - | - | - |
| 21 | 60000 Pa total pressure first measurement | 60000 Pa total pressure last point | Time delay | Total pressure last to deployment time | 60000 | N/m ² | 60000 | N/m ² | 111.4 | s | 160.7 | s | 13.1 | 0.077956 | 7.9828 | 0.053274 |
| 22 | Total pressure peak value | Total pressure peak time | Time delay | Pressure peak time to deployment time | 201353.1 | N/m ² | 132.7 | s | - | - | - | - | 41.1 | -0.00014 | 69.228 | 0.63988 |

2.6 Performance of the algorithms

The 22 algorithms are simultaneously tested using a 10000 run Monte Carlo simulation. The goal of the simulation is to define the dispersions of the Mach number, the altitude and the dynamic pressure at the nominal deployment Mach number of 1.7. Besides determining the dispersions, the failure rate of the algorithm is determined. The algorithm is considered a failure when it triggers the parachute outside of the defined bounds of either one of the Mach number, Altitude or dynamic pressure.

When different measurement methods are compared, g-load measurements and dynamic pressure measurements are similar performing and outperforming barometric measurements by almost a factor 2 on accuracy. These correlated algorithms are compared to single threshold triggers in order to measure their performance, while still excluding sensor noise. Figure 24 shows the Mach number dispersion such a single threshold case and to the best performing correlated algorithm, which is the correlation of two g-load thresholds at the end of the trajectory, which is basically a measurement of the g-load slope.

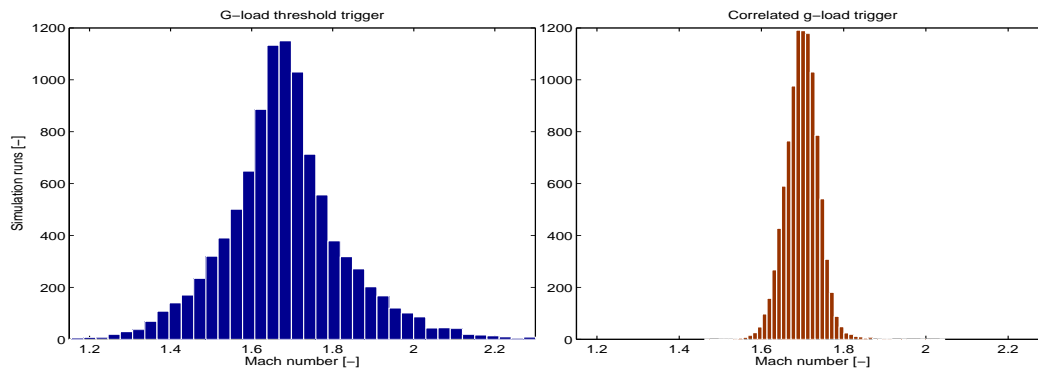


Figure 24. Parachute trigger Mach dispersions. On the left side the Mach dispersion of a single threshold trigger is shown, the right side shows the dispersion of a correlated algorithm

The Figure shows a clear increase in accuracy of the correlated algorithm. If the distribution is approached to be Gaussian, a simple timer has a Mach dispersion of $0.79 \ 3\sigma$, the single threshold trigger a dispersion of $0.44 \ 3\sigma$ and the correlated algorithm had a dispersion of $0.12 \ 3\sigma$. Static pressure measurements show similar improvement, a Mach dispersion of $0.55 \ 3\sigma$ is obtained by a single barometric measurement, whereas a Mach dispersion of $0.22 \ 3\sigma$ is obtained by a correlated barometric algorithm.

Figure 25 shows similar results on the altitude dispersion. The increase of accuracy is less than the Mach estimation, because the correlated algorithm is correlated to the Mach values. The Mach number was chosen to be optimized, because in the study case mission, the Mach opening window was the smallest and therefore the most critical. The altitude dispersions for a timer, a threshold and the g-slope correlation are 2198, 1707 and 996 m 3σ respectively.

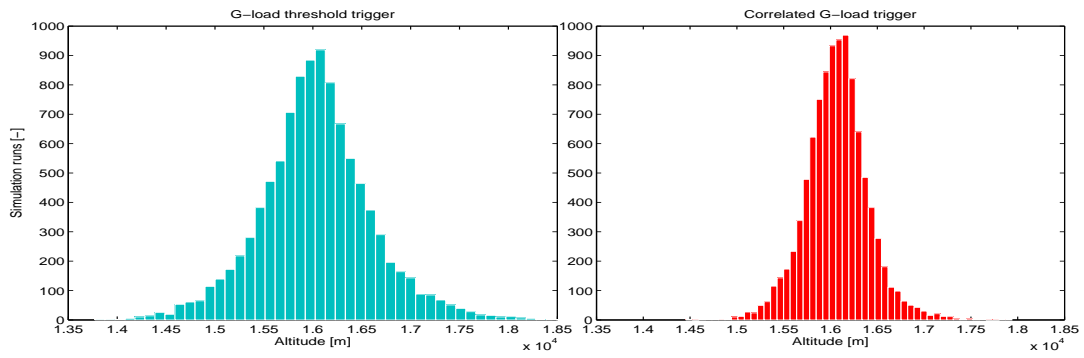


Figure 25. Parachute trigger altitude dispersions. On the left side the altitude dispersion of a single threshold trigger is shown, the right side shows the dispersion of a correlated algorithm.

In Table 8 the results of the entire algorithm performance test is presented. The table has been color coded to show the trade-off choices:

- Green: Compliant (Without considering altitude)
- Blue: Compliant performance, but outperformed by a similar algorithm
- Yellow: Actually not compliant, but used because it is used historically (g-switch and static pressure)

| Case # | Mach 3 σ [-] | Failure rate on Mach [%] | Altitude 3 σ [m] | Failure rate on altitude [%] | Dynamic pressure 3 σ [N/m ²] | Failure rate on dynamic pressure [%] | Total success rate [%] | Total Failure rate [%] |
|--------|---------------------|--------------------------|-------------------------|------------------------------|---|--------------------------------------|------------------------|------------------------|
| 1 | 0.788 | 43.3 | 2198 | 15.94 | 12754 | 39.88 | 49.81 | 50.19 |
| 2 | 0.492 | 34.69 | 1560 | 5.91 | 8314 | 39.95 | 51.17 | 48.83 |
| 3 | 0.443 | 16.83 | 1707 | 8.78 | 5936 | 18.4 | 76.66 | 23.34 |
| 4 | 0.631 | 30.8 | 2095 | 14.43 | 9259 | 32.22 | 61.44 | 38.56 |
| 5 | 0.591 | 27.68 | 2008 | 13.17 | 8481 | 29.64 | 64.49 | 35.51 |
| 6 | 0.258 | 2.45 | 1156 | 2.05 | 4669 | 3.39 | 94.15 | 5.85 |
| 7 | 0.559 | 24.54 | 1946 | 12.3 | 7950 | 23.59 | 69.56 | 30.44 |
| 8 | 0.310 | 5.31 | 1262 | 3.15 | 4907 | 5.82 | 90.26 | 9.74 |
| 9 | 0.585 | 26.72 | 1964 | 12.58 | 8415 | 25.12 | 67.75 | 32.25 |
| 10 | 0.588 | 26.87 | 1969 | 12.69 | 8466 | 25.28 | 67.64 | 32.36 |
| 11 | 0.593 | 27.06 | 1989 | 13 | 8522 | 25.82 | 67.05 | 32.95 |
| 12 | 0.171 | 0.13 | 1072 | 1.31 | 3595 | 0.27 | 98.43 | 1.57 |
| 13 | 0.169 | 0.1 | 1085 | 1.35 | 3534 | 0.2 | 98.46 | 1.54 |
| 14 | 0.182 | 0.2 | 1091 | 1.42 | 3705 | 0.35 | 98.19 | 1.81 |
| 15 | 0.362 | 9.58 | 1403 | 4.68 | 5374 | 9.39 | 85.17 | 14.83 |
| 16 | 0.121 | 0.08 | 996 | 1.1 | 3734 | 0.07 | 98.85 | 1.15 |
| 17 | 0.520 | 23.5 | 461 | 0 | 12668 | 25.7 | 66.98 | 33.02 |
| 18 | 0.221 | 0.83 | 943 | 0.45 | 5788 | 2.44 | 96.64 | 3.36 |
| 19 | 0.308 | 5.72 | 1559 | 6.11 | 2551 | 6.96 | 89.84 | 10.16 |
| 20 | 0.169 | 0.2 | 1301 | 3 | 179 | 0.12 | 97 | 3 |
| 21 | 0.461 | 17.76 | 1801 | 9.68 | 5592 | 17.9 | 76.32 | 23.68 |
| 22 | 0.480 | 19.79 | 1525 | 6.33 | 8321 | 19.74 | 72.46 | 27.54 |

Table 8. The results of all the algorithm performance test.

The success rate varies from 49.81% to 98.85%. This wide range of performance makes it very suitable to perform a trade-off. There is a side note however:

According to this result no algorithm performs within the required success rate of 99.73 (3σ), mainly because the trigger is outside the altitude bounds. This is caused by the high dispersions of the trajectory: In 64 cases the deployment Mach number is located outside the altitude bound, which makes it an immanent failure, such a scenario is thus infeasible for a real life mission and operations. However, for an algorithm trade-off test, the high dispersions are useful to make a clear comparison. The first conclusion which can be drawn is that the non-adaptive algorithms perform significantly less than the adaptive ones. Furthermore it can be seen that g-trigger algorithms outperform pressure based triggers, even though they measure similar features of the g-load and pressure curves. This is because the pressure readings have higher dispersions with trajectory changes. It can also be seen in Figure 23 that pressure based algorithms have less correlation.

A surprisingly well performing algorithm is the direct deployment at a preset dynamic pressure. It does not have the increased uncertainty at the deployment instant as the g-load and the influence of the atmospheric and aerodynamic uncertainties have less impact on the accuracy than static and therefore also the total pressure.

The algorithms based on the g-load peak and the g-load curves slope are the best performing algorithms from the test. These algorithms already showed strong correlation to the dispersions and this correlation leads to compliant results when altitude is not considered. Not considering the altitude is justifiable, because the Deployment is at a high enough altitude; there will always be sufficient time for a complete parachute deployment sequence. For this reason these algorithms are chosen for further investigation.

Furthermore it has to be noted that the difference in performance of the 1, 2 or 3 g thresholds are actually negligible. In this test the 2 g trigger performs best, but even for a 10000 run simulation the differences are too small to give a clear conclusion. Also based on different simulations performed outside the scope of this report showed different winners when slightly different dispersions were used. The choice for the 2 g trigger is not definite and might be changed for secondary reasons, like sensor characteristics.

There are two algorithms which will be investigated further although their performance is not compliant even without considering the altitude, but still significantly outperforming the rest. These are a g-switch base trigger and a pressure based trigger. A g-switch is a very simple separate piece of hardware, which might be used separately from an IMU for redundancy. The same holds for the static pressure based sensor. Because the static pressure measurement is a different one than IMU measurements and a static pressure probe is often carried for other purposes, it is interesting to use this algorithm for further investigation as well.

Figure 26 and Figure 27 visualize the results presented in Table 8. The blue parallelograms in the figures indicate the opening window of the parachute. The size of the deployment field gives an indication of the accuracy of the algorithm, the shape on the way it is correlated.

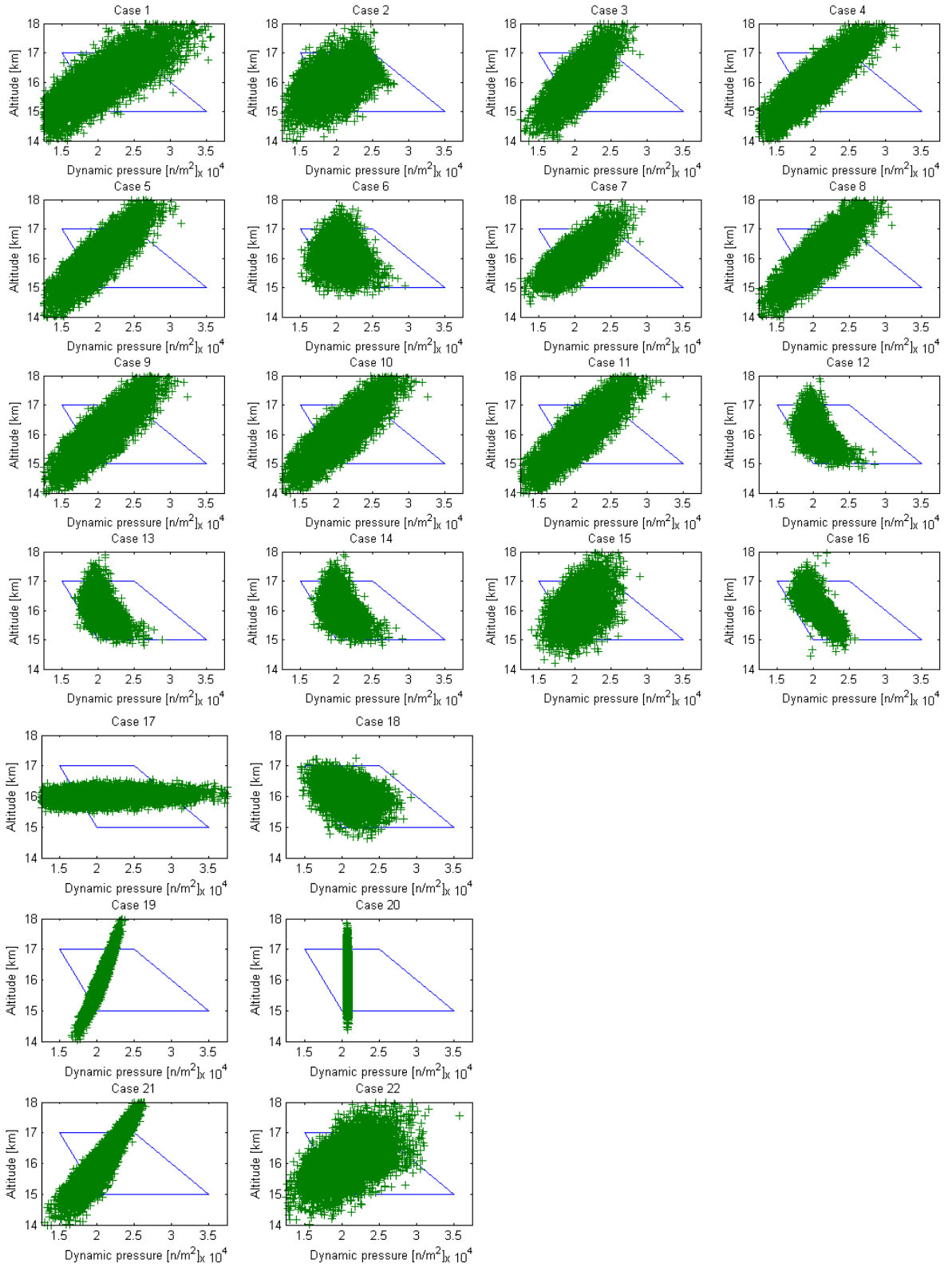


Figure 26. Correlation plots of the parachute opening windows of dynamic pressure and altitude.

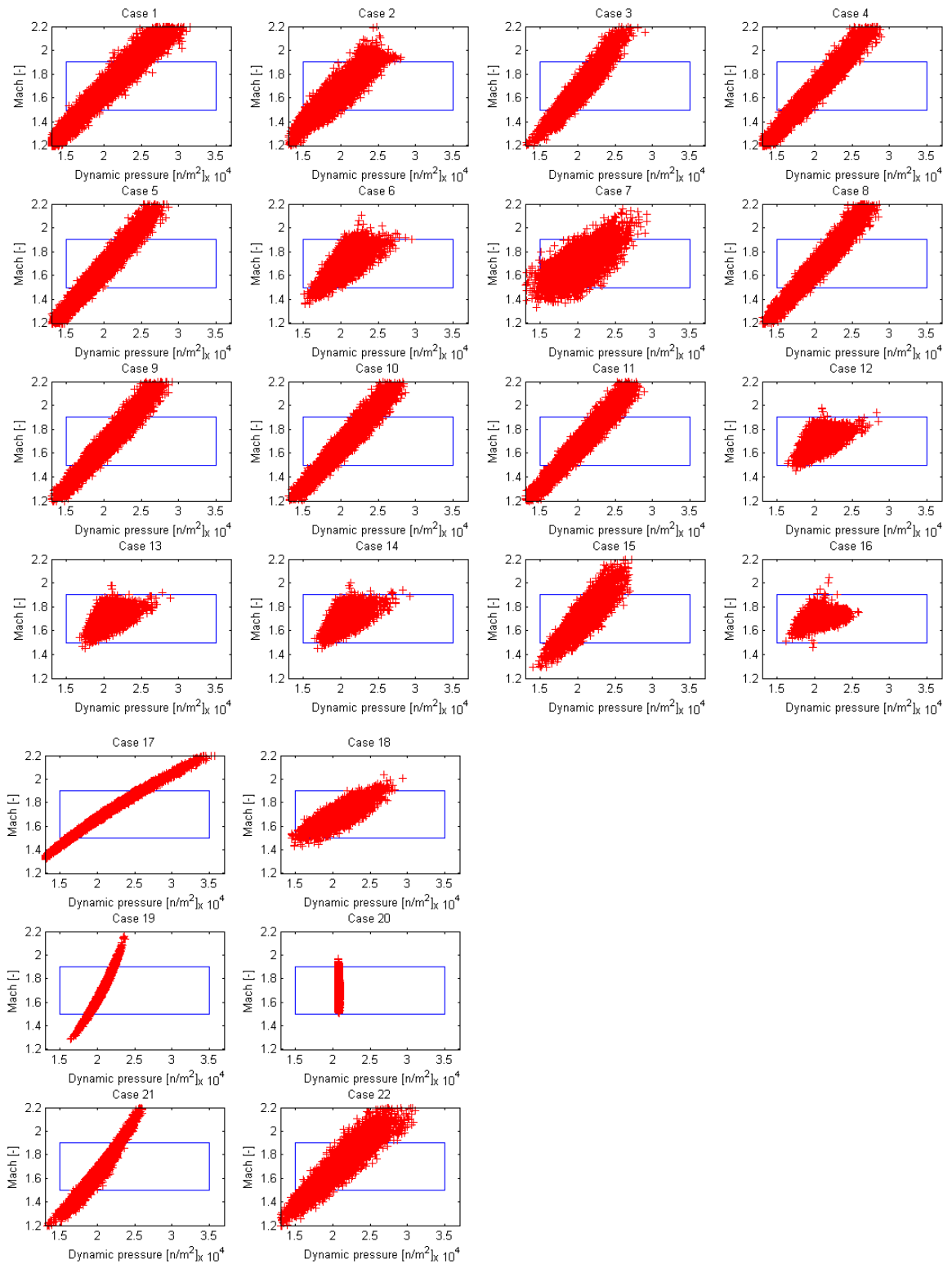


Figure 27. Correlation plots of the parachute opening windows of dynamic pressure and Mach number.

2.7 High fidelity modeling

This paragraph will describe the high fidelity models of the in paragraph 2.6 selected algorithms. In the Flight Mechanics Simulation Tool, the measurement chain is build up to represent the utilized hardware. These models are tested on their Mach estimation performance as a function of the sensor's error using Monte Carlo simulations. Using these models also a non-nominal performance test is performed.

2.7.1 Simulink flow diagram

The high fidelity modeling is done using Simulink model of FMST. The flow diagram in Figure 28 describes the functions in the Simulink model for the 8 to 6 g trigger, but other models work in a similar way. The Simulink code models the sensor and the noise, which is inserted into the threshold detection. When the thresholds are detected a timing sequence and time delay calculation is started using the linear regression function. When the time matches the calculated time, the system sends the deployment signal. All algorithms should contain a premature noise suppression filter: The sensor's noise might unwillingly activate and deactivate a certain threshold and prematurely activate the triggering signal. For example, in this case the threshold trigger will only be activated after the sensors have detected a decrease in g-loads for 2 seconds.

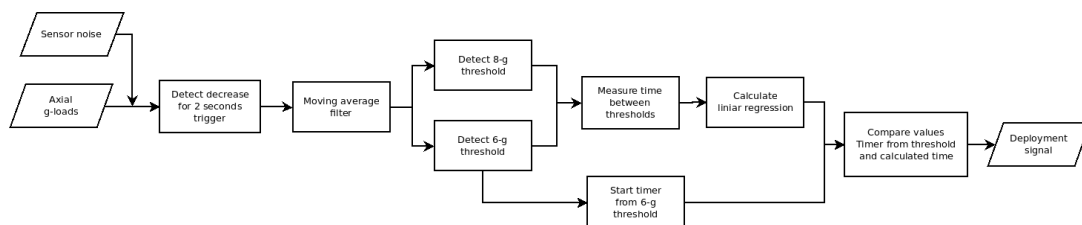


Figure 28. Flow diagram of a high fidelity g-slope triggering algorithm.

Figure 29 shows the Mach dispersion of the g-slope algorithm. For the g-load based measurements it is assumed the sensors' noise amplitude is the dominant error compared to the bias. This assumption is based on the table of sensor data (Table 1). The figure shows a clear linear relation to the sensor noise, when no filter is applied. Such kind of relation can be predicted, since the algorithm will be activated directly at the first moment when the sensor hits the threshold value. So when the noise is increased, it will automatically lead to a higher deviation is measured threshold time, which will lead to a constant increase of the dispersions. The sensor noise range between 0.05 and 0.2 g is a realistic range of sensor specifications; based on the knowledge the Huygens probe sensor has a noise of $0.05 \text{ g } 3\sigma$. At this sensor noise value, the Mach dispersion is increased by around 33 %.

The advantage of these correlated algorithms together with a time delay with respect to the 'immediate deployment triggers', is that there is time to apply sensor filtering to increase the measurement performance and as can be seen in Figure 29, using a simple 10 point averaging filter, the Mach dispersion will increase about 25

percent, even when very noise sensors are used. To conclude, using algorithms with a time delay trigger reduces the requirements for the sensors.

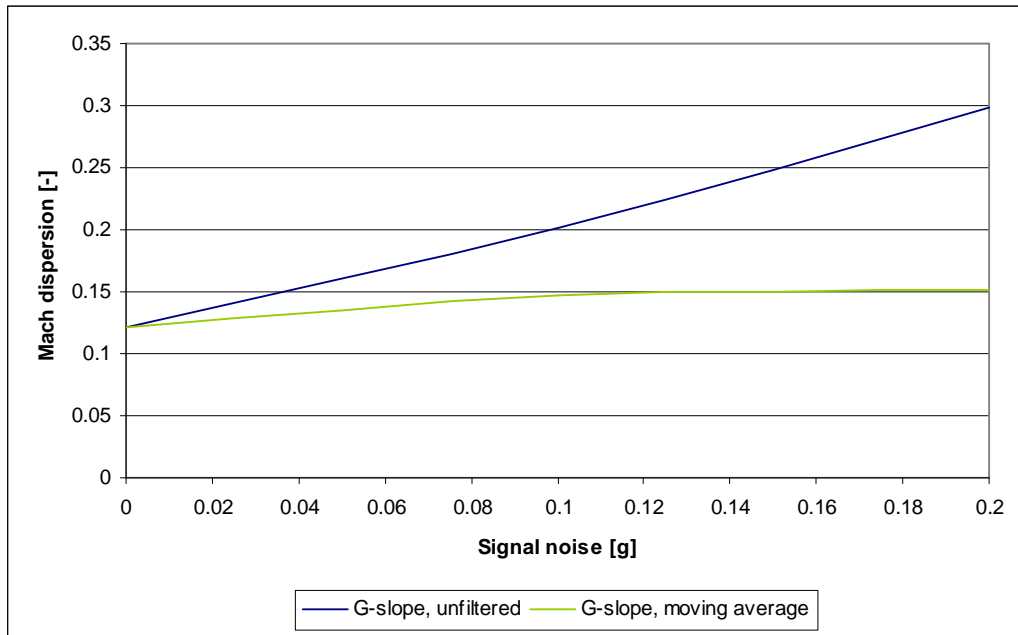


Figure 29. Mach dispersion as a function of the sensor's noise, with and without the use of a filter.

2.7.2 Nominal and off-nominal trajectory high fidelity modeling results

In Figure 30 the performance of the in paragraph 2.6 selected g-load based algorithms are presented. Furthermore, a potential off-nominal scenario performance is shown. The first thing to notice is a factor of 2 increase of the Mach dispersion with the estimation of the dynamic pressure using a drag derived Mach estimation method. In this particular case, uniform distribution of the aerodynamic uncertainty below Mach 2 is the main contribution of the significant reduction in accuracy. Analysis performed on the lifting re-entry as described in subparagraph 3.3.2 will elaborate more on the dispersions using drag derived measurement methods.

All algorithms use value average filters except the dynamic pressure estimation, because it triggers the deployment directly at certain pressure threshold. This can of course be improved by estimating values some seconds before deployment, but the nearly horizontal line displayed in the figure, indicates that the effect of sensor noise is negligible compared to the error induced by the uniformly distributed aerodynamic uncertainty below Mach 2.

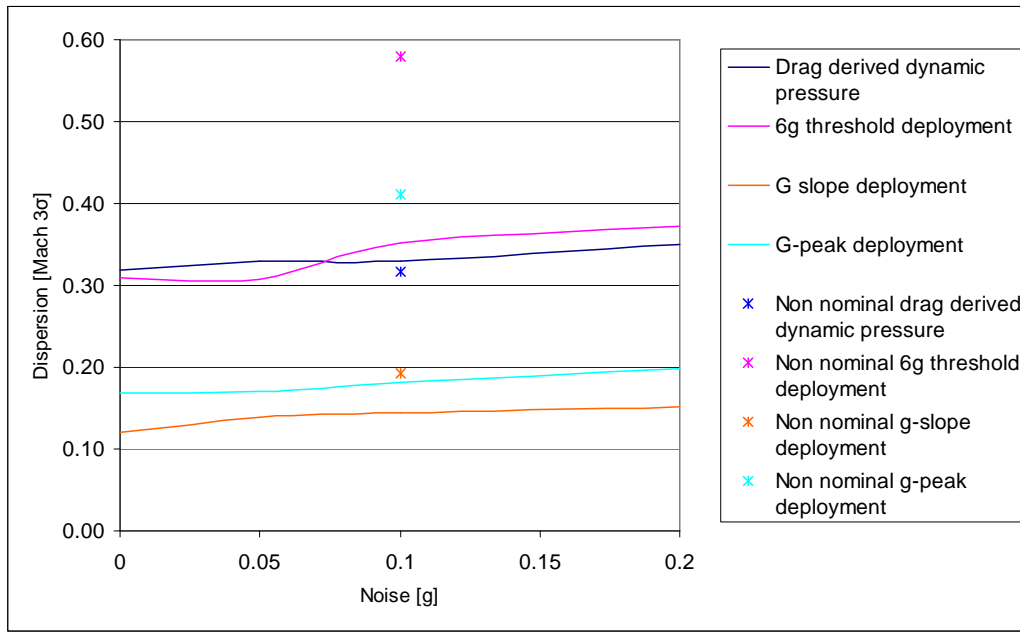


Figure 30. Results of the high fidelity modeling of g-load based triggering systems.

Figure 31 (left) shows the alternative triggering scenario besides g-load based triggering; the static pressure algorithm which was also considered in paragraph 2.6. It is not possible to directly compare g-loads sensor to pressure sensors, because a different unit is measured. Furthermore, the pressure sensor accuracy is according to Table 1 more depended on the total measured range. The pressure sensor information found indicated a 1% full scale error. In this case static pressure measurements are required up till 7000 Pa, indicating only a 70 Pa error. However it is very likely the mission will require a pressure sensor capable of measuring higher pressures as well and compromises on the accuracy. During the Huygens mission this was partially omitted by using a scalable pressure sensor. But still in the finest setting of this specific sensor an error of 400 Pa was present. This value can be seen as a realistic first assumption. For this reason also the off-nominal analysis was run using a 400 Pa error. As displayed in Figure 31, the off-nominal dispersion does not become a dominant factor in the static pressure measurements. This would make it reliable alternative triggering method.

Figure 31 (right) shows a continuous updating Mach drag derived estimation method, with an applicability more aimed on lifting re-entries, see subparagraph 3.3.2. If such a method is used, unprecedented accuracy could be achieved and since it determines the conditions independently of the initial conditions, the off-nominal de-orbiting does not influence the quality of the measurement. The drag derived measurement accuracy is dominated by the velocity estimation bias. For this reason this is presented in this figure. A more complete sensitivity analysis on drag derived measurements can be found in subparagraph 3.4.1.

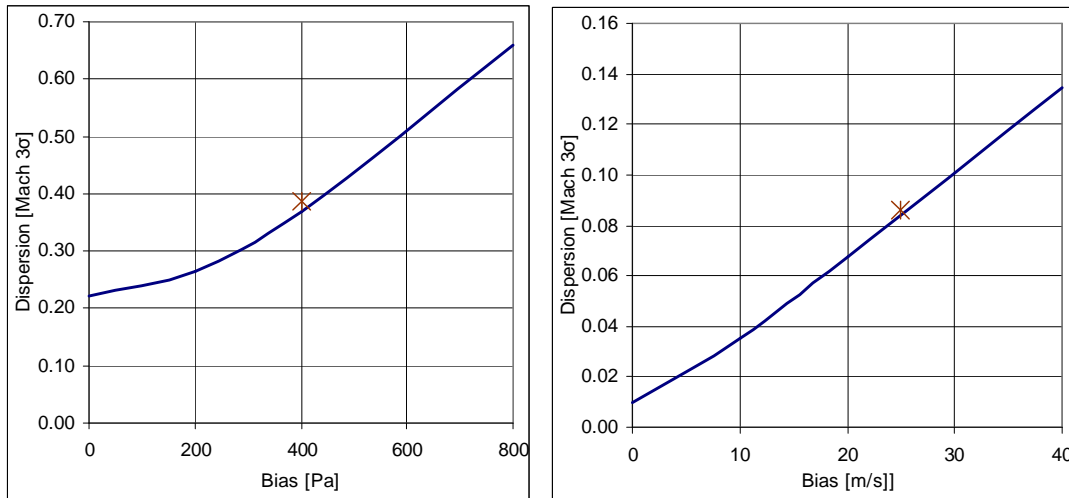


Figure 31. Results of the high fidelity modeling of a static pressure triggering mechanism (left) and a drag derived measurement system (right).

For a ballistic re-entry, off-nominal cases are rare, because the re-entry itself is uncontrolled. However, due to de-orbit anomalies, the initial conditions can induce a situation different than intended. This off-nominal situation induces higher flight path and initial velocity dispersions. Such a scenario can also easily be tested using Monte Carlo analysis. The following off-nominal scenario has been tested:

| Flight path angle | +1 | -1 | deg | Gaussian 3σ |
|-------------------|------|------|-----|--------------------|
| Velocity | 7300 | 7530 | m/s | Uniform |

Table 9. Off-nominal de-orbiting initial re-entry conditions.

In reality, the flight path angle and the velocity are correlated parameters: If the vehicle is de-orbited and it would run out of fuel to quickly, the orbital velocity will still be higher than intended; the re-entry will ‘overshoot’ its nominal trajectory and this in term leads to a shallower flight path angle. For the sake of simplification, the Monte Carlo analysis is performed using these variables as being independent. This will actually lead to a more conservative result, since it will create a broader range of scenarios than it would be practically possible.

For this scenario a timer would have an unusable large Mach dispersion of 2.6771 at 3σ and a single threshold trigger, without sensor noise would have a dispersion of 0.5016 at 3σ , which most likely means a parachute failure.

2.8 Conclusions on the ballistic re-entry algorithm development

For a ballistic re-entry, multiple accurate triggering algorithms can be used with different types of sensors. Using 2 measurement points which are correlated with DLS activation time, can improve the accuracy 2 to 3 times to non correlated single threshold triggers and timers.

Correlation points can be selected on points with low dispersion to have a ‘stable’ point or with high dispersion to have maximum adaptivity to the dispersions. Correlation of two highly dispersed parameters can lead to less accurate results, e.g. correlating the g-peak time and the g-peak value.

The g-load curve has higher correlations than the pressure curve, because the atmospheric variations influence the pressure measurements which are uncorrelated to the actual flight path dispersions, while measuring the deceleration is not influenced by the uncorrelated variation of an external medium. It appears that measuring the g-load slope just before deployment and measuring the g-load peak have the best correlation and the most accurate results, but not compliant to the primary goal of a 3σ (99.7%) success rate. With the scenario set, compliance is impossible, because the dispersions are such that in 64 out of 10000 cases the deployment Mach number is located outside the altitude bound, which makes it an immanent failure. For performance comparison purposes, this poses no problem.

Measuring or estimating the dynamic pressure and deploy at a preset setting is an exception for a not correlated algorithm to perform compliant to a less than 3σ failure, when altitude is not taken into account, but physically measuring this pressure will be very challenging. Furthermore static pressure probes perform not compliant, but are not ruled out for usage because of the possibility to use it as redundant sensors.

More accurate results could be obtained by last second adjustments. The aerodynamic uncertainty region increases at Mach 2.0, because the flow properties change stronger in this region until the subsonic flow regime. There should be a measurement point within this region to obtain more accurate results. From Mach 2 to the nominal 1.7 takes around 3 seconds. Drag derived measurement is a continuous estimation method which delivers this accuracy, but is more complex. Furthermore higher order regressions might be used to adapt to high dispersed or non-nominal situations.

High fidelity models of the best performing algorithms are incorporated in the Simulink structure to model the sensor characteristics. It showed that performance decreases due to the sensor error, but this decrease can be limited by using filtering. The high fidelity model also showed that accuracy of the dynamic pressure estimation by measuring the deceleration decreased the accuracy by a half. Finally an off-nominal scenario was set up to show that these adaptive algorithms are also able to manage a degraded de-orbit maneuver.

For the Earth ballistic re-entry it can be concluded that correlated algorithms outperform the current used threshold triggers on accuracy and the ability to adapt to off-nominal de-orbiting. Furthermore, adding a time delay between the measurement and the actual deployment has the benefits of providing processing time for noise reduction and removing the axial g-load measurement error for possible angle of attack oscillations divergence.

One of the developed correlated g-load algorithms was tested on the EXPERT mission 6 DOF model and proved to have a far superior performance over the current design and could also cope with an off-nominal scenario.

3 The lifting re-entry case

The lifting re-entry study case is based on the Horus-2b study vehicle⁷, which is depicted in Figure 32. This specific vehicle has a weight which is too high a conventional parachute utilization; however the ballistic coefficient will be comparable for smaller sized vehicles, so the trajectory is representative for 'generic' re-entry vehicles.

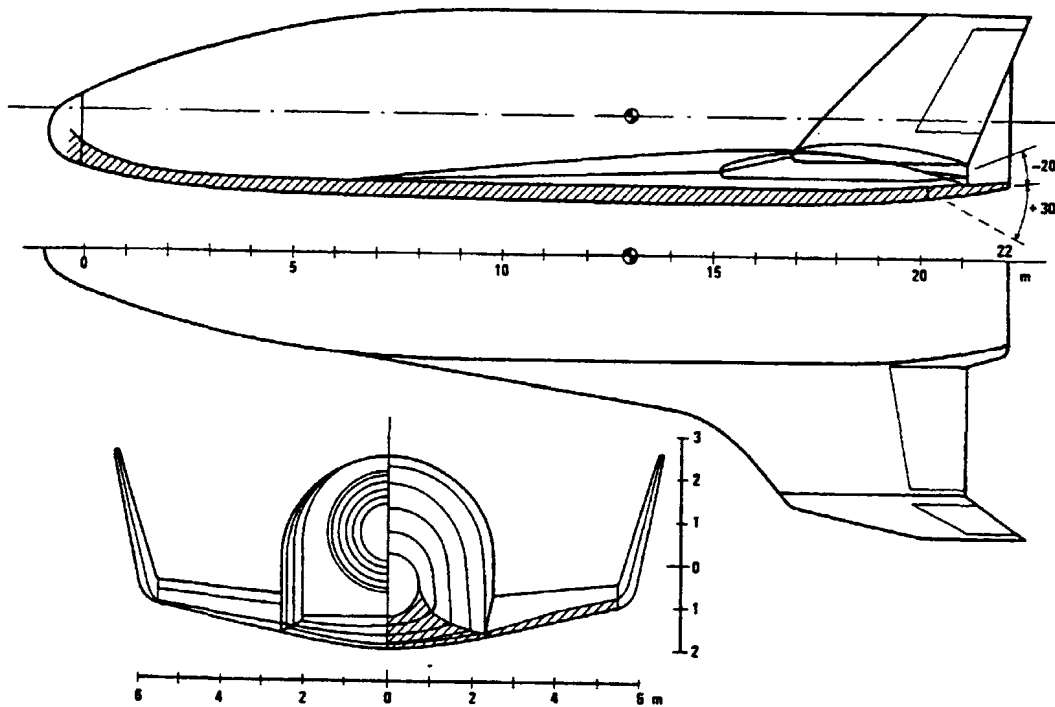


Figure 32. *The Horus-2b re-entry vehicle*⁷.

Estimating the deployment conditions for a lifting re-entry will be significantly different from a ballistic re-entry because the vehicle is actively controlling its flight path. This means the estimation does not depend from the initial conditions and the dispersions, but also on the guidance, navigation and control (GNC). For this reason it is not possible to correlate input and output conditions from some known corridor of initial conditions: The vehicle has to estimate its state and the atmosphere based on the conditions it is flying in at that moment. For this reason, more input parameters will be required, but on the other hand, more parameters will be available because they are necessary to navigate the vehicle. Since the vehicle will continuously estimate its state, the uncertainties of initial conditions do not influence the performance of the measurement. However, in order to obtain realistic estimation values, sensor errors will be introduced.

3.1 *The lifting re-entry flight path*

Major features of the re-entry trajectory are presented in the combined plot of Figure 33. These features are considered to be the nominal trajectory. However, this

flight path is not fixed and the GNC system will decide how to fly during flight, so deviations of this flight path are likely to be present, although those are not considered to be off-nominal maneuvers.

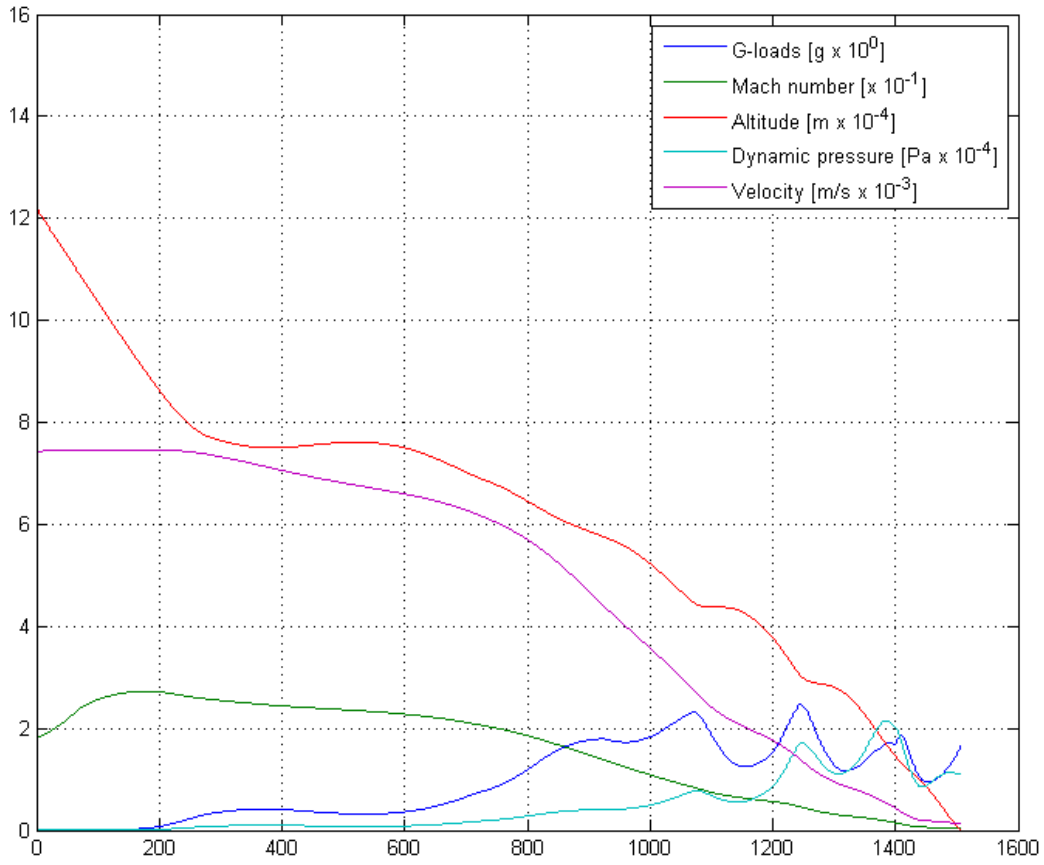


Figure 33. The Earth lifting re-entry profiles. All y-axis values are multiplied by the value provided in the legend.

For the Monte Carlo analysis, only the terminal descent from Mach 2 is used, because the Mach measurement is continuous and does not depend on the path flown before. This way also the modeling of the navigation is omitted and navigation performance model results for the final phase of the flight are applied. Table 10 defines the main vehicle and scenario characteristics:

| Nominal conditions lifting re-entry | | Lower limit | Upper limit | Distribution | Unit | Remark |
|-------------------------------------|--------------|-------------|-------------|--------------|----------------|---|
| Vehicle | Horus 2b | | | | | |
| Mass | 26029 | -780.87 | 780.87 | 3 σ | kg | |
| Inertia matrix | See Table 11 | | | 3 σ | % | |
| S ref | 110 | | | 3 σ | m ² | |
| c ref | 23 | | | 3 σ | m | |
| b ref | 12 | | | 3 σ | m | |
| Aerodynamic | | | | | | See Table 12 and Table 13 |
| ΔCA | - | -4 | 4 | 3 σ | % | This parameter defines only the dispersion, the aerodynamic value itself is calculated during the |

| | | | | | | |
|-------------------------------------|---|-------|------|-----------|------------------|--|
| | | | | | | simulation |
| ΔCN | - | -9 | 9 | 3σ | % | This parameter defines only the dispersion, the aerodynamic value itself is calculated during the simulation |
| Scenario | GEO position NED (North Eastern Down) speed, VEL attitude | | | | | |
| Altitude | 24621.111 6 | 500 | 500 | 3σ | m | |
| Latitude | 5.6293 | 0 | | | deg | Is only applicable for footprint |
| Longitude | -52.9478 | 0 | | | deg | Is only applicable for footprint |
| Velocity | 610.8619 | -10 | 10 | 3σ | m/s | |
| Heading | 94.8516 | 0 | | | deg | Is only applicable for footprint |
| Flight path angle | -3.6067 | -1.5 | 1.5 | 3σ | deg | |
| Attitude | | | | | | |
| alpha | 16 | -2.5 | 2.5 | | deg | |
| beta | 0 | | | | deg | |
| phi_aero | 50 | -10 | 10 | | deg | |
| roll_dot | 0 | | | | deg | |
| pitch_dot | 0 | | | | deg | |
| yaw_dot | 0 | | | | deg | |
| Sensors | | | | | | |
| alpha bias | 0 | -2 | 2 | 3σ | deg | |
| Velocity bias | 0 | TBD | TBD | 3σ | m/s | To be varied to determine IMU performance |
| Velocity noise | 0 | -5 | 5 | 3σ | m/s | TBC, Integrated values do not contain a lot of noise |
| Acceleration | 0 | -0.06 | 0.06 | 3σ | g | Value taken from Huygens mission |
| Environment | | | | | | |
| Atmosphere US 76 | | | | | | GRAM based model atmospheric uncertainties |
| Parachute opening conditions | | | | | | |
| Altitude | 24000 | - | - | NA | m | |
| Mach number | 1.6 | - | - | NA | - | |
| Dynamic pressure | | - | - | NA | n/m ² | |
| Simulation properties | | | | | | A basic earth model is used with J2 gravitational model |
| Solver | ode 4 | | | | - | |
| Time start | 0 | | | | s | |
| Time step | 0.1 | | | | s | Fixed time step |
| Relative tolerance | 1.00E-05 | | | | - | Not used for ODE 4 |
| Absolute tolerance | -1 | | | | - | Not used for ODE 4 |
| Scope decimation | 1 | | | | s | |
| Julian date | 2455742.5 | | | | - | 30 june 00:00 UTC |

Table 10. Simulation initial conditions and uncertainties of the Monte Carlo simulation.

Parameters not listed in the table are the inertia matrix and the aerodynamic database. They are provided below:

| Inertia matrix | | kg*m ³ |
|----------------|--------|-------------------|
| 119000 | 0 | 0 |
| 0 | 769000 | 0 |
| 0 | 0 | 806000 |

Table 11. The inertial matrix of the Horus 2b vehicle.

The aerodynamic characteristics are depended on the Mach number and the angle of attack. The following table lists the C_D and the C_L values used:

| M→ AoA ↓ | 1.2 | 1.5 | 2 | 3 | 5 | 10 | 20 | 30 |
|-------------|----------|----------|----------|----------|----------|----------|----------|----------|
| 0 | 0.10112 | 0.083694 | 0.076711 | 0.074968 | 0.067994 | 0.066242 | 0.05056 | 0.05056 |
| 5 | 0.124984 | 0.095346 | 0.083151 | 0.072699 | 0.063964 | 0.063964 | 0.048291 | 0.048291 |
| 10 | 0.199444 | 0.141902 | 0.112272 | 0.093085 | 0.08435 | 0.077386 | 0.059969 | 0.059969 |
| 15 | 0.329685 | 0.233787 | 0.181484 | 0.148341 | 0.125667 | 0.116941 | 0.087347 | 0.087347 |
| 20 | 0.520947 | 0.362285 | 0.285565 | 0.231518 | 0.200118 | 0.182702 | 0.14609 | 0.14609 |
| 25 | 0.774963 | 0.541334 | 0.426258 | 0.347821 | 0.304244 | 0.283322 | 0.236249 | 0.236249 |
| 30 | 1.08477 | 0.765712 | 0.607068 | 0.502461 | 0.448397 | 0.422254 | 0.357756 | 0.357756 |
| 35 | 1.08477 | 1.02671 | 0.820976 | 0.69197 | 0.622233 | 0.597816 | 0.51937 | 0.51937 |
| 40 | 1.08477 | 1.32083 | 1.06628 | 0.90764 | 0.825681 | 0.787343 | 0.710623 | 0.710623 |
| 45 | 1.08477 | 1.32083 | 1.3325 | 1.14596 | 1.05355 | 1.0152 | 0.922805 | 0.922805 |

Table 12. The C_D database of the Horus 2-b vehicle.

| M→ AoA ↓ | 1.2 | 1.5 | 2 | 3 | 5 | 10 | 20 | 30 |
|-------------|----------|----------|----------|----------|----------|----------|----------|----------|
| 0 | -0.00632 | -0.02727 | -0.02968 | -0.02968 | -0.03434 | -0.03901 | -0.04137 | -0.04137 |
| 5 | 0.269892 | 0.164899 | 0.108903 | 0.066906 | 0.045835 | 0.027218 | 0.003934 | 0.003934 |
| 10 | 0.564819 | 0.361857 | 0.261483 | 0.196154 | 0.147157 | 0.121468 | 0.072496 | 0.072496 |
| 15 | 0.869103 | 0.579766 | 0.435085 | 0.330092 | 0.269454 | 0.236742 | 0.162128 | 0.162128 |
| 20 | 1.1827 | 0.802365 | 0.611021 | 0.480363 | 0.401035 | 0.363681 | 0.277353 | 0.277353 |
| 25 | 1.1827 | 1.01794 | 0.784623 | 0.632943 | 0.544306 | 0.499976 | 0.399674 | 0.399674 |
| 30 | 1.1827 | 1.21487 | 0.951202 | 0.780881 | 0.682864 | 0.640866 | 0.531231 | 0.531231 |
| 35 | 1.1827 | 1.38614 | 1.09678 | 0.914771 | 0.81216 | 0.763187 | 0.667479 | 0.667479 |
| 40 | 1.1827 | 1.38614 | 1.20968 | 1.01835 | 0.918004 | 0.871389 | 0.780395 | 0.780395 |
| 45 | 1.1827 | 1.38614 | 1.28995 | 1.09394 | 0.995971 | 0.95164 | 0.86298 | 0.86298 |

Table 13. The C_L database of the Horus 2-b vehicle.

3.2 Flight path dispersions

The initial conditions lead to the flight path characteristics shown in Figure 34 and Figure 35. Ten Monte Carlo simulations are presented to make the dispersions visible. Jumps in the g-loads originate from abrupt changes in the aerodynamic database.

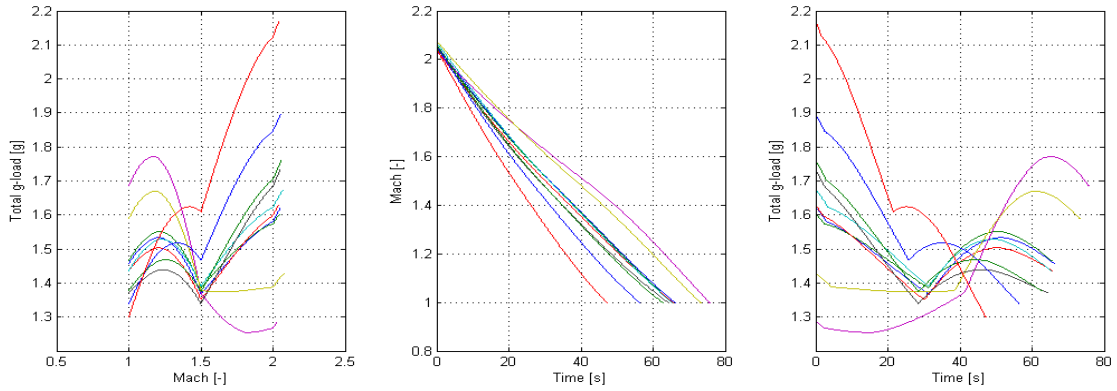


Figure 34. *G-load dispersions by Monte Carlo simulation.*

The lapse of the static pressure has less correlation to the horizontal velocity and Mach number estimation as the ballistic re-entry type. This is because the flight path angle is much shallower compared to the ballistic flight path angle and is more dispersed. This will make correlations for static pressure measurements less accurate. The dynamic pressure looks more suitable for correlation for Mach estimation, compared to the jumps in the g-loads and the highly dispersed static pressure.

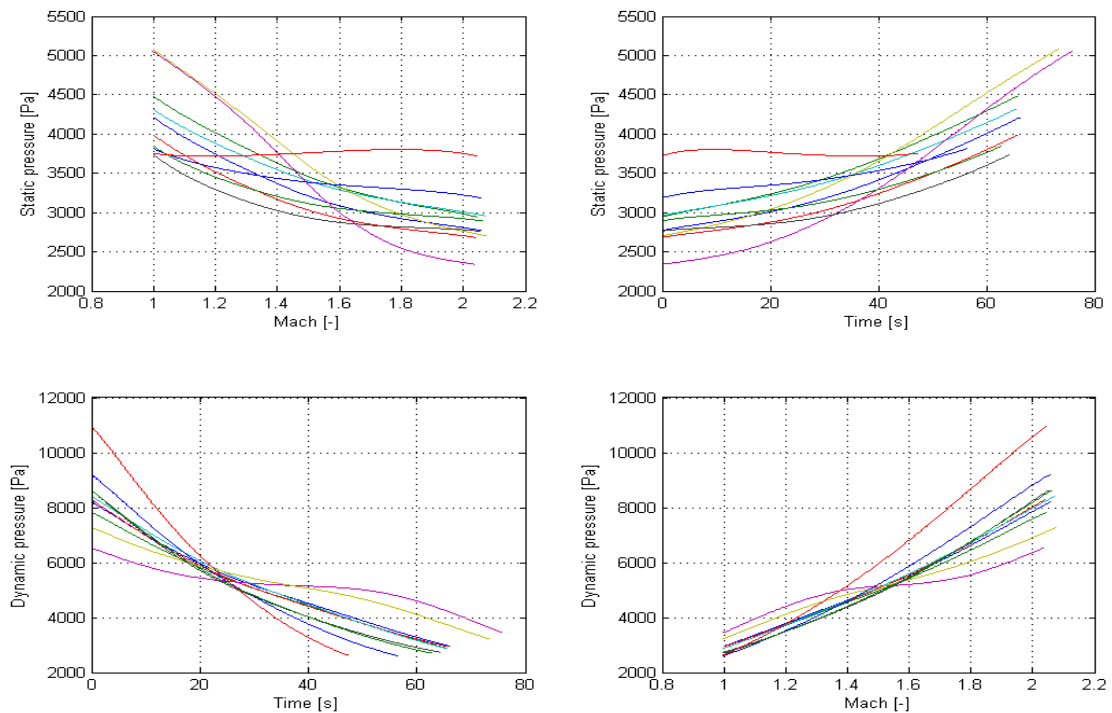


Figure 35. *Pressure dispersions by Monte Carlo simulation.*

3.3 Measurements used

For the lifting re-entry different measurements and methods will be used as for the ballistic re-entry, because the measurement methodology will be very different. The

systems or tools useful for determining the parachute opening window investigated are:

- IMU providing:
 - o Acceleration in axial direction
 - o Velocity
 - o Angle of attack
- Databases:
 - o Aerodynamic
 - o Atmosphere
- GPS providing:
 - o Velocity
 - o Altitude
- Static pressure probe
- Temperature probe

Using these tools, different types of measurement methods can be developed:

- Drag derived measurement, using the deceleration measured by the IMU to estimate the environment. Using the integrated deceleration the IMU can estimate the velocity, or GPS can be used to determine the velocity. An on-line knowledge of the aerodynamic database is necessary.
- Drag derived measurement to estimate velocity. In this case static pressure is measured to know the environmental conditions. With the use of the deceleration of the IMU and the equation of the dynamic pressure, the velocity is estimated. An on-line knowledge of the aerodynamic database is necessary.
- Velocity-constant temperature mach estimation: In this case only the velocity is determined by either the IMU or GPS and the speed of sound is considered to be constant along the altitude. This can be done thanks to the vehicle specific fact the DLS activation occurs at altitude range where the temperature gradient is almost vertical.
- Static pressure only. This measurement does not provide information about the velocity, but does not require the IMU or GPS, which might make it suitable as a back-up trigger hardware.
- Temperature measurements might be useful to determine the Mach number, from which information of the environment is required.

3.3.1 Quick measurement system trade-off

Without looking directly to the numbers, a qualitative overview can be made on the performance of different sensor systems. Desirable characteristics on parachute triggering sensors are:

- Predictability. The system should be modeled and analyzed prior to flight.
- Implementability, considering the interaction with the flow. Because of the extreme conditions during the re-entry, the sensor system should be able to survive these conditions
- Expected accuracy. Because the parachute and the vehicle have constraints on structural strength and stability, the conditions should be sufficiently accurate.

- Reliability. Because failure of the system means the vehicle will most likely crash to destruction, the system should be very reliable/redundant.

A simple performance scoring system is applied, only to give an indication what is necessary in order to develop a specific system. The scores are:

- 3: Desired performance or minimum development work required
- 2: Possible sufficient performance or more investigation required
- 1: Likely to be underperforming or complex to implement

| | Minimum flow knowledge required | Minimal flow interaction | Expected accuracy | Reliability |
|-----------------------------|---------------------------------|--------------------------|-------------------|-------------|
| Inertial measurement | 2 | 3 | 3 | 2 |
| GPS | 3 | 3 | 3 | 1 |
| Static pressure measurement | 1 | 2 | 1 | 3 |
| Total pressure measurement | 1 | 1 | 3 | 2 |
| Temperature measurement | 1 | 2 | 1 | 3 |

Table 14. Quick trade-off table for different methods of measuring the deployment conditions.

For estimation of the dynamic pressure using inertial measurements, the drag coefficients should be known. For this reason, knowledge of the flow around the vehicle is required. However, for pressure and temperature sensors, local disturbances around the probes can create faulty measurements, so for these kinds of measurements, the flow should be understood on local level, so the score is lower as inertial measurements. Since GPS does not require any aerodynamic information, it scores the highest.

Both inertial measurements and GPS do not require interaction with the flow, no probes have to be developed which has to withstand the extreme re-entry conditions. Static pressure and temperature are not fully exposed to the flow and it should be possible to design probes able to cope with these conditions, static pressure probes have been used before. Temperature probes have not been used yet for parachute triggering, but it can provide information about the flow. More analysis will be needed for such as system, since the afterglow of the vehicle is often not very thoroughly analyzed. A total pressure probe should be fully exposed to the hypersonic flow at stagnation point; up till now this has never been done before, except deployable pressure probes to be used in a later phase of the re-entry.

Scoring on the expected accuracy is based on the first analysis performed. Inertial measurements, GPS and a total pressure probe are both capable of performing accurate estimates of the velocity, which is a driving parameter for parachute deployment. Static measurements can support these measurements or provide an estimation of the altitude, but that does not necessarily imply suitable deployment conditions.

Reliability is a killer requirement for parachute triggering mechanisms, because it is a mission critical item. GPS is depended on the signals received from the satellites. During the blackout phase of the re-entry this signal cannot be received due to ionization of the air surrounding the vehicle. After this blackout the signal should be acquired fast enough in order to be useful for the velocity estimation. This signal acquiring time is very hard to predict. For this reason GPS on itself is not suitable for

parachute triggering, but the hardware will be available anyway and it scores very well on other items it might be considered as a backup. Static measurements score high because these kinds of sensors have been used before on most flight, which increases confidence on its functionality. A total pressure probe will be mechanically more challenging, which decreases its reliability. Inertial measurements are performed using an IMU, which is a complicated device, but is used in most missions because it is used to control the vehicle. Because static measurements are considered to be very reliable, it makes it an interesting back-up opportunity.

3.3.2 Drag derived measurements

A method to estimate flight conditions with a non intrusive measurement is drag derived (altitude) (DD(A)). The DDA measurement is a means of estimating the altitude by combining the measurements of aerodynamic (or non-gravitational) accelerations, aerodynamic and atmospheric models¹⁶. With the altitude estimation the standard atmospheric temperature and thus the Mach number can be estimated.

The non-gravitational component of the deceleration is extracted from the IMU (x-direction, Figure 36) and together with the vehicle's mass, reference area, its longitudinal axis aerodynamic force coefficient and the integrated velocity; the air density can be estimated using Eq. (1). Using a standard atmosphere profile, an estimation of the altitude can be made. The benefit of using the axial component of the acceleration is that it is independent of bank angle reversals. Figure 36 on the left shows the magnitude of the g-force, the peaks in the curve depend on the turns flown commanded by the navigation system; these can be very different per flight. Figure 36 on the right shows the g-loads separated in components, which shows the body-axis x-component as a useful parameter to estimate the dynamic pressure.

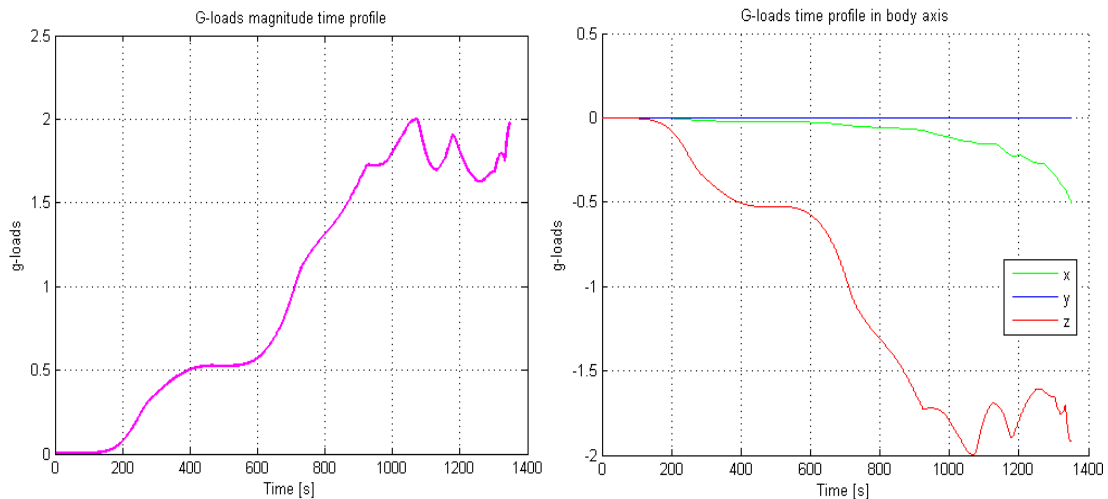


Figure 36. Total g-load curve (left) and g-load curves separated in components (right).

Drag derived measurement uses an estimation of the dynamic pressure through the acceleration and the aerodynamic database. From the dynamic pressure the air density is calculated. Using a standard atmosphere lookup table, either the

atmospheric temperature or pressure is determined and this way the local speed of sound is determined. The estimation is described in the following equation:

$$P_{dyn} \approx \frac{m \cdot \Gamma}{S_{ref} \cdot C_A} = \frac{1}{2} \cdot \rho \cdot V^2 \quad (1)$$

Γ and V are extracted from the IMU; C_A is extracted from a database and is a function of the Mach number and the angle of attack. The angle off attack can be also be estimated by the navigation system or is extracted from another database which contains the angle of attack as a function of the velocity and the position of the control surfaces. The Mach number is used from the previous time-step. Since the C_A does not change rapidly with respect to the Mach number and the estimation cycle frequency is high enough, the use of the previous time step value can be justified.

This calculation procedure is inserted into the Simulink model according to the following scheme:

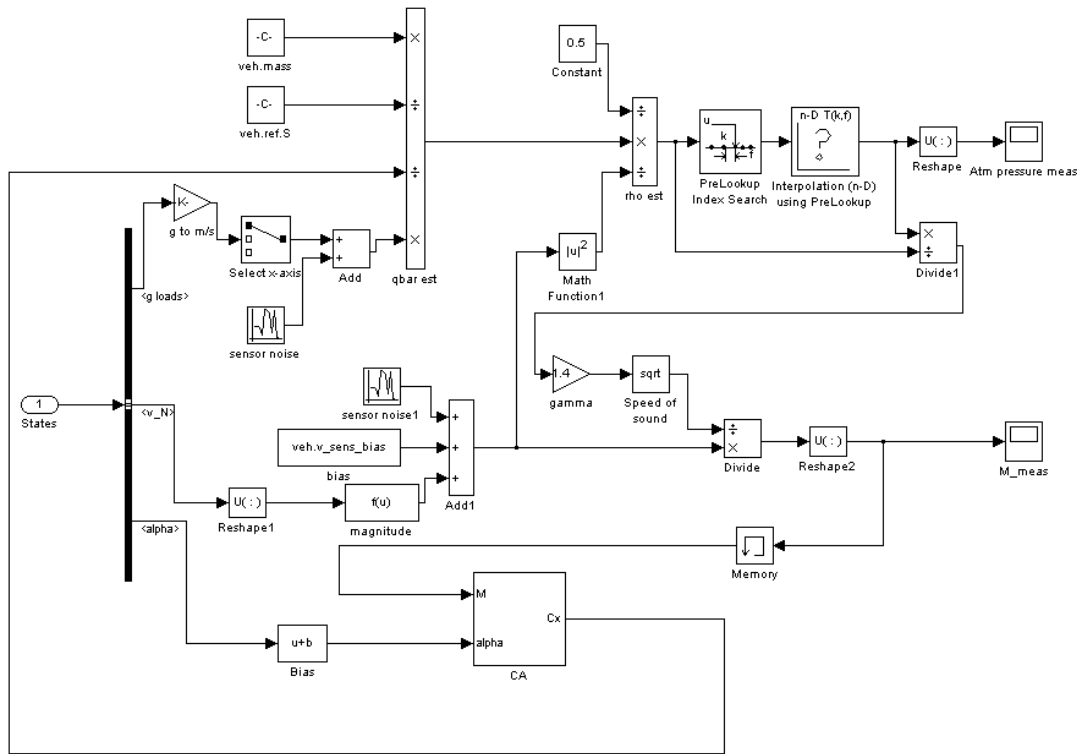


Figure 37. Simulink drag derived Mach estimation scheme.

3.3.3 Constant temperature Mach estimation

If the drogue deployment is between 11 and 30 km altitude, a more simple Mach estimation method can be used. Since the temperature is very stable in the stratosphere and has a square root relation with the speed of sound, the speed of sound can be assumed constant (see Figure 8 for the atmosphere temperature

profile). In this case, drag derived measurements are not required and only the velocity has to be known, which can be divided by a constant speed of sound to estimate the Mach number. Furthermore, the parachute deployment has to be performed at only one instant on which the temperature can be optimized to achieve similar performance as the drag derived measurements. The Mach number will be calculated with:

$$M = \frac{V}{\sqrt{\gamma \cdot R \cdot T}} \quad (2)$$

The velocity and temperature dispersions are put inside a table to calculate the worst case scenarios for different IMU performance. T_{\min} and T_{\max} are plus or min 13 Kelvin 3σ .

If the IMU drifts are considered to be 3σ values these worst case values are:

$$(1 - (1-0.997)^2) \times 100 = 99.9991 \% \approx 4.5\sigma$$

| | | | | | | | | | |
|---------------------------------|------|------|------|------|------|------|------|------|------|
| Velocity est [m/s] | 432 | 442 | 452 | 462 | 472 | 482 | 492 | 502 | 512 |
| Velocity drift [m/s] | -40 | -30 | -20 | -10 | 0 | 10 | 20 | 30 | 40 |
| M_est, T_{nominal} [-] | 1.46 | 1.50 | 1.53 | 1.57 | 1.60 | 1.63 | 1.67 | 1.70 | 1.74 |
| M_est, T_{max} [-] | 1.42 | 1.45 | 1.49 | 1.52 | 1.55 | 1.59 | 1.62 | 1.65 | 1.69 |
| M_est, T_{min} [-] | 1.51 | 1.55 | 1.58 | 1.61 | 1.65 | 1.68 | 1.72 | 1.75 | 1.79 |

Table 15. *Worst case Mach estimations for the velocity estimation drift and temperature deviations.*

Using Monte Carlo simulations this leads to a 3σ result of Mach 0.0678 for a velocity bias of 20 m/s. More knowledge on temperature variations within the stratosphere is required to confirm the accuracy of this method.

3.3.4 Altitude estimation

With the estimation of the air density and using the standard US76 atmospheric model, an estimation can be made for the altitude. The accuracy of this estimation mainly depends on the aerodynamic uncertainty and the atmospheric variations. Already at modeling level of the nominal trajectory, there is an error in the altitude estimation:

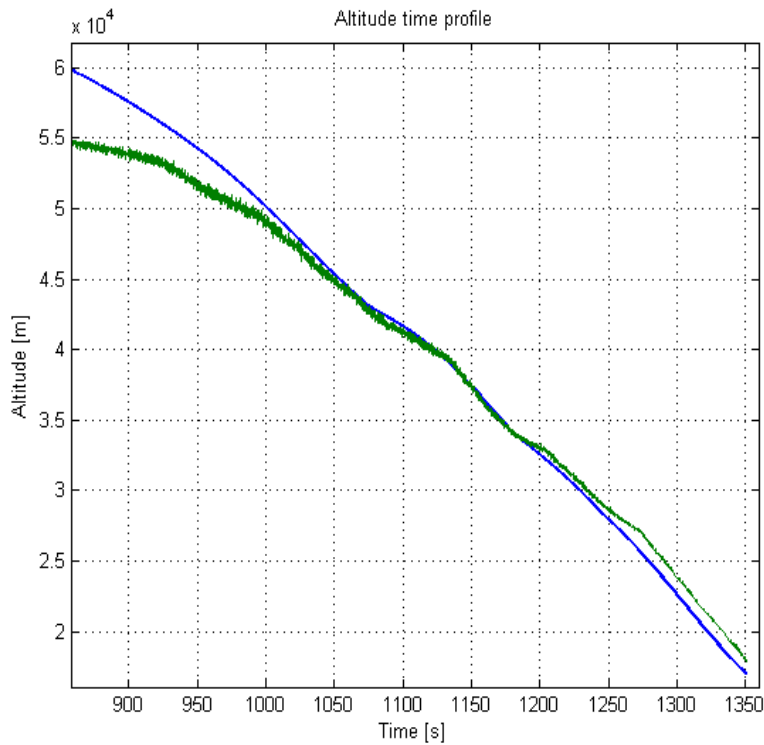


Figure 38. Altitude estimation by DDA. The blue line is the as-flown trajectory; the green line indicates the measured altitude.

The main contribution of the error in the altitude estimation and in the drag derived measurements in the simulation is de discrepancy of the C_A simulated value and the simulated measured value, already without taking into account any aerodynamic uncertainties. Agreement on the definition of the C_A might solve this problem. The C_A propagation as currently simulated seems unlikely because it contains discontinuities. These discontinuities might originate from the Matlab interpolation of the lookup table of the C_A , which is a function the Mach number and the angle off attack. Since the curve of the Mach number is smooth, the possible cause is the interpolation or the definition of the C_A as a function of the angle off attack.

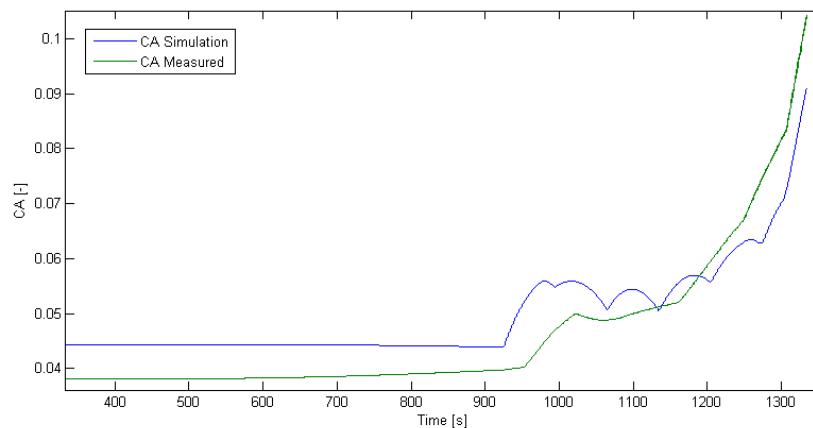


Figure 39. C_A modeling discrepancy between the simulated C_A and the simulated measured C_A .

If a drag derived method is planned to be used on a future mission, it is recommended to verify a smooth continuation of the C_A in FMST in order to perform a reliable analysis.

3.4 Main error sources

The IMU provides the velocity by integration the measured acceleration. Since the Mach number is equal to the velocity divided by the speed of sound, the error of the measurement will increase linearly with the velocity measurement error. The IMU velocity drift is independent of the velocity itself, so the error ratio will increase exponentially with decreasing velocity, see Figure 40.

An important contribution of the measurement accuracy is the stability of the stratosphere, the atmospheric layer in which the vehicle will be flying during deployment conditions. The speed of sound has a square root relation with the only dependence being the temperature. In the stratosphere the temperature varies only ± 13 K 3σ which will lead to an error no more than Mach 0.05 at deployment conditions, or as shown in Figure 40, a temperature of -13 K below the nominal temperature will lead to a constant error ratio estimate of 1.03.

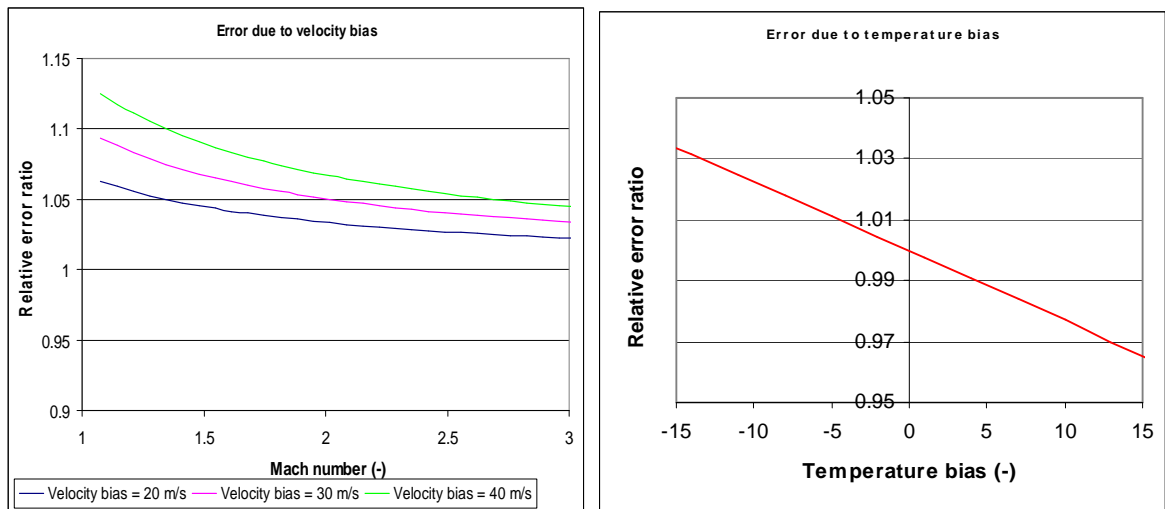


Figure 40. Relative error ratios of the Mach number as a function of the velocity drift (left) and the temperature uncertainty.

3.4.1 IMU sensitivity

The drag derived measurements are based on the outputs of the IMU; the deceleration and the velocity. The accuracy of these outputs depends on the characteristics of the IMU used. An IMU can have the following measurement inaccuracies:

- Velocity noise
- G-load noise and bias
- Aoa noise and bias
- Velocity bias

It has been investigated what kind of influence these inaccuracies have on the total measurement inaccuracy using 11 Monte Carlo simulations of 500 runs. The results are presented in Table 16. The upper part of the table shows which kind of measurement error is activated, the lower part shows the results defining the parachute deployment window.

| | Case 1 | Case 2 | Case 3 | Case 4 | Case 5 | Case 6 | Case 7 | Case 8 | Case 9 | Case 10 | Case 11 |
|--|--------|--------|--------|--------|--------|--------|--------|--------|--------|---------|---------|
| Velocity estimate bias [m/s] | 0 | 0 | 0 | 0 | 0 | 0 | 0 | 10 | 20 | 30 | 40 |
| AoA estimate bias [deg] | 0 | 0 | 0 | 0 | 0 | 2 | 4 | 0 | 0 | 0 | 0 |
| G-force measurement noise [g] | 0 | 0 | 0 | 0.05 | 0.1 | 0 | 0 | 0 | 0 | 0 | 0 |
| Velocity measurement noise [m/s] | 0 | 5 | 10 | 0 | 0 | 0 | 0 | 0 | 0 | 0 | 0 |
| Drag derived measurements | | | | | | | | | | | |
| 3σ at M = 1.4 [Mach] | 0.0013 | 0.0037 | 0.0055 | 0.0013 | 0.0013 | 0.0013 | 0.0013 | 0.0112 | 0.0221 | 0.0326 | 0.0454 |
| 3σ at M = 1.6 [Mach] | 0.0015 | 0.0041 | 0.0071 | 0.0015 | 0.0015 | 0.0015 | 0.0016 | 0.0111 | 0.0219 | 0.0321 | 0.0448 |
| 3σ at M = 1.7 [Mach] | 0.0016 | 0.0040 | 0.0062 | 0.0017 | 0.0017 | 0.0016 | 0.0018 | 0.0111 | 0.0218 | 0.0321 | 0.0462 |
| Constant temperature mach estimation | | | | | | | | | | | |
| 3σ at M = 1.4 [Mach] | 0.0017 | 0.0039 | 0.0060 | 0.0016 | 0.0017 | 0.0015 | 0.0016 | 0.0113 | 0.0221 | 0.0324 | 0.0452 |
| 3σ at M = 1.6 [Mach] | 0.0016 | 0.0041 | 0.0065 | 0.0016 | 0.0016 | 0.0017 | 0.0017 | 0.0114 | 0.0220 | 0.0324 | 0.0451 |
| 3σ at M = 1.7 [Mach] | 0.0021 | 0.0040 | 0.0067 | 0.0020 | 0.0020 | 0.0021 | 0.0021 | 0.0116 | 0.0221 | 0.0326 | 0.0452 |
| Density estimation related measurements | | | | | | | | | | | |
| Mean dynamic pressure error [Pa] | 1098 | 1105 | 1106 | 1113 | 1127 | 1098 | 1077 | 1101 | 1106 | 1105 | 1097 |
| 3σ dynamic pressure error [Pa] | 316 | 313 | 296 | 328 | 362 | 351 | 471 | 338 | 354 | 431 | 525 |
| Mean altitude error [m] | -1465 | -1394 | -1333 | -1481 | -1518 | -1459 | -1438 | -1491 | -1451 | -1463 | -1466 |
| 3σ altitude error [m] | 1121 | 1150 | 1093 | 1162 | 1147 | 1092 | 1234 | 1145 | 1172 | 1222 | 1337 |

Table 16. Sensitivity results of different measurement errors of the deployment conditions.

Case 1 is a reference case using a perfect IMU with no sensor noise and bias.. Errors induced in these measurements are because of aerodynamic, atmospheric uncertainties and the C_A discrepancy described in subparagraph 3.3.4. The Error due to the aerodynamic uncertainty of the axial drag coefficient is small since a large estimation error of 20% of the density will induce an altitude error of less than 1.5 km because the density is exponential. This induces only a 1 K error on the atmospheric temperature if deployment is in or above the tropopause. Case 2 and 3 show the influence of velocity noise, but it is expected an IMU will not produce much velocity noise because it is an integrated value. Furthermore the influence is small. Case 4 and 5 show the influence of g-load noise. In the simulation also this noise has barely an effect on the measurements, because the deceleration is used to estimate the relatively stable conditions of the stratosphere. It is also used to estimate the dynamic pressure and it can be seen the error slightly increases, although the main error is due to the C_A error. Case 6 and 7 are the angle of attack bias errors; the angle of attack measurement is required to estimate the C_A and this error exposes itself through this value. This bias has increased influence when the angle of attack is low, at the end phase of the re-entry.

Case 8 to 11 show the velocity drift, on which the Mach dispersion is depicted in Figure 41. This velocity drift is determining the quality of the measurement: The dispersions are an order of magnitude higher than the errors induced by the other cases.

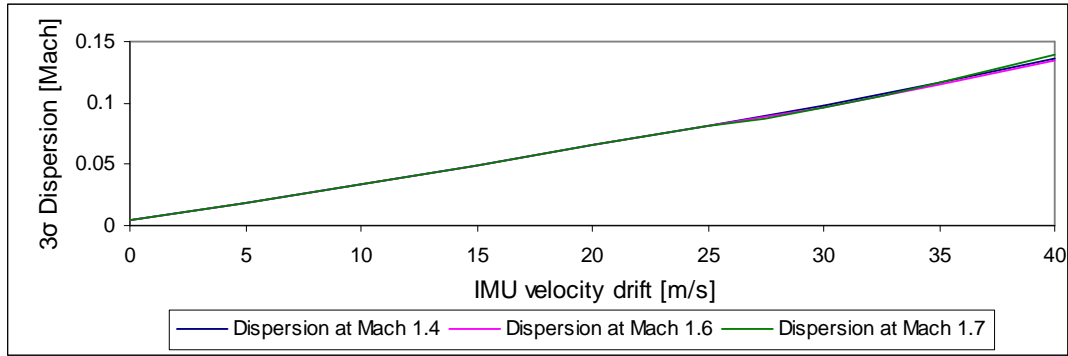


Figure 41. Mach dispersion as a function of the velocity drift.

3.4.2 Calculation of the error due to wind

The inertial measurement unit provides the velocity with respect to an earth fixed reference frame and does not provide any information about the airspeed directly. To investigate what happens to the Mach estimation if there is any wind a calculation example is performed at the deployment conditions:

| | | |
|-----------------|-------------|-------------------|
| Real stat press | 2925,04 | Pa |
| Real density | 0,04699778 | kg/m ³ |
| Static temp | 220,56 | K |
| a | 297,7187384 | m/s |
| M | 1,6 | - |
| V | 476,3499815 | m/s |

Table 17. Real conditions for deployment at Mach 1.6.

The velocity V is the velocity measured by the IMU. A 15 m/s head wind is introduced. This leads to a difference in the drag measured using the accelerometers

| | | | | |
|---------------------|-------------|---|-----------|-----|
| Drag | 44576,4964 | N | -1,71257 | m/s |
| Drag with head wind | 47428,07672 | N | -1,822124 | m/s |

Table 18. Drag measured with and without wind.

However, the measured velocity of the IMU is the same in both cases. ρ is calculated through the dynamic pressure and because the IMU velocity is 15 m/s lower, ρ will be higher:

| | | |
|------------------------|-------------|-------------------|
| ρ meas | 0,050004251 | Kg/m ³ |
| Static pressure lookup | 3161 | Pa |
| a meas | 297,4902951 | m/s |
| M meas | 1,601228643 | - |

Table 19. Measured Mach number with wind.

The result of the calculation leads to a Mach number of still 1.6 but it calculated to be flying at a lower altitude than the actual flying altitude, while in reality the Mach

number becomes 1.65 due to the wind. To conclude; wind adds to the velocity measured bias. If an accurate altitude measurement would be available, this bias could be corrected.

3.4.3 Alternative estimation of the velocity

It is determined that estimation of the velocity is most important parameter for the estimation of the parachute deployment conditions. It is worth investigating whether this estimation can be performed in an alternative way if the IMU integrated value is not available. This can be done using similar drag derived measurements, but with another parameter instead of the velocity. In this case a static pressure sensor will be used. A static pressure sensor has been available on already flown re-entry vehicles and is a potential redundant measurement device.

Using the drag derived measurements, the dynamic pressure is determined. With the dynamic pressure known, instead of the determination of the density, the velocity is determined. The ambient density is determined from the static pressure measurement:

$$P_{dyn} = \frac{1}{2} \cdot \rho \cdot V^2 \quad (3)$$

$$P_{stat} \xrightarrow{\text{Std atm}} \rho \rightarrow V = \sqrt{\frac{2 \cdot P_{dyn}}{\rho}} \quad (4)$$

This measurement method is tested in a Monte-Carlo simulation to estimate its performance. The results are shown in Figure 42 and Table 20. Figure 42 shows the estimation method converges as soon as the g-loads in axial direction are high enough to overcome the noise. Furthermore it can be seen the estimation error is again depended largely on the determination method of the C_A .

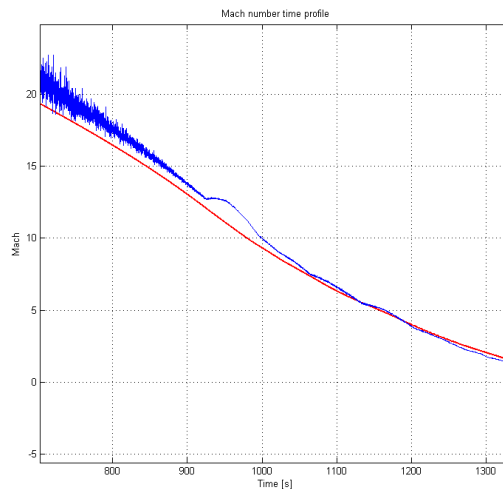


Figure 42. Velocity estimation using a drag derived measurement and a static pressure probe.

Table 20 shows the velocity error around the deployment conditions. The average velocity error of 107.51 m/s is a bias which originates from the C_A discrepancy described in subparagraph 3.3.4 and can be compensated for. The velocity dispersion of 74 m/s 3σ is expected to be 3 to 2 times higher than the IMU integrated velocity estimation, but is might be suitable for a redundant estimation or to perform on flight bias correction when this estimation is integrated. However, detailed knowledge of the flow field around the vehicle is necessary in order to obtain a precise static pressure measurement.

| | |
|------------------------------|---------|
| 3σ Velocity [m/s] | 73.97 |
| Average error velocity [m/s] | -107.51 |
| 3σ Mach [-] | 0.24 |

Table 20. Estimation error of the velocity using a drag derived measurement and a static pressure probe.

3.5 Nominal trajectory Mach estimation results

Figure 43 shows the convergence of the estimated Mach number starting from Mach 12, of the methods described above using a 15 m/s velocity drift and 5 m/s sensor noise. Before this point the deceleration has the same order of magnitude as the accelerations sensor's noise and therefore the measurement of the drag derived method is unusable. When the real deceleration becomes the dominant term over the noise, the estimation starts to converge. It can be seen in the picture both methods converge and are the most accurate at the end of the trajectory, which is desired for parachute triggering. Below Mach 1 the velocity bias will become the dominant error in the estimation, at this time the parachute should already have been deployed.

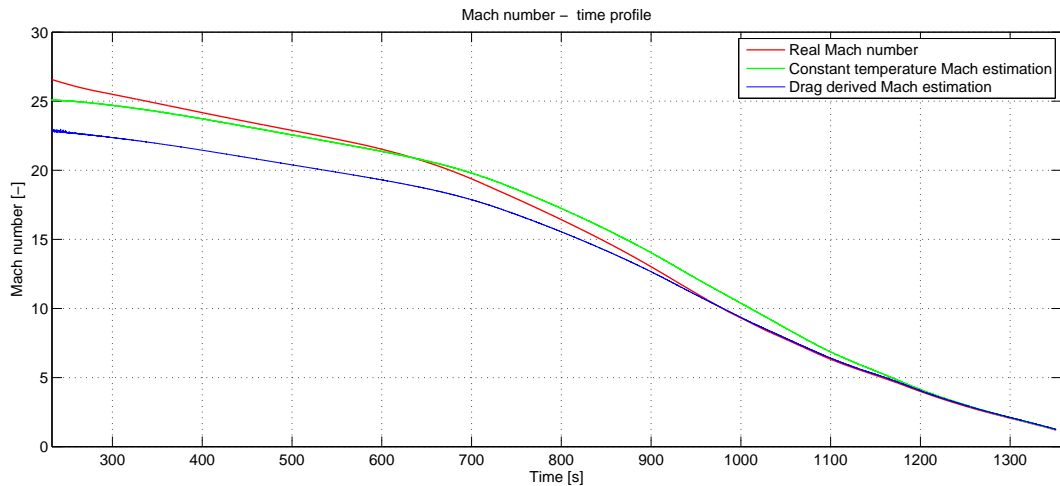


Figure 43. Lifting re-entry Mach profile with Mach estimation methods. Both Mach estimation profiles will converge to an acceptable error below Mach 5, which is more than sufficient for parachute deployment.

3.5.1 Monte Carlo results

Ten Mach estimations are depicted in Figure 44 in the lower part, for comparison the ‘as flown’ is depicted in the upper part of Figure 44 to visualize what is happening and how it is measured. The Mach dispersion of the drag derived method is depicted in Figure 44 on the right side.

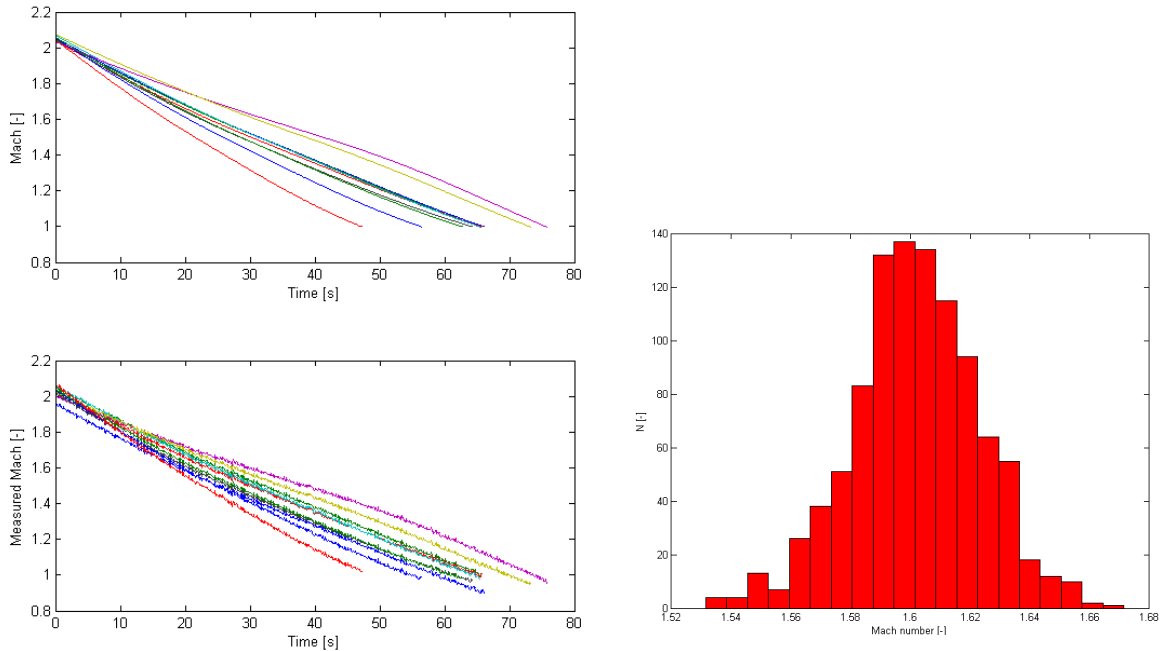


Figure 44. 10 Monte Carlo trajectories (upper left) and their measured values (lower left) The Mach estimation dispersion at Mach 1.6 is short in the histogram (right).

With an IMU accurate within 28 m/s 3σ , the accuracy becomes:

| | Drag derived | Constant temperature |
|---------------------------|--------------|----------------------|
| Mach 3σ at M = 1.4 | 0.0954 | 0.0948 |
| Mach mean at M = 1.4 | 1.3997 | 1.4039 |
| Mach 3σ at M = 1.6 | 0.0945 | 0.0951 |
| Mach mean at M = 1.6 | 1.6009 | 1.6022 |

Table 21. Mach dispersions of the two different estimation methods.

3.6 Off-nominal

Besides possible of nominal de-orbiting, failure of the onboard control systems are a risk for the mission success. For the lifting re-entry three off-nominal situations are investigated:

- Loss of IMU. In this case the drag derived measurements are not possible to perform and a different method has to be used, for instance, static pressure measurements.
- Loss of control but not navigation. In this case the vehicle will have more random flight paths, but the system will be able to measure the flight conditions.

- Ballistic re-entry. If systems of the vehicle fail at the beginning of the re-entry it might be possible to make a ballistic re-entry by giving the vehicle a constant spin, which makes the vehicle to rotate around the velocity axis in direction of velocity to rotate the lift vector and effectively cancel it out. The vehicle will go down in a spiraling motion.

3.6.1 In case of total loss of the IMU

The drag derived measurements totally rely on the IMU, just as the GNC systems. It might be the case the IMU fails, so there must be redundant systems to still deploy a parachute. If the IMU fails at the last part of the mission, a time based open loop control could be used. Also the velocity and the mach estimation can be 'open loop'. In this case, a constant descent rate is assumed, using the last known value the atmospheric density is estimated by integrating the constant descent rate. The velocity is estimated by calculating and integrating the deceleration from the last measured velocity. The open loop estimation is performed using a constant altitude rate:

$$\frac{d\rho}{\rho} = \frac{-dH}{H} = \text{Constant} \quad (5)$$

The initial ρ is the last known measurement from the IMU. To estimate the deceleration, the equation of the dynamic pressure is used:

$$P_{dyn} \approx \frac{m \cdot a}{S_{ref} \cdot C_D} = \frac{1}{2} \cdot \rho \cdot V^2 \quad (6)$$

This can be rewritten as:

$$\frac{S_{ref} \cdot C_D \cdot \frac{1}{2} \cdot \rho \cdot V^2}{m} = a = \frac{dV}{dT} \quad (7)$$

The air density and the deceleration are integrated over time to estimate the velocity. In order to investigate until which point this open loop estimation is accurate, it is inserted into FMST and at 10 seconds intervals, estimations are made on what point Mach 1.5 is reached, which is a realistic parachute deployment value.

| Time before deployment [s] | Mach number at IMU failure [Mach] | Velocity error at M=1.5 [m/s] | Air density error at M = 1.5 [kg/m ³] | Estimated Mach at M=1.5 [Mach] |
|----------------------------|-----------------------------------|-------------------------------|---|--------------------------------|
| 234 | 6,33 | -78,35 | 0,018598 | 1,23 |
| 224 | 6,07 | -46,22 | 0,010859 | 1,34 |
| 214 | 5,83 | -21,72 | 0,00509 | 1,42 |
| 204 | 5,6 | -6,12 | 0,001219 | 1,47 |
| 194 | 5,38 | 1,32 | -0,0009 | 1,5 |

| Time before deployment [s] | Mach number at IMU failure [Mach] | Velocity error at M=1.5 [m/s] | Air density error at M = 1.5 [kg/m ³] | Estimated Mach at M=1.5 [Mach] |
|----------------------------|-----------------------------------|-------------------------------|---|--------------------------------|
| 184 | 5,16 | 1,79 | -0,00151 | 1,5 |
| 174 | 4,94 | -3,38 | -0,00087 | 1,48 |
| 164 | 4,71 | -12,54 | 0,000618 | 1,45 |
| 154 | 4,48 | -21,75 | 0,002079 | 1,42 |
| 144 | 4,23 | -12,44 | -0,00113 | 1,45 |
| 134 | 4 | -2,55 | -0,0046 | 1,48 |
| 124 | 3,77 | 5,69 | -0,00773 | 1,51 |
| 114 | 3,55 | 11,38 | -0,01028 | 1,53 |
| 104 | 3,34 | 12,89 | -0,01172 | 1,54 |
| 94 | 3,13 | 10,33 | -0,01195 | 1,53 |
| 84 | 2,94 | 9,35 | -0,01274 | 1,52 |
| 74 | 2,75 | 9,96 | -0,01401 | 1,52 |
| 64 | 2,57 | 8,28 | -0,01396 | 1,52 |
| 54 | 2,39 | 5,28 | -0,01277 | 1,51 |
| 44 | 2,23 | 1,03 | -0,01067 | 1,5 |
| 34 | 2,06 | -3,44 | -0,00785 | 1,48 |
| 24 | 1,9 | -6,87 | -0,0045 | 1,47 |
| 14 | 1,73 | -8,33 | -0,00118 | 1,47 |
| 4 | 1,57 | -6,9 | 0,001079 | 1,47 |

Table 22. Mach estimation errors of open loop estimation. From Mach 6 on, there is sufficient accuracy for successful deployment.

From Table 22 can be concluded that the open loop estimation converges to useful values around mach 6, 4 minutes before the actual deployment time. From parachute triggering point of view, a maximum of 4 minutes of flying time without feedback should be achievable.

3.6.2 Static pressure triggering

As last resort, the parachute can be triggered on static pressure only. Such a scenario would occur if the IMU fails in an early stage of the re-entry. In such a case the mission is considered to be unsuccessful and parachute deployment is desired just in order to have a chance of retrieving most parts of the vehicle. This procedure has a high risk of failure, because contains has no information on the important parameters of parachute triggering and the vehicle is basically gliding uncontrolled through the sky. A Monte Carlo analysis is performed to trigger on a specific static pressure, representing the nominal desired deployment altitude. The results are presented in Figure 45, but it gives a too optimistic picture, because in this simulation the vehicle is in controlled flight. The deployment peak at Mach 2.1 is due to a limitation of the Monte Carlo simulation, which starts at around Mach 2.1; all values in this peak represent a Mach number of 2.1 and higher where the parachute should have already be deployed according to the static pressure measurement.

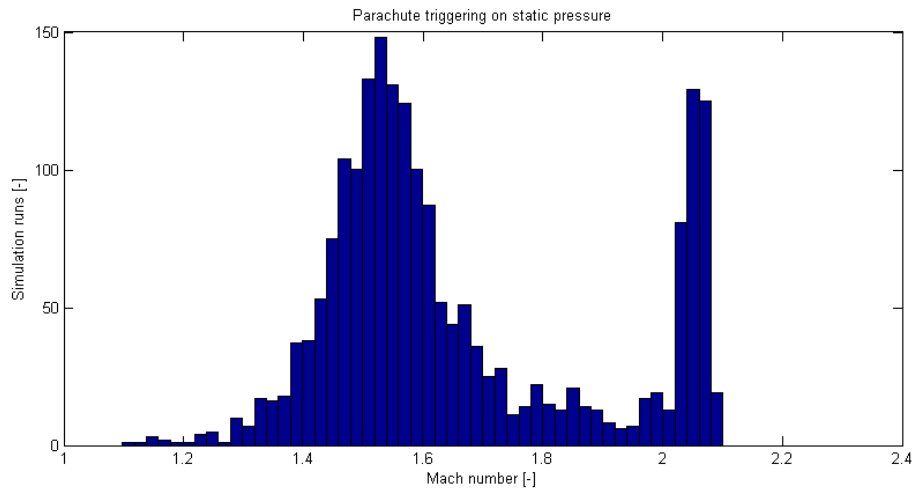


Figure 45. Histogram of the Mach dispersion when static pressure triggering is used.

If the vehicle is still flying, parachute deployment on static pressure only will be in the range of Mach 1.1 to 2.4.

3.6.3 Ballistic re-entry

It might be the case the vehicle cannot be controlled as designed, or the de-orbiting goes wrong. In both cases, it might be decided to perform a ballistic re-entry. This is achieved by giving the vehicle a constant bank angle rate, to constantly rotate the lift vector about the velocity axis in order to cancel it out. This is only possible when the vehicle can obtain a sufficient bank angle rate. If the vehicle is still in working order, the Mach number and the velocity should still be measured as in the nominal flight. To test this case, the test vehicle is given a constant 10 deg bank rate to achieve a ballistic re-entry. The result of the Mach number and the measurement are presented in Figure 46. If also the IMU fails in this early stage, it might be considered to have a static pressure correlated algorithm for a ballistic re-entry as described in the chapter about ballistic re-entry vehicles.

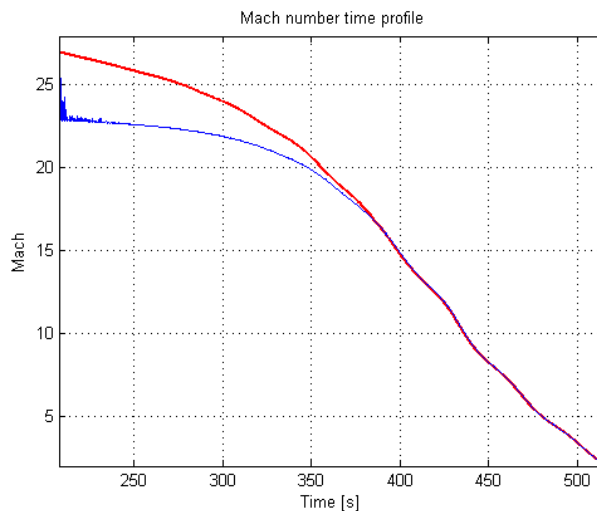


Figure 46. Drag derived Mach estimation of a ballistic re-entry for a lifting re-entry vehicle.

3.7 Parachute triggering logic

With the measurement methods identified and the off-nominal conditions discussed a parachute triggering logic can be developed. It is based on which measurements are available in which condition.

Figure 47 presents a schematic overview of the mach estimation process on system level. Since the parachute trigger system has to be reliable, redundant inputs are required. So the three main inputs, velocity acceleration and AoA are redundantly estimated. The flight computer should have a C_A , an atmospheric and an AoA database onboard. Selection on the preferred Mach estimation should be based on the accuracy of the method used.

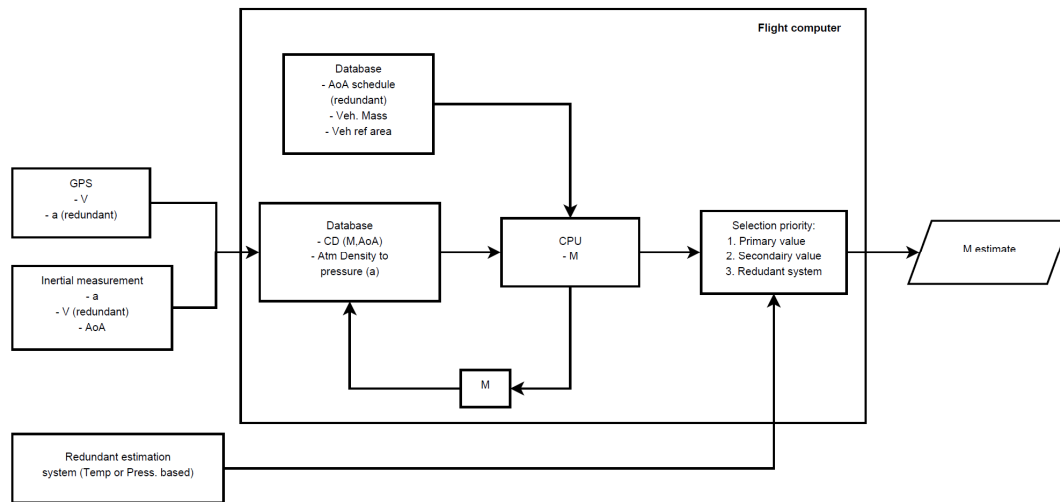


Figure 47. Mach estimation system indicating redundancy.

Figure 48 shows the parachute triggering system at logics level. This chain of decisions should be able to cope with all off-nominal situations described and using the most accurate solutions first. It uses the following measurements in order of preference:

1. Drag derived Mach number estimation
2. Mach estimation using the velocity and a constant temperature
3. Velocity and Mach estimation using drag derived measurements and static pressure
4. Open loop velocity estimation
5. Static pressure trigger

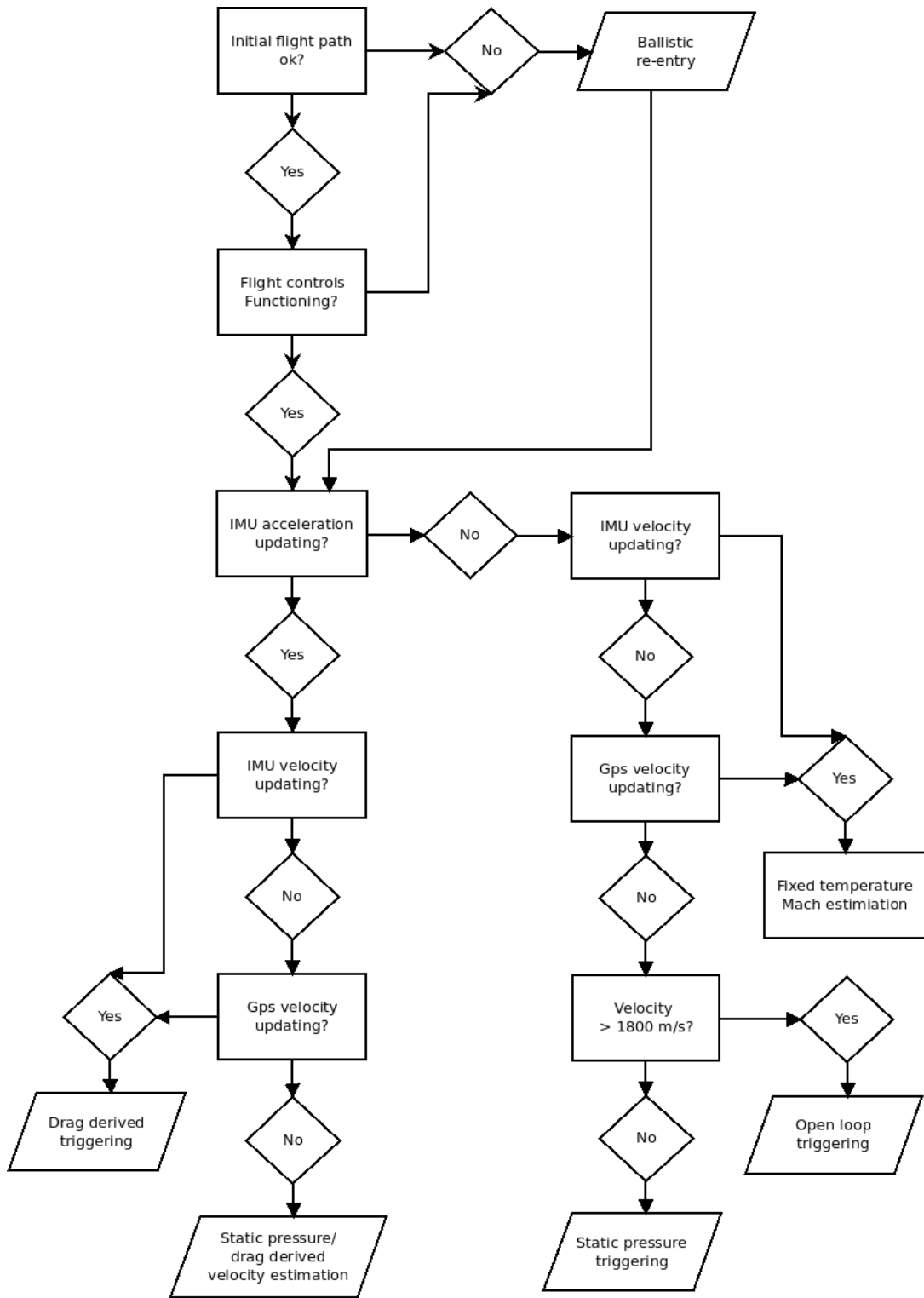


Figure 48. Parachute triggering system at logics level.

3.8 Conclusions

Accurate velocity estimation is the main driver for parachute deployment, because this value has the most influence on both the Mach number estimation as the dynamic pressure estimation. The 3σ success rate will depend on the accuracy of the velocity estimation of the IMU. For this reason and because the stratosphere is very stable, drag derived measurements are not strictly necessary if the average temperature of the stratosphere is measured just before the mission. If FMST is to be used to analyze a drag derived method for a future mission, a solid definition of the C_A should be made and implemented.

The highest risk to the triggering success rate is wind, because this investigation did not succeed to estimate this parameter accurately. The best chance to estimate this value is determined to be a drag derived method together with a static pressure measurement. However with the C_A discrepancy found in FMST accurate estimation was not possible. But if this issue assumed to be resolved and just neglected as a bias, still a high dispersion of 73.97 m/s 3σ was achieved and therefore a successful implementation of such a system remains questionable.

Open loop estimation as defined in subparagraph 3.6.1 can secure the mission in case the IMU fails at the end of the mission. Unfortunately, at the most extreme part of the re-entry, no easy achievable back-up exists in the IMU failure case. If there is a failure at this most extreme part static pressure measurements can be used only as a last resort. It is undesirable, because the altitude information does not have correlation with the flown flight path. Ballistic re-entry can save the vehicle when there are problems in an early stage of the re-entry, however the vehicle must be capable of performing such a re-entry. Because the velocity estimate is found to be the driving parameter and the opportunity to have an accurate estimate of deployment conditions only for this measurement it is recommended from reliability point of view to fly with a redundant IMU which would at least be able to estimate this velocity. Alternatively GPS should be considered to remain as back-up to provide a two fault tolerant system. From these developed and analyzed methods a logics flow diagram was developed to determine the optimum method at each situation during flight.

4 Footprint reduction

If the flight conditions can be estimated accurately, the parachute opening window size might be used to open the parachute prior or post the nominal conditions in order to reduce the footprint of the re-entry vehicle's landing site. This way the longitudinal axis of the ellipse can be decreased. Furthermore it will be investigated whether a slightly more robust parachute can make a significant reduction of the landing site footprint in order to have a semi-controlled re-entry. Such a controlled deployment might be an intermediate step from the uncontrolled ballistic flight and lift-vector control used for a completely guided re-entry.

4.1.1 Applicability for footprint reduction study

The investigation for footprint reduction by a dynamic parachute opening window aims to investigate the opportunities and limitations of such a method. It could be used for:

- Precision landings for small footprints
- A simple reduction of large footprints

A precision landing would be possible if the footprint size is a similar size as the reduction possible by the dynamic parachute deployment. Unfortunately this is not the case, the footprint size of the re-entry missions investigated are at least more than twice the possible reduction size by a parachute in ideal circumstances. For this reason, a simple reduction method is investigated to reduce footprints in the order of tens of kilometers, while this will also give an insight what would be a feasible footprint size for precision landings.

4.1.2 Footprint reduction deployment control

From early analysis it is determined that even with a very robust drogue of a currently used size, the footprint can never be reduced to a theoretical zero, because the amount of kilometers reduction achievable by an adaptable drogue deployment time will never be at the same size of current re-entry footprints. For this reason, the deployment algorithm does not have to make a very fine estimation of the right moment of deployment: Defining three discrete instants of deployment is already sufficient to have a theoretical reduction of 66.7 % compared to a single point deployment on nominal conditions. So, the algorithm will be developed to define just 3 'settings': 1) 'flight path undershoot', 2) 'on nominal course', and 3) 'flight path overshoot'. The control algorithm will deploy at a defined high Mach number when the vehicle's flight path to overshoot its landing site and will deploy at a lower bound mach number when the vehicle is defined to undershoot its nominal landing site. Since it will be unlikely 66.7% reduction will ever be achieved with any drogue, 3 discrete control steps odd to be sufficient. This will keep the algorithm simple and more importantly, makes it possible to make a very course, and thus an easy to estimate, downrange prediction.

For the footprint analysis again the Mach range is determined to be the driving parameter.

4.1.3 Modeling of the parachute in FMST

To perform the footprint analysis, the parachute phase should also be modeled, because a downrange prediction has to be made at any given point of the opening of the parachute. Since there was no FMST model provided for the parachute phase modeling, the total trajectory will be cut in two phases: The phase prior to the parachute deployment and the phase on which the parachute is deployed. The deployment itself is simplified to be instantaneous. The parachute phase is modeled by changing the reference area of the vehicle. This reference area will be the reference area of the vehicle + the parachute area, multiplied by a correction factor of an estimated parachute drag coefficient divided by an average vehicle's drag coefficient:

$$D_{tot} = C_{D_{Vehicle}} \cdot S_{ref\ Vehicle} \cdot \frac{1}{2} \cdot \rho \cdot V^2 + C_{D_{Parachute}} \cdot S_{ref\ Parachute} \cdot \frac{1}{2} \cdot \rho \cdot V^2 \quad (8)$$

$$D_{tot} \approx \frac{1}{2} \cdot \rho \cdot V^2 \cdot C_{D_{Vehicle}} \cdot \left(S_{ref\ Vehicle} + S_{ref\ Parachute} \cdot \frac{C_{D_{Parachute}}}{\bar{C}_{D_{Vehicle}}} \right) \quad (9)$$

This method is used to have an easy implantation of the parachute into FMST. Since the drag coefficient of the vehicle changes with respect to the Mach number, the parachute drag coefficient will change with it. The total modeling of the parachute behaviour is not necessarily fully representative this way, but for downrange prediction this is assumed to be sufficient, because the downrange travel after the parachute deployment is small compared to the total footprint: about 3 km for lower bound Mach number deployment, to about 10 km to high Mach number deployment. The vehicle's aerodynamic database has a decreasing C_D with a decreasing Mach number. Since the parachute's modeling is linked to the vehicle's aerodynamic database, the parachute efficiency decreases with it, which is corresponding to reference¹⁴. But even if the prediction has a relatively high error of the parachute downrange, the error will still be relatively small compared to the total footprint size. Furthermore, a possible second or 2nd stage deployment will not be taken into account, since during these phases the horizontal displacement is negligible (a few hundreds of meters) and not applicable for Mars missions, since only one stage has been used on Mars.

4.2 Earth ballistic re-entry footprint reduction

To investigate the footprint reduction capabilities, the earth ballistic reference case is used. With this preliminary investigation no Monte Carlo simulation is performed, only the parachute phase is modeled at different Mach numbers with their corresponding nominal flight conditions in order to determine the maximum amount of kilometers can be gained using minimum or maximum mach deployment criteria. Figure 49 shows the last part of the trajectory with parachute deployment at different Mach numbers.

The parachute characteristic is set to have a $S_{ref\ Parachute} \cdot \frac{C_{D_{Parachute}}}{\bar{C}_{D_{Vehicle}}}$ of 3, which can be interpreted as a parachute with a diameter of 2 m and a C_D of 0.678 to 0.55 in a

Mach range of 1.45 to 3, which are realistic values, based on drogue dimensioning of the Pares vehicle.

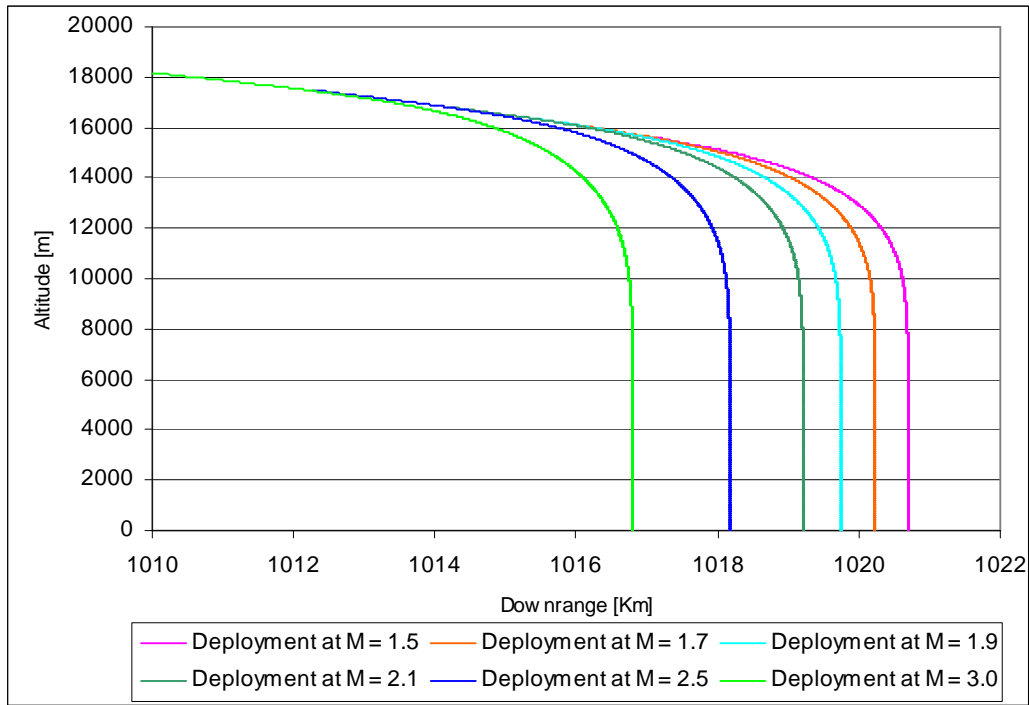


Figure 49. Terminal trajectories with parachute deployment at different Mach numbers.

The difference in distance covered between Mach 3 and 1.5 is around 4 km; which would be about the maximum footprint reduction possible with a very robust parachute, if a parachute would be used which has a mach range similar to EXPERT, the total reduction possible would be around 1.5 km. Figure 50 shows achievable footprint reduction as a function of the parachute opening Mach range. This maximum reduction possible is actually also a function of the flight path angle, velocity/deceleration and the size of the parachute. All of these parameters will show an increase in footprint reduction if the opening window is shifted to higher Mach numbers: The flight path angle will be more horizontal, the distance difference will be higher of the higher deceleration, distance covered will be higher due the higher velocity and the size of the parachute will also increase the deceleration. However, a parachute capable of deploying at higher Mach number than 2.5 is not yet available and even if the deployment window will have a range of Mach 4 (so for example from 6.5 to 1.5), reduction will just still be around 13.7 km. Such a decelerator has not been developed yet. For this reason such a system is only feasible for precision landing systems or when hypersonic deceleration systems would be developed.

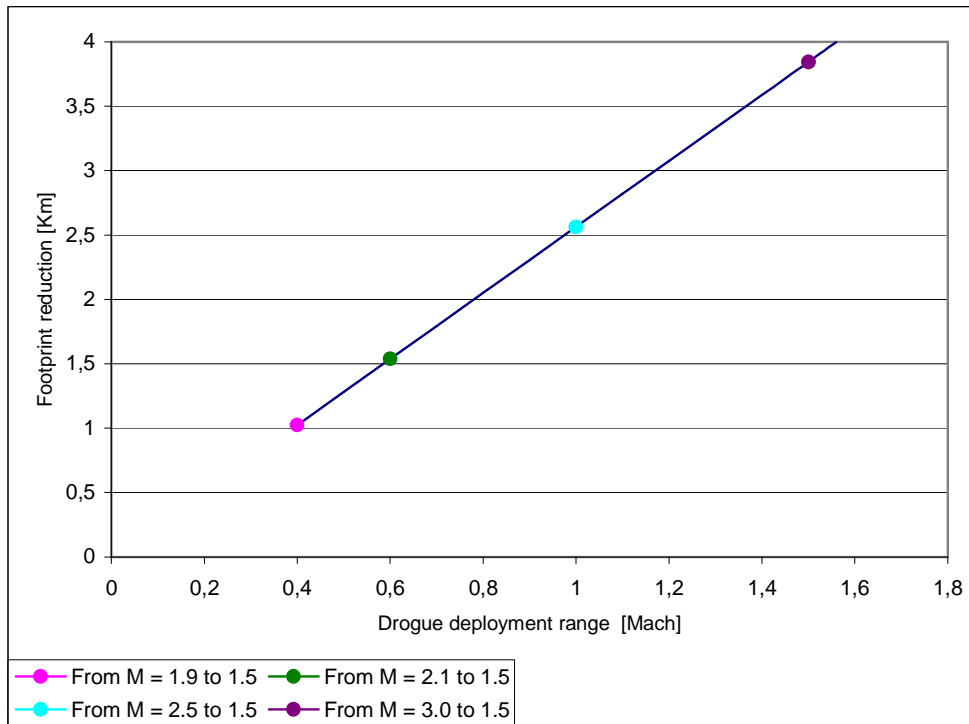


Figure 50. *Footprint reduction capability as a function of the parachute opening window.*

4.3 MER footprint reduction

From the analysis performed in paragraph 4.2, there seems to be an opportunity for adaptive parachute deployment for a Mars mission. Mars has a rare atmosphere and low gravity compared to Earth, these phenomena increase the distance flown in the supersonic regime. Footprints on Mars in general are bigger than on Earth because less is known about Martian atmosphere which has got a high variability, thus the modeling uncertainties atmosphere are also higher. Reduction of these footprints is desired in order to increase the probability of a landing on a flat area, which increases the probability of a mission success.

4.3.1 MER footprint reconstruction

In order to make a realistic footprint reduction analysis, first a realistic re-entry scenario has to be developed: Due to the availability of public data, the MER (Mars Exploration Rover) missions are selected to serve as a scenario test case. A system layout of the MER re-entry configuration is presented in figure Figure 51.

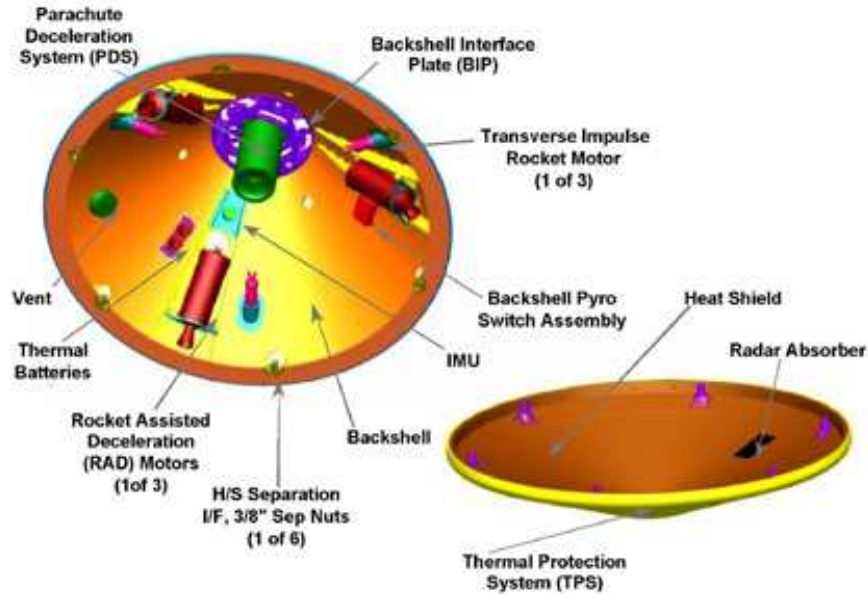


Figure 51. Exploded view of the MER re-entry vehicle²¹.

From all the public data available the aerodynamic database, insertion conditions, deployment conditions, landing position and their uncertainties are gathered. This data is inserted in the FMST to perform a Monte Carlo analysis in order to reproduce the footprint. The basic re-entry initial conditions are displayed below in Table 23.

| Nominal conditions ballistic re-entry | Lower limit | Upper limit | Distr. | Unit | Remark |
|---------------------------------------|--|-------------|--------|------------|---|
| Vehicle | MER | | | | |
| Mass MER A | 827 | -8.27 | 8.27 | 3 σ | kg |
| Mass MER B | 831 | -8.31 | 8.31 | 3 σ | kg |
| Inertia matrix | Unit matrix | | | | |
| Aerodynamic MER A and B | | | | | See Table 24 for drag coefficients |
| $\Delta CA < \text{Mach } 2$ | 0 | -5 | 5 | 3 σ | % This parameter defines only the dispersion, the aerodynamic value itself is calculated during the simulation |
| $\Delta CN < \text{Mach } 2$ | 0 | -5 | 5 | 3 σ | % This parameter defines only the dispersion, the aerodynamic value itself is calculated during the simulation |
| $\Delta Cm < \text{Mach } 2$ | 0 | -5 | 5 | 3 σ | % This parameter defines only the dispersion, the aerodynamic value itself is calculated during the simulation |
| $\Delta CA \geq \text{Mach } 2$ | 0 | -5 | 5 | 3 σ | % This parameter defines only the dispersion, the aerodynamic value itself is calculated during the simulation |
| $\Delta CN \geq \text{Mach } 2$ | 0 | -5 | 5 | 3 σ | % This parameter defines only the dispersion, the aerodynamic value itself is calculated during the simulation |
| $\Delta Cm \geq \text{Mach } 2$ | 0 | -5 | 5 | 3 σ | % This parameter defines only the dispersion, the aerodynamic value itself is calculated during the simulation |
| Scenario MER A | Inertial position in polar coordinates, attitude in inertial VEL | | | | |

| Nominal conditions ballistic re-entry | | Lower limit | Upper limit | Distr. | Unit | Remark |
|--|------------------------|-------------|-------------|------------|------------------|--|
| Altitude | 129200 | -5100 | 5100 | 3 σ | m | |
| Latitude | -17,7 | -0.12 | 0.12 | 3 σ | deg | |
| Longitude | 161,8 | 0.01 | 0.01 | 3 σ | deg | |
| Velocity | 5630 | -2.1 | 2.1 | 3 σ | m/s | |
| Heading | 79 | -0.06 | 0.06 | 3 σ | deg | |
| Flight path angle | -11.5 | -0.06 | 0.06 | 3 σ | deg | |
| Mission time | 330 | | | | s | |
| Scenario MER B Inertial position in polar coordinates, attitude in inertial VEL | | | | | | |
| Altitude | 129200 | -5100 | 5100 | 3 σ | m | |
| Latitude | -17,7 | -0.12 | 0.12 | 3 σ | deg | |
| Longitude | 161,8 | 0.01 | 0.01 | 3 σ | deg | |
| Velocity | 5630 | -2.1 | 2.1 | 3 σ | m/s | |
| Heading | 79 | -0.06 | 0.06 | 3 σ | deg | |
| Flight path angle | -11.5 | -0.06 | 0.06 | 3 σ | deg | |
| Mission time | 330 | | | | s | |
| Attitude MER A and B | | | | | | |
| alpha | 0 | | | | deg | Value not used in ballistic point mass re-entry simulation |
| beta | 0 | | | | deg | Value not used in ballistic point mass re-entry simulation |
| phi_aero | 0 | | | | deg | Value not used in ballistic point mass re-entry simulation |
| roll_dot | 0 | | | | deg | Value not used in ballistic point mass re-entry simulation |
| pitch_dot | 0 | | | | deg | Value not used in ballistic point mass re-entry simulation |
| yaw_dot | 0 | | | | deg | Value not used in ballistic point mass re-entry simulation |
| Environment | | | | | | |
| Atmosphere | See subparagraph 1.5.3 | | | | | |
| Parachute opening conditions | | | | | | |
| Altitude MER A | 7500 | -5100 | 5100 | 3 σ | m | |
| Altitude MER B | 6200 | -5400 | 5400 | 3 σ | m | |
| Mach number | 1.77 | | | | - | |
| Dynamic pressure MER A | 725 | | | | n/m ² | |
| Dynamic pressure MER B | 750 | | | | n/m ² | |
| Simulation properties | | | | | | A central gravity Mars model |
| Solver | ode 4 | | | | - | |

Table 23. Simulation initial conditions and uncertainties of the MER Monte Carlo simulation.

Compared to earth re-entry vehicles the Mars vehicles have a higher drag coefficient due to their shape, lower mass and bigger cross section area, this is necessary to keep the ballistic coefficient low, in order to be able to reduce the vehicle's speed sufficiently in the rare Mars atmosphere before it hits the planet's surface. The aerodynamic database is presented in Table 24.

| | | | | | | | | | | | |
|------|---------|---------|---------|---------|---------|---------|---------|---------|---------|---------|---------|
| Mach | 0,3811 | 0,6151 | 0,9303 | 1,0128 | 1,2509 | 1,5282 | 1,6067 | 2,0302 | 3,0306 | 4,1466 | 5,1087 |
| CA | 1,0445 | 1,0954 | 1,2133 | 1,2988 | 1,4145 | 1,5393 | 1,5647 | 1,5705 | 1,5775 | 1,5867 | 1,5960 |
| Mach | 6,3402 | 8,8415 | 9,8036 | 10,8425 | 11,8430 | 12,8817 | 13,9592 | 14,9983 | 16,0375 | 17,1153 | 18,1544 |
| CA | 1,6075 | 1,6272 | 1,6364 | 1,6434 | 1,6503 | 1,6549 | 1,6630 | 1,6734 | 1,6850 | 1,6988 | 1,7093 |
| Mach | 19,2320 | 20,2323 | 21,3479 | 22,4249 | 23,4249 | 24,4248 | 25,4247 | 26,3478 | 27,1939 | 28,0016 | 30,2702 |
| CA | 1,7185 | 1,7243 | 1,7278 | 1,7289 | 1,7278 | 1,7266 | 1,7254 | 1,7254 | 1,7254 | 1,7243 | 1,7150 |

Table 24. The aerodynamic database of the MER vehicle.

All the parameters defined lead to the re-entry profile presented in Figure 52. G-forces and dynamic pressure are respectively about 3 times and 100 times lower due to the lower gravity and dynamic pressure on Earth. Mars gravity and atmosphere are about 3 times and 100 lower as on earth. The re-entry starts at similar altitude, however the entry velocity has to be lower on Mars in order not to crash into the Martian surface if the flight path angle is steep, because of the thin atmosphere. Or to miss the planet if the flight path angle is too shallow, because of the lower Martian gravity field.

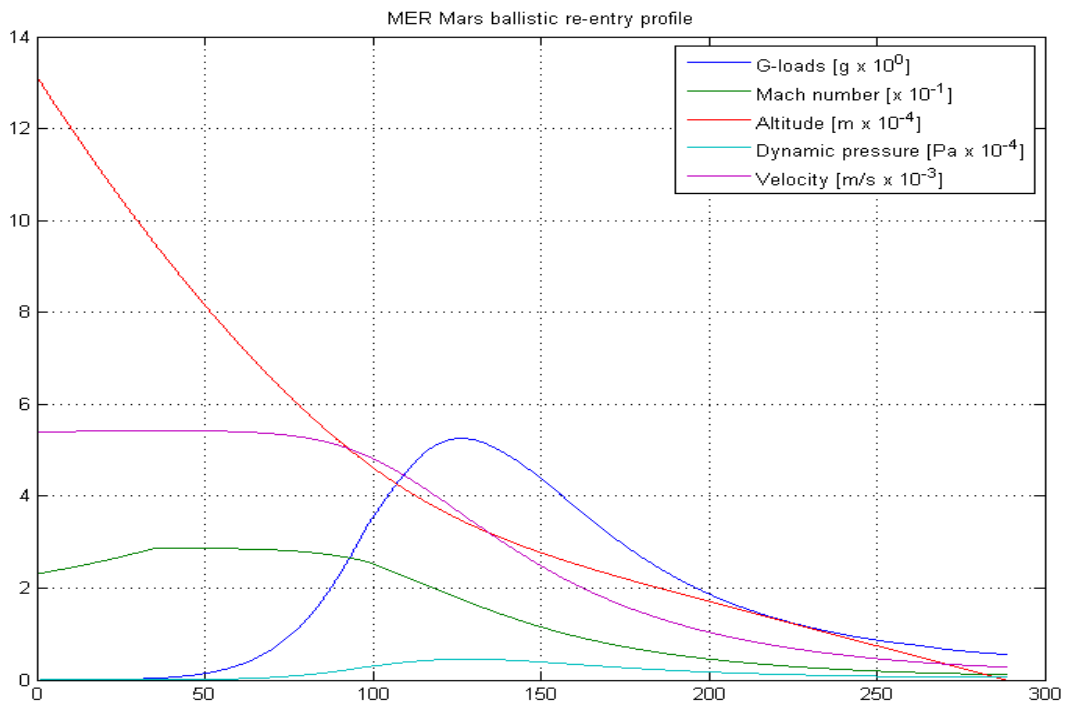


Figure 52. The MER ballistic re-entry profiles. All y-axis values are multiplied by the value provided in the legend.

The MER parachute is modeled the same way as the earth ballistic study case, by increasing the reference area and correct for the drag coefficient of the vehicle as described in subparagraph 4.1.3. The real MER parachute has a diameter of 14 m and with a vehicle drag coefficient of about 1.57. A corrected reference area of 45 m² is calculated using Eq. (9) and a drag coefficient of 0.41 in the deployment Mach range, which is consistent with reference¹⁴. Because the Monte Carlo simulation will generate randomized parachute deployment initial conditions, the parachute phase should be modeled during the Monte Carlo analysis itself. For this reason the parachute downrange is modeled as a quadratic regression of the deployment

velocity. Using the nominal trajectory, the parachute phase downrange is calculated at four different initial deployment velocities. From these four points a quadratic regression is generated which is shown in Figure 53. This regression is used to calculate the final downrange.

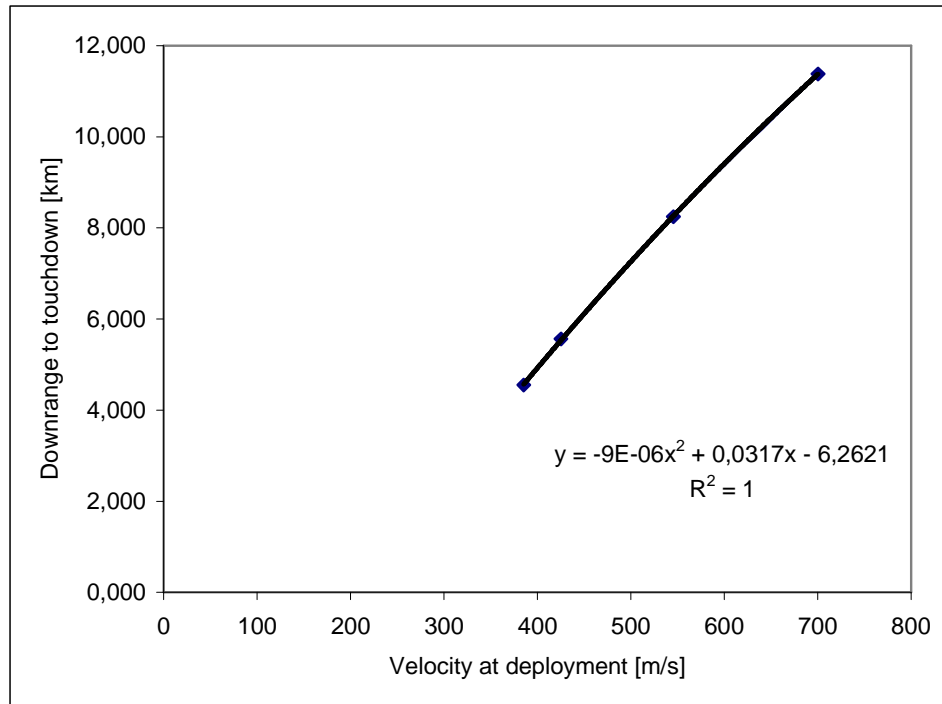


Figure 53. *Parachute phase quadratic regression modeling.*

Reference⁵ indicates a footprint contribution breakdown of different types of uncertainties. In order to compare the current Monte Carlo case to the case provided in this reference, three 1000 run Monte Carlo simulations are performed with these different types of uncertainties:

- 1) Aerodynamic uncertainty, the uncertainty due to the deviations from the measured and the real aerodynamic coefficients.
- 2) Navigational errors: Errors in the determination of the longitude, latitude and the heading. Also the de-orbiting maneuver will cause can provide only a certain corridor in entry velocity and flight path angle.
- 3) Atmospheric uncertainties: The modeling error due to simplification and not completely known true conditions of the Martian atmosphere.

Because a 3 DOF model is used only the navigational errors will induce a two dimensional ellipse. Also the contribution of an angle of attack bias is neglected, because the vehicle is spinning with 2 rpm, the bias is also rotating which mostly cancels itself out. Figure 54 shows the footprint of the three footprint contributions and Table 25 shows the numbers corresponding with the figure.

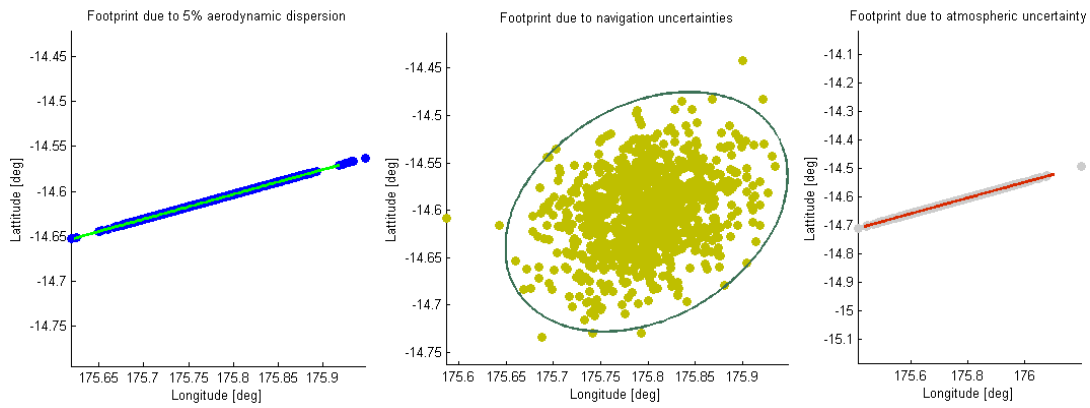


Figure 54. Footprint contributions of different types of uncertainties.

These footprint contributions will make up the total landing ellipse as presented in Figure 56. The separate contributions are comparable but not the same as mentioned in reference⁵. The difference between the reference and the calculated values exist, because a different ellipse calculation method is used and a different atmosphere model is used. Wind modeling was not performed; however, this contribution is small (1 Km x 3 Km)⁵. Also dust storm and post dust storm conditions are not considered, because landing in these dusty conditions is considered to be unsafe for the hardware.

| | Long axis [Km] calculated | Short axis [Km] calculated | Long axis [Km] reference | Short axis [Km] reference |
|---------------------|------------------------------|-------------------------------|-----------------------------|------------------------------|
| Aerodynamic | 18.0 | 0.0 | 13 | 3 |
| Navigation | 18.8 | 13.0 | 32 | 3 |
| Atmosphere | 40.8 | 0.0 | 38 | 0.1 |
| Wind | 0.0 | 0.0 | 3 | 1 |
| Total 99 % ellipses | 48.4 | 13.0 | 51.4 | 4.4 |

Table 25. Ellipse sizes of the footprint contributions of different types of uncertainties.

Table 26 contains the data from the Monte Carlo analysis which is compared to NASA trajectory reconstruction from the real MER mission¹⁸. For a first reconstruction attempt the results are very satisfying: Mars rover “Opportunity” has landed within the determined landing ellipse and is 5.53 km of the nominal determined landing point, unfortunately, Mars rover “Spirit” has landed outside of the landing ellipse and is 19.20 km from the nominal landing point. Also the determined deployment conditions¹⁸, except Spirit deployment altitude, can be reconstructed within a 5% error.

| MER A (Spirit) | | | | | | | |
|----------------------|-------------|--------------------|---------------|--------------------|------|--------|------|
| | Real value* | Standard deviation | Nominal value | Standard deviation | Unit | Error | Unit |
| Deployment longitude | 175,411 | 0,013 | 175,710 | 0,130 | deg | -17,69 | km |
| Deployment latitude | -14,528 | 0,039 | -14,628 | 0,053 | deg | 5,95 | km |

| | | | | | | | |
|--------------------------------|---------|-------|----------|---------|-----|--------|----|
| Landing longitude | 175,478 | | 175,801 | 0,130 | deg | -19,11 | km |
| Landing latitude | -14,572 | | -14,603 | 0,053 | deg | 1,82 | km |
| Deployment altitude | 7500 | 1700 | 6261,007 | 590,697 | m | -16,52 | % |
| Dynamic pressure at deployment | 725 | | 757,772 | 26,376 | Pa | 4,52 | % |
| Velocity at deployment | 410,98 | 0,77 | 425,420 | 8,750 | m/s | 3,51 | % |
| MER B (Opportunity) | | | | | | | |
| Deployment longitude | 354,413 | 0,013 | 354,470 | 0,131 | deg | -3,39 | km |
| Deployment latitude | -1,957 | 0,041 | -1,979 | 0,041 | deg | 1,28 | km |
| Landing longitude | 354,474 | | 354,564 | 0,131 | deg | -5,35 | km |
| Landing latitude | -1,948 | | -1,972 | 0,041 | deg | 1,40 | km |
| Deployment altitude | 6200 | 1800 | 6240,644 | 591,051 | m | 0,66 | % |
| Dynamic pressure at deployment | 750 | | 759,289 | 26,361 | Pa | 1,24 | % |
| Velocity at deployment | 429,68 | 0,81 | 425,442 | 8,761 | m/s | -0,99 | % |

Table 26. Real landing and deployment conditions compared with the calculated conditions.

It appears FMST is also very suitable for re-entry simulation on Mars. If FMST is to be used for Mars GNC mission analysis, recommendations for more accurate and verified trajectory reconstruction for FMST are:

- The use of an official Mars atmosphere model, tailored to each specific re-entry case: Deployment conditions for both vehicles are the same in the used analysis because the same atmospheric model is used for both cases, apparently this model used resembles more the Opportunity profile than the Spirit profile.
- Second order term gravity modeling, as recommended and provided in reference¹⁸
- Shape modeling, in order to improve the current spherical shape to a more accurate ellipsoid.

However, for a footprint reduction case study this reconstruction is sufficient, because the footprint performance is compared to the self made nominal case and not in the reference⁵ determined footprint and real landing location.

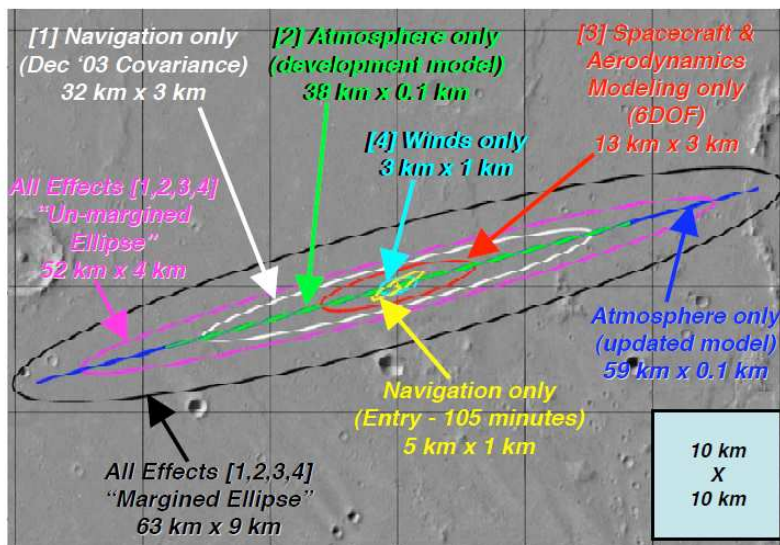


Figure 55. Spirit footprint as defined by ref⁵.

Figure 56 and Figure 57 show the determined 99.7% landing ellipse together with the real landing locations and for Spirit, also the NASA target location out of 10000 Monte Carlo Simulations. The total ellipse length is 54.43 km for Spirit and 53.31 km for Opportunity. These values are comparable with the un-margined ellipse of figure 1 in reference⁵, see Figure 55. However, these ellipses are generated by applying 3 σ values on both axis of the ellipse; this actually generates a 99.4% ellipse, assuming a fully Gaussian distribution.

Due to the atmospheric uncertainties, the footprint dispersion will be not truly Gaussian.

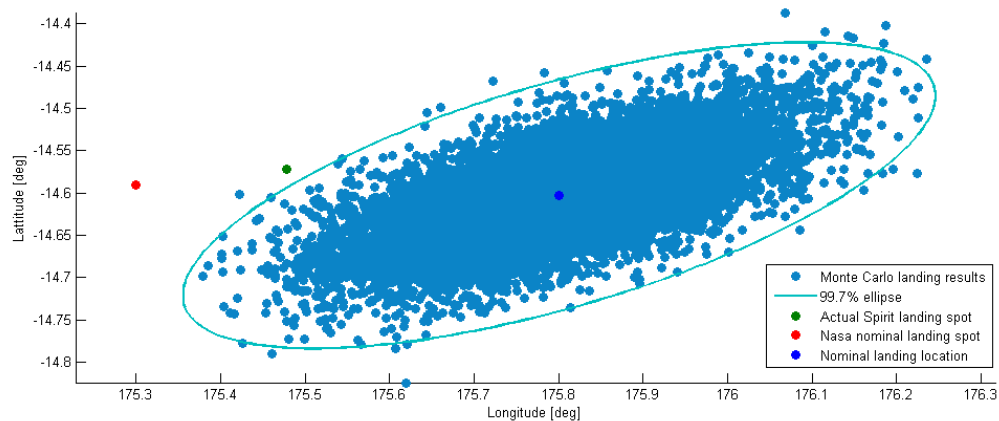


Figure 56. MER A (*Spirit*) reconstructed footprint together with the real and the planned landing site.

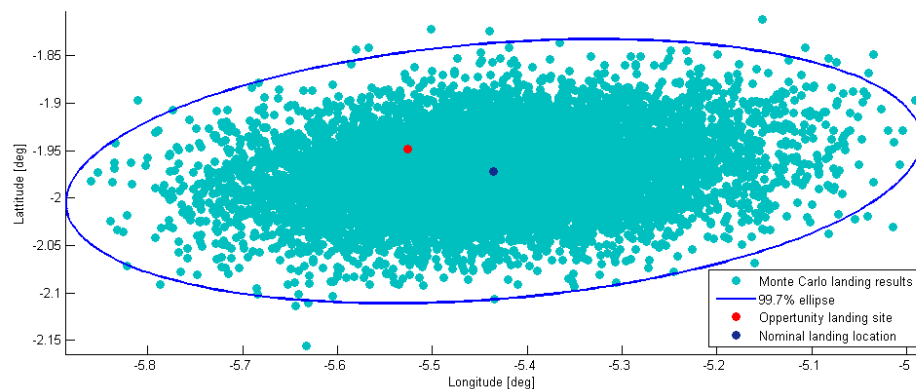


Figure 57. MER B (*Opportunity*) reconstructed footprint together with the real and the planned landing site.

4.3.2 Footprint reduction

To produce a baseline for a footprint reducing algorithm, the analysis is performed two times. The first analysis is based on deployment on exact knowledge of the vehicle's longitude. The sensor part is left out in this case in order to analyze the size of the footprint reduction possible by changing the deployment time, which is limited by the parachute's deployment capabilities in terms of Mach number. Acquiring position information during flight by sensors could be obtained by correlating ground images made during flight with a ground map database. This

would be a new technology to be developed and for this reason a second analysis is performed. This analysis uses g-load correlations in order to predict the downrange flown and correct it by parachute deployment. This estimation is independent of navigational inputs. This results in an easy implementable algorithm, but has less footprint reduction performance.

The goal of the combination of this double analysis is to have a clear indication of the maximum footprint reduction achievable, which is limited to the parachute capabilities and to determine minimum footprint reduction requirements, which are driven by the navigation system capability. For the footprint reduction analysis the trajectory of the MER-A vehicle (Spirit) is used.

4.3.3 Footprint reduction limited on parachute capabilities

The ideal case footprint reduction algorithm compares the longitude to the nominal trajectory. Since the heading of Spirit is around 74 deg, latitudinal information is not necessary. As mentioned in subparagraph 4.1.2, three settings are used, undershoot, nominal and overshoot. The developed algorithm compares its position to the nominal case and if it is more than 0.05 deg to far it will deploy the parachute at the high Mach value, if it is within +/- 0.05 deg it will deploy on its nominal value and if it is more than 0.05 deg to short it will deploy at the low bound Mach number. In reality such a navigation rule can be implemented by combining geographic orientation and knowledge of the velocity.

Figure 58 and Figure 59 show the results of possible footprint reduction for 2 cases: The first case uses a Mach opening range from Mach 2.1 to 1.6, which is within the qualification of the Viking based parachutes. The footprint size reduces from 54.53 km to 46.902 km, which is a reduction of 7.628 km. This is a reduction of 14 % compared to the original ellipse. This can be the reduction when only the navigation systems are updated and already flight-proven Viking technology is used. For a more significant reduction, a second case is studied using a parachute which is able to be opened at a higher Mach number. In this case a parachute is modeled which is capable of deployment at Mach 3. A higher Mach number deployment than Mach 3 has not been investigated, because it would come to close to the control limit reduction of 66.7%, which is explained in subparagraph 4.1.2 and also due to the aerothermal constraints of the currently used materials. Such kind of parachute would be able to reduce the footprint from 54.75 to 30.52 km, which is a reduction of 24.23 km or 44 %.

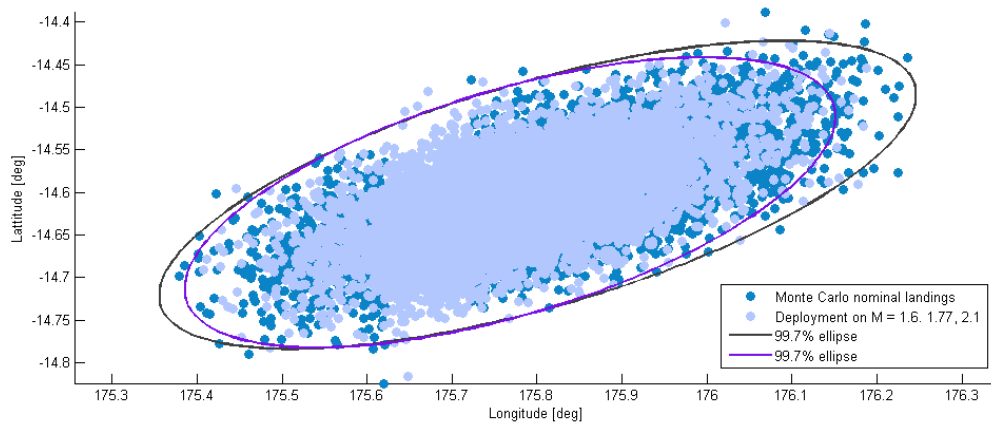


Figure 58. Footprint reduction possible using qualified Viking parachutes.

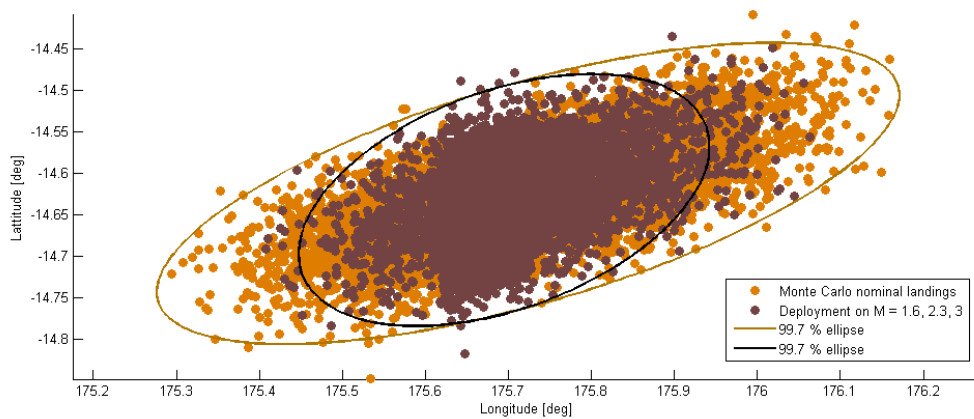


Figure 59. Footprint reduction possible, using a parachute capable of deployment up till Mach 3.

The footprint reduction achievable is mainly a function of two related parameters; the Mach deployment window and the maximum deployment Mach number. The footprint reduction capability increases exponentially if the parachute's maximum Mach number is increased, because the Mach opening window will get larger, the velocity is higher so more distance can be covered and the flight path angle is shallower. This can be seen in the isobar plot of Figure 60. A higher Mach number deployment is also desirable to land at higher elevations on Mars⁶. Development of a parachute with a higher opening velocity than current Viking technology might be designed with both benefits in mind. The use of a ballute might be an option for such kind of decelerator.

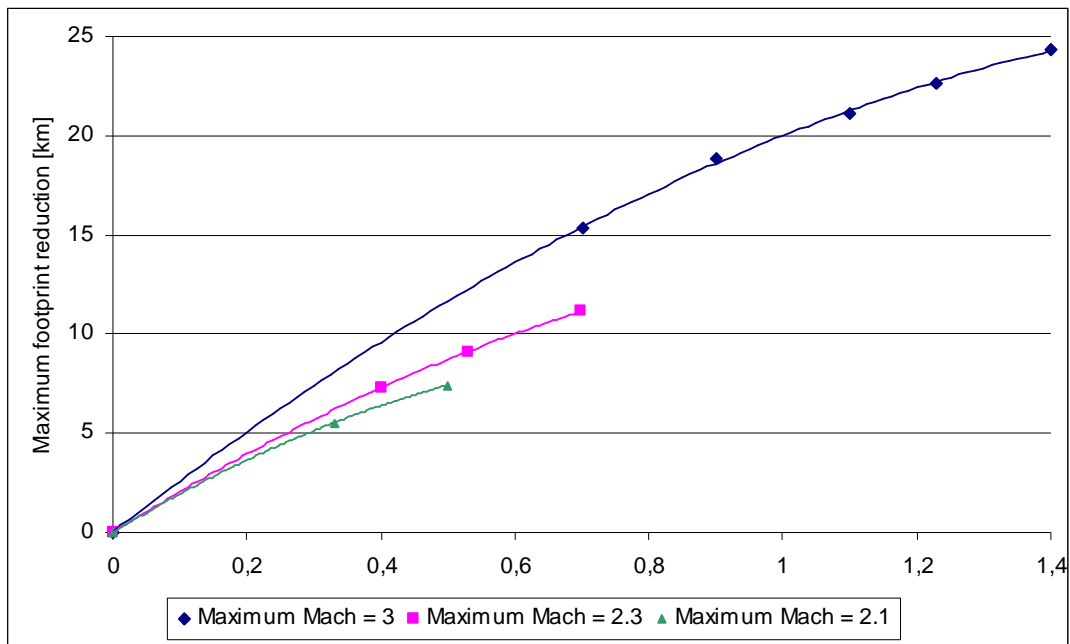


Figure 60. Footprint reduction possible as a function of the maximum parachute deployment Mach number and the Mach opening window.

4.3.4 Footprint reduction using g-force correlations only

To specify minimum requirements, g-load correlations are used in order to define the desired instant of parachute deployment. For such an algorithm, four correlations are needed:

1. A correlation to determine the downrange from the initial point, this is a function of the actual vehicle mass, aerodynamic uncertainties, the flight true flight path angle and most of all, the actual atmospheric conditions. For such an algorithm, no navigational errors can be corrected.
2. High velocity deployment
3. Nominal velocity deployment
4. Low velocity deployment

As mentioned in subparagraph 4.1.2, only three logical conditions are investigated to simplify the algorithm. In similar way as for the ballistic re-entry case, multiple algorithms are examined on their correlation. This time however, the strongest correlating algorithm, the g-slope correlation, is chosen and now different values are used. For the downrange prediction it is determined that correlation and the start of the re-entry provides the best correlation. This, is because the high uncertainties in the atmosphere are poorly correlated and overruling downrange parameters like the flight path angle and initial velocity dispersions.

| First g-load threshold | Second g-load threshold | Correlated with | Downrange correlation | Mach 3 correlation | Mach 2.3 Correlation | Mach 1.6 correlation |
|------------------------|-------------------------|-----------------|-----------------------|--------------------|----------------------|----------------------|
| 0,3, first | 1, first | - | 0,408 | 0,064 | 0,066 | 0,066 |
| 0,3, first | 2, first | - | 0,642 | 0,308 | 0,310 | 0,311 |
| 0,3, first | 3, first | - | 0,814 | 0,567 | 0,569 | 0,571 |
| 0,3, first | 4, first | - | 0,727 | 0,664 | 0,665 | 0,668 |
| 1, first | 1, last | 3g | NA | NA | NA | 0,157 |
| 2, first | 2, last | 3g | 0,226 | 0,073 | 0,142 | 0,055 |
| 3, first | 3, last | 3g | 0,309 | 0,539 | 0,515 | 0,553 |
| 4, first | 4, last | 3g | 0,295 | 0,392 | 0,452 | 0,255 |
| 4, last | 3, last | 3g | 0,027 | 0,556 | 0,630 | 0,390 |
| 4, last | 2, last | 3g | 0,085 | 0,672 | 0,745 | 0,506 |
| 4, last | 1, last | 3g | 0,098 | 0,747 | 0,810 | 0,590 |
| 3, last | 2, last | 3g | 0,134 | 0,741 | 0,807 | 0,584 |
| 3, last | 1, last | 3g | NA | NA | NA | 0,672 |
| 4, last | 3, last | 4g | 0,033 | 0,806 | 0,840 | 0,717 |
| 4, last | 2, last | 4g | 0,035 | 0,880 | 0,912 | 0,796 |
| 4, last | 1, last | 4g | 0,043 | 0,920 | 0,944 | 0,846 |
| 3, last | 2, last | 4g | 0,095 | 0,890 | 0,916 | 0,815 |
| 3, last | 1, last | 4g | NA | NA | NA | 0,871 |

Table 27. Correlations of different g-load thresholds to the downrange and the desired deployment conditions.

From Table 27 the g-load thresholds which have the strongest correlation to the downrange prediction and the desired Mach numbers are selected. These correlations are shown in Figure 61. Although no navigation input is added, the downrange can be predicted by correlating it with the time between g-load thresholds at an early phase during the re-entry with a R^2 of 0.81. The downrange is divided into an undershoot range, a nominal range and an overshoot range. These downrange prediction ranges activates one of the other 3 correlations which are used to determine the selected deployment Mach number similar as described in subparagraph 2.4.2.

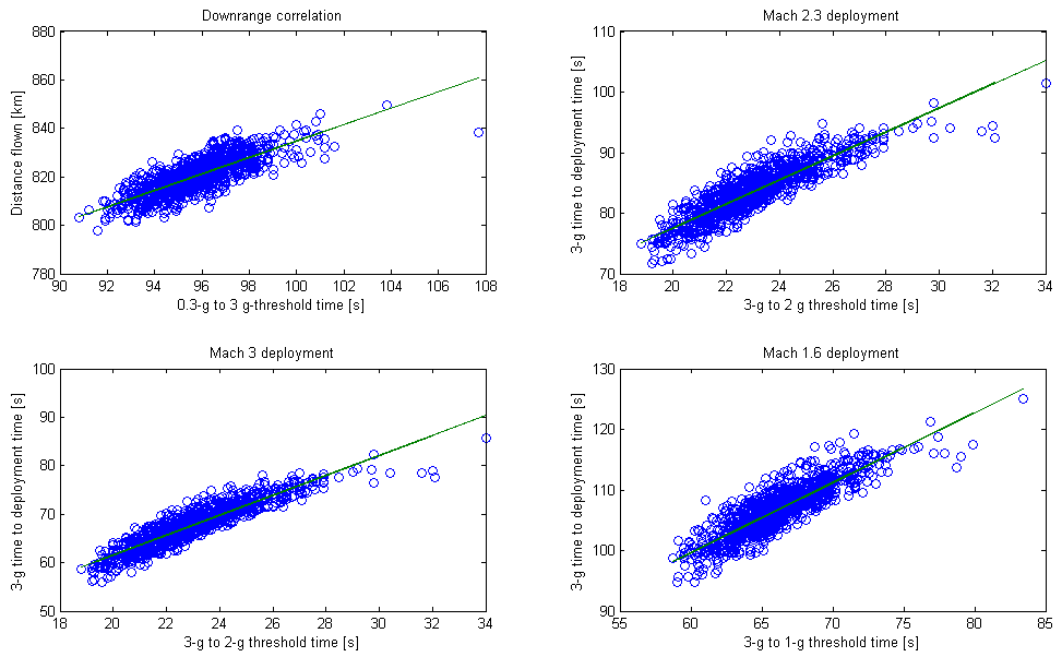


Figure 61. Correlations of the selected g-load thresholds to the downrange and the desired deployment conditions. R^2 vales are: 0.81 ,0.89 0.92,0.87 from upper left to right and down left to right respectively.

These correlated algorithms lead again to a higher accuracy than an uncorrelated trigger, for nominal deployment at Mach 1.77 a correlated g-slope algorithm has a dispersion of $0.191\ 3\sigma$ and a direct g-trigger has a dispersion of $0.265\ 3\sigma$. Using these correlations another 10000 run Monte Carlo simulation is performed in order to estimate the footprint. Figure 62 presents the results.

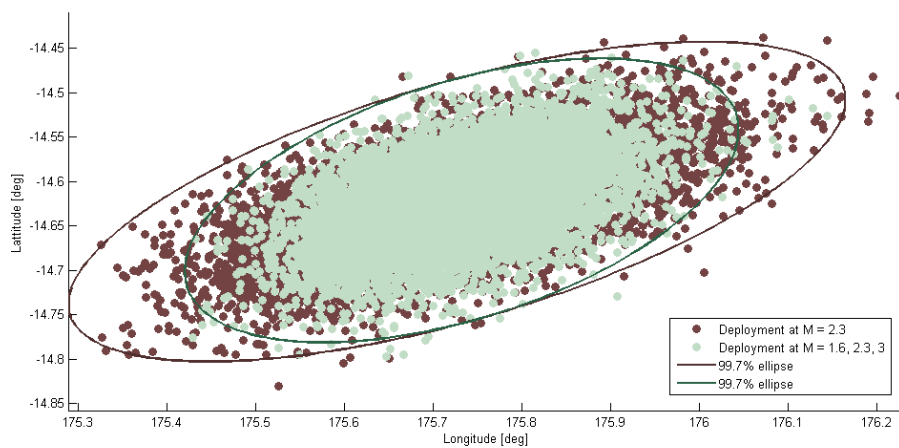


Figure 62. Footprint reduction using a parachute capable of deployment up till Mach 3 and g-load correlations only.

The footprint ellipse is reduced from 53.54 km to 38.23, a reduction of 15.31 km, which is 10 km less than the “ideal” case. Furthermore A remark must be made of the mathematical background of the generation of the 3σ ellipse. The developed

ellipse is such that the 2-dimensional probability is 99.73%, assuming a Gaussian circular distribution¹⁷. However, the perfect navigation control algorithm creates stepwise changes in the simulation, which makes the PDF leptokurtic with a kurtosis (the “peakness” of the curve compared to a true Gaussian distribution) of 6.15, whereas the nominal landing footprint has a slightly platykurtic PDF of 2.94.

To give a better view on the landing site distribution contour plots have been made, which are presented in Figure 63. The figure shows that the algorithm creates a concentrated centre circle and a large area with still a significant probability of a landing. This could be explained by the insertion coordinate dispersion, which cannot be compensated for since it is uncorrelated with the g-loads. It represents the R^2 of 0.81, from which the 0.19 are the “false decisions” made by the algorithm, which create this “plateau”. An example when this happens is when the insertion is further downtrack as intended, while there is a denser atmosphere than expected: The denser atmosphere will be picked up by the g-load measurements, due to a higher deceleration, so the algorithm will decide that the vehicle might come short to its landing target and will open the parachute at the latest moment. However, the further insertion cannot be detected by the g-load measurement and due to the decision of the algorithm the vehicle will in the end overshoot its landing target, whereas if no corrections were made, the vehicle might have landed very close to the intended landing zone. These kinds of scenarios could explain the 10 km difference in footprint reduction.

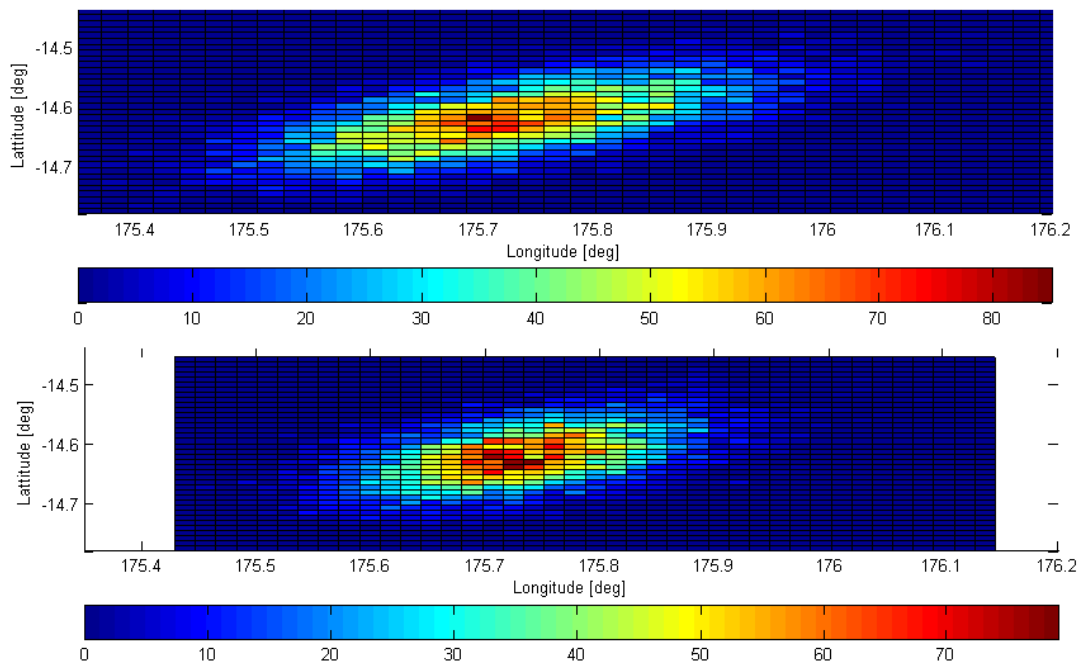


Figure 63. 2D histogram of the landing site dispersion for *nominal deployment only (upper) and using g a parachute capable of deployment up till Mach 3 and g-load correlations only (lower)*.

Figure 64, Figure 65 and Figure 66 display the deployment dispersions for the Mach number, the altitude and the dynamic pressure as performed by the footprint reduction algorithm. These 3 peaks represent the 3 different Mach number deployment conditions. The Mach number and dynamic pressure have a dispersion

of around 10% and 7.5 % respectively from their mean, whereas the altitude dispersion is the same for every deployment of around $1.7 \text{ km } 3\sigma$.

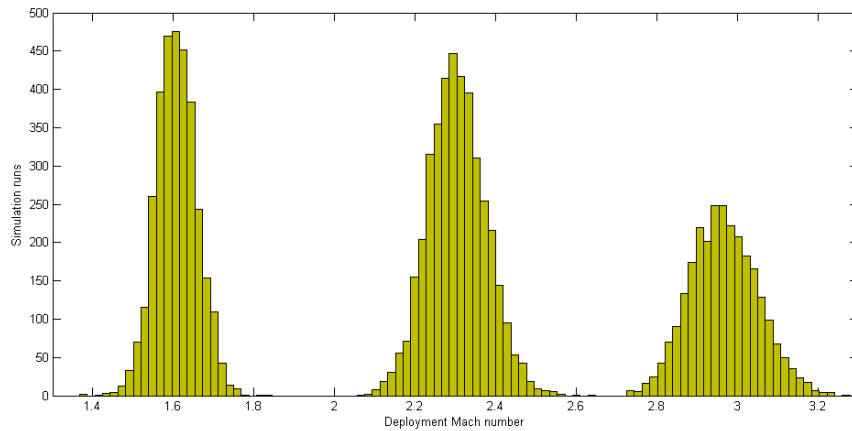


Figure 64. Mach dispersions of the g -load correlated deployments. The three dispersions clearly indicate the 3 separate instants of deployment, depending on the required downrange.

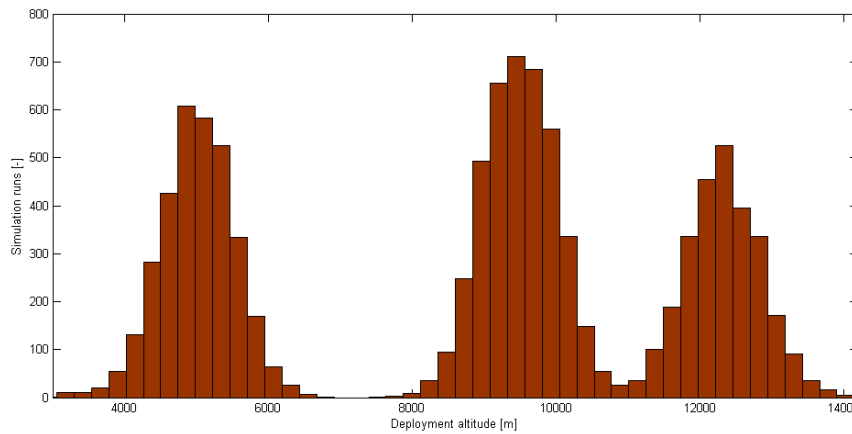


Figure 65. Altitude dispersions of the g -load correlated deployments. The altitude dispersion at the deployment is around $1.7 \text{ Km } 3\sigma$ for of all three different Mach numbers.

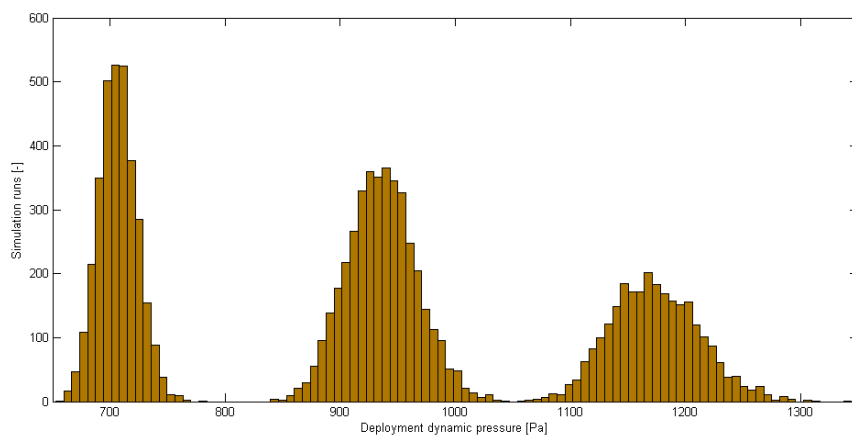


Figure 66. Dynamic pressure dispersions of the g -load correlated deployments. Current Viking maximum deployment dynamic pressure is 1100 Pa ; the high Mach number parachute should be able to withstand 1300 Pa .

4.4 Conclusions

Footprint reduction by the use of a dynamic opening window of the parachute is found to be ineffective on Earth, because the reduction will be around an order of magnitude smaller than the total footprint. Footprint reduction using a dynamic opening window has potential on Mars. A reduction of 25 km could be achieved if current Viking parachute technology is stretched to a maximum Mach number of 3 for a MER like mission. If simple g-load correlations are used instead of a still to be developed navigation system, this reduction would be 15 km. A higher opening velocity is already desired in order to be able to land on the Martian highlands. Modified parachute designs can be developed to incorporate both benefits.

FMST was used to reconstruct the MER trajectory and footprint and has found to be very suitable to use for Mars re-entries: The landing site estimation was 19.20 and 5.53 km from the actual landing site. However the use of verified Martian atmosphere models and verification and elaboration of the Mars model is recommended if this tool would be used for analysis of future Mars missions. In the future usage of a ballute as decelerator device may extend the usable Mach range and thus increase the possibility of footprint reduction.

5 Conclusions

This parachute triggering investigation involved three cases, a ballistic re-entry and a lifting re-entry on Earth and a ballistic re-entry on Mars. Because only study cases were used, no direct system design has been performed, but performance is set as a function of sensor accuracy to provide insight on the sensor requirements for future missions. Together with the design logic presented, they can be used for future mission design. This is in compliance with the mission need statement. However, incompliant to the mission need statement, a sound reliability study has not been performed, because system reliability data of the proposed to be used systems was not available. A reliability study of hypothetical systems of a hypothetical mission was decided to be too arbitrary and therefore the focus was aimed to improve the methodology and the measurements only. Also the third goal was elaborated more than originally intended, because footprint reduction on Earth seems to be infeasible and a good opportunity was noticed for a Mars mission, a new Mars study case has been developed.

For the earth ballistic re-entry it can be concluded that correlated algorithms outperform the current used threshold triggers on accuracy 2 to 3 times and the ability to adapt to off-nominal re-entry due to degraded de-orbiting. The g-load curve has higher correlations than similar measurements on the pressure curve. This is because the aerodynamic uncertainty influences the altitude and velocities and so providing different readings, whereas measuring the deceleration is less influenced by this trajectory difference. It appears that measuring the g-load slope just before deployment and measuring the g-load peak have the best correlation and the most accurate results, but not compliant to the primary goal of a 3σ success rate. With the scenario set, compliance is impossible, because the dispersions are such that in 64 out of 10000 cases the deployment Mach number is located outside the altitude bound, which makes it an imminent failure. For comparison purposes, this poses no problem. Measuring or estimating the dynamic pressure and deploy at a preset setting is an exception for a not correlated algorithm to perform compliant to a less than 3σ failure, when altitude is not taken into account, but physically measuring this pressure will be very challenging. Furthermore static pressure probes perform not compliant, but are not ruled out for usage because of the possibility to use it as redundant sensors.

Adding a time delay between the measurement and the actual deployment has the benefits of providing processing time for noise reduction and removing the axial g-load measurement error for a possible angle of attack oscillations divergence. Alternatively, a lateral g-load trigger can be used to prevent angle of attack oscillation escalation.

One of the developed correlated g-load algorithms was implemented on the EXPERT mission model and proved to have a far superior performance over the current design and could also cope with an off-nominal scenario.

For the lifting re-entry, drag derived measurements are found to be a very suitable non-intrusive measurement method to estimate deployment conditions. The velocity measurement by the IMU is the driving parameter for parachute triggering by a

factor of 10, compared to all other measured variables used for the drag derived measurements. The 3σ success rate will depend on the accuracy of the velocity estimation of the IMU (Inertial Measurement Unit). Furthermore, assuming a constant stratosphere temperature might already provide sufficiently accurate Mach estimation for parachute deployment. This removes extra calculation and measurement steps compared to the drag derived measurements. Unfortunately, at the most extreme part of the re-entry, no easy achievable back-up exists if the IMU fails. If there is a failure at this most extreme part static pressure measurements can be used only as a last resort. It is undesirable, because the altitude information does not have correlation with the flown flight path.

The highest risk to the triggering success rate is wind, because this investigation did not succeed to estimate this parameter accurately. The best chance to estimate this value is determined to be a drag derived method together with a static pressure measurement. However with the discrepancy of the axial-force drag coefficient (C_A) found in the Flight Mechanics Simulation Tool (FMST) accurate estimation was not possible. But if this issue assumed to be resolved and just neglected as a bias, still a high dispersion of 73.97 m/s 3σ was achieved and therefore a successful implementation of such a system remains questionable.

Because the velocity estimate is found to be the driving parameter and the opportunity to have an accurate estimate of deployment conditions only for this measurement it is recommended from reliability point of view to fly with a redundant IMU which would at least be able to estimate this velocity. Alternatively GPS should be considered to remain as back-up to provide a two fault tolerant system. From these developed and analyzed methods a strategy was developed to determine the optimum method at each situation during flight.

Footprint reduction by the use of a dynamic opening window of the parachute is found to be ineffective on earth, because the nominal reduction would be less than 10 % of current footprints. However, it has a potential on Mars: A reduction of 25 km, or 44% of the original footprint, could be achieved if current Viking parachute technology is stretched to a maximum Mach number of 3 for a MER like mission. If simple g-load correlations are used instead of a still to be developed navigation system, this reduction would be 15 km, which is a reduction of 29% of the original footprint. A higher opening velocity is already desired in order to be able to land on the Martian highlands. Modified parachute designs can be developed to incorporate both benefits.

The Flight Mechanics Simulation Tool (FMST) has proven to be a very useful and versatile tool to analyze the re-entry trajectory, but also to develop the parachute triggering algorithms. Furthermore it has proven to be capable of analyzing re-entry trajectories on Mars. However, for specific mission purposes it could be expanded to suit specific demands.

The Mission Need Statement required a system level analysis of the reliability of a triggering system. However it was deliberately chosen to not perform this analysis, because the analysis depends on the available hardware of a specific mission which was not available. During the generation of the Mission Need Statement it was assumed such information would be available on the future ESA missions in a later

stage, however this was not the case. For this reason no in dept study on system level was performed but the focus was aimed at design methodology and the footprint reduction. So because the implementation of the algorithms on the hardware depends on the availability of the hardware of each specific mission, no recommendations are performed on this matter.

6 Recommendations

For the analysis and design of parachute triggering algorithms for ballistic vehicles it is recommended to investigate the use of correlated algorithms. On the real EXPERT mission data the results were very promising. Furthermore such an algorithm might also be considered to use on a Mars mission, since it would be able to cope with the large atmospheric uncertainties. Footprint reduction by the use of a dynamic parachute opening window is determined to be infeasible for Earth, but is worth incorporating for a re-entry on Mars, assuming current footprint sizes.

For a lifting re-entry it can be recommended to incorporate some way of drag derived measurements in order to estimate all parachute deployment conditions during flight, however an accurate estimation of the flight velocity is the critical parameter in this estimation and redundancy of this parameter is recommended. Furthermore a wind dispersion study still has to be performed. For implementation point of view it is disappointing a thorough wind analysis could not have been incorporated, because it is a critical parameter for parachute deployment. The results of this investigation are to perform the mission at low wind conditions, because estimation of the wind during flight proved to be unsuccessful.

Future expansions to improve the versatility of FMST might be:

- Implementation of a smooth and verified method of the determination of the C_A in order to implement drag derived measurement analysis.
- A simple implementable method to incorporate the parachute phase or phases to model the end-to-end trajectory.
- Verification for Martian re-entry trajectories, this should mainly consist of:
 - The use of an official Mars atmosphere model, e.g. GRAM, tailored to each specific re-entry case: Deployment conditions for both vehicles are the same in the used analysis because the same atmospheric model is used for both cases; apparently this model used resembles more the Opportunity profile than the Spirit profile.
 - Second order term gravity modeling and ellipsoid of Mars, as recommended and provided in reference¹⁸.

These relatively small extensions can give FMST interesting opportunities for the analysis and design for different aspects for future missions. The expansion for broader use of this tool is definitely recommended.

All outcome distributions were assumed to have a Gaussian distribution, which is from mathematical point of view a poor implantation. The Matlab statistics toolbox was used to perform Kolmogorov-Smirnov tests, from which the tested distributions all failed. Fortunately, because the Monte Carlo analysis is discrete, the actual success rates and dispersion can simply be counted, avoiding all mathematics involved. Since the type of distribution is in the industry a design parameter, proper agreement on the type of the distribution and the deviation from it should be considered.

Bibliography

¹Colombattia, G., P. Withers, F. Ferri, A. Aboudan, A.J. Ball, C. Bettanini, V. Gaborit, A.M. Harri, B. Hathi, M.R. Leese, T. Makinen, P.L. Stoppato, M.C. Towner, J.C. Zarnecki, F. Angrilli, M. Fulchignoni, *Reconstruction of the trajectory of the Huygens probe using the Huygens Atmospheric Structure Instrument (HASI)*, www.elsevier.com, 5 December 2007

²Crowley, G., M. A. Bullock, C. Freitas, D. Boice, L. Young, D. H. Grinspoon, R. Gladstone, R. Link and W. Huebner, *DEVELOPMENT OF A SURFACE-TO-EXOSPHERE MARS ATMOSPHERE MODEL.*, Southwest Research Institute, San Antonio, Texas, U.S.A.

³Gerald Pignie, Patrick Delaux, Laurent Bouaziz, Hamid Kebci, François Trinquard, *Parachute Opening Triggering Algorithm Of The Atmospheric Re-Entry Demonstrator*, Aiaa Gnc Conference, July 29-31 1996, San Diego, CA

⁴Desai, Prasun N., Dan T. Lyons, Jeff Tooley, Julie Kangas, *Entry, Descent, and Landing Operations Analysis for the Stardust Entry Capsule*, NASA Langley Research Center, Hampton, VA, 23681-2199

⁵Knocke, Philip C., Geoffrey G. Wawrzyniak, Brian M. Kennedy, *Mars Exploration Rovers Landing Dispersion Analysis*, AIAA/AAS Astrodynamics Specialist Conference and Exhibit, Providence, Rhode Island, 16-19 August 2004, AIAA 2004-5093

⁶Manning Robert M., Adler, Mark, *Landing on Mars*, AIAA Space 2005 Conference, California, Long Beach, AIAA-2005-6742

⁷Mooij, Ir. E., *THE HORUS-2B REFERENCE VEHICLE*, Memorandum M-692, Delft University of Technology, Delft, May 1995

⁸Muylaert, Jean, Francesca Cipollini, Giorgio Tumino, Willi Kordulla, Giorgio Saccoccia, Constantinos Stavriniadis, *Preparing for Atmospheric Reentry with EXPERT's Help, An Aerothermodynamic In-Flight Research Programme*, esa bulletin 114, may 2003

⁹Myron R. Grover III, Benjamin D. Cichy, *Overview of the Phoenix Entry, Descent and Landing System Architecture*, Jet Propulsion Laboratory, California Institute of Technology, Pasadena, CA, 91109, USA

¹⁰NASA, *GENESIS*, Mishap Investigation Board Report, Volume I, NASA

¹¹NASA. *STANDARD ATMOSPHERE 1976*, NASA-TM-X-74335, 1976

¹²Paulat, J.C.; Boukhobza, P., *Re-entry Flight Experiments Lessons Learned – The Atmospheric Reentry Demonstrator ARD*, In Flight Experiments for Hypersonic

Vehicle Development (pp. 10-1 – 10-46). Educational Notes RTO-EN-AVT-130, Paper 10. Neuilly-sur-Seine, France: RTO. Available from: <http://www.rto.nato.int/abstracts.asp>, 2007

¹³Prasun N. Desai, Robert A. Mitcheltree, F. McNeil Cheatwood, *Entry Dispersion Analysis For The Stardust Comet Sample Return Capsule*, NASA Langley Research Center

¹⁴Sengupta, Anita, Richard Kelsch, James Roeder, Mark Wernet, Allen Witkowski, Mike Kandis, *Supersonic Performance of Disk-Gap-Band Parachutes Constrained to a 0-Degree Trim Angle*, JOURNAL OF SPACECRAFT AND ROCKETS, Vol. 46, No6, November–December 2009

¹⁵Sudars M., A.Saluzzi, *Modeling of Parachute Dynamics in a Synthetic Flight Mechanics Simulations Environment*, AIAA-2009-2943

¹⁶Tumino, Giorgio, *The Ixv Project, The Esa Re-Entry System And Technologies Demonstrator Paving The Way To European Autonomous Space Transportation And Exploration Endeavours*, IAC-08-D2.6.01

¹⁷Wayne E. Hoover, *Algorithms For Confidence Circles and Ellipses*, NOAA Technical Report NOS 107 C&GS 3, Charting and Geodetic Services, Rockville, MD, September 1984

¹⁸Withers, Paul a., Michael D. Smith b, *Atmospheric entry profiles from the Mars Exploration Rovers Spirit and Opportunity*, Center for Space Physics, Boston University, USA, Elsevier, Icarus 185 (2006) 133-142

Pictures

¹⁹Figure 3: For Soyuz:
http://www.asc-csa.gc.ca/eng/newsletters/apogee/2009/11_article03.asp
For X-38:
<http://www.dutchspace.nl/pages/products/content.asp?id=322>

²⁰Figure 12: <http://www.parabolicarc.com/2009/07/17/esa-thales-alenia-space-sign-development-contract-experimental-reentry-vehicle/>

²¹Figure 51: http://marsrovers.jpl.nasa.gov/mission/images/aeroshell1_500.jpg

Appendix A, Matlab algorithms and FMST data extraction

This Appendix gives examples of Matlab code used for the three cases studied:

- 4) A ballistic re-entry trajectory on Earth
- 5) A ballistic re-entry trajectory on Mars
- 6) A lifting re-entry trajectory on Earth

Investigation 1: A ballistic re-entry trajectory on Earth

For the Earth ballistic re-entry case investigation a Matlab data extraction example is given from the g-slope algorithm from 8 to 6 g. No sensors are modeled, so the thresholds are simply extracted and stored after a Monte Carlo run. Also deployment conditions are stored:

```
% 6g time last
SimSensst.g6_index =
find((ScopeOut_gloads_tot(:,2)+g_meas_noise)>6,1,'last');
SimSensst.g6_trigger_time2(i_mc,1) = ScopeOut_M(SimSensst.g6_index);

% 8g time last
SimSensst.g8_index = find(ScopeOut_gloads_tot(:,2)>8,1,'last');
SimSensst.g8_trigger_time2(i_mc,1) = ScopeOut_M(SimSensst.g8_index);

% Nominal Mach
SimSensst.deploy_M_index = find(ScopeOut_M(:,2)<1.7,1,'first');
SimSensst.deploy_M_time(i_mc,1) =
ScopeOut_M(SimSensst.deploy_M_index);
% Minimum Mach
SimSensst.deploy_M_index_min = find(ScopeOut_M(:,2)<1.5,1,'first');
SimSensst.deploy_M_time_min(i_mc,1) =
ScopeOut_M(SimSensst.deploy_M_index_min);
% Maximum Mach
SimSensst.deploy_M_index_max = find(ScopeOut_M(:,2)<1.9,1,'first');
SimSensst.deploy_M_time_max(i_mc,1) =
ScopeOut_M(SimSensst.deploy_M_index_max);
% Nominal qbar
SimSensst.deploy_qbar(i_mc,1) =
ScopeOut_qbar(SimSensst.deploy_M_index,2);
% Altitude
SimSensst.deploy_alt(i_mc,1) =
ScopeOut_alt(SimSensst.deploy_M_index,2);
```

These stored thresholds are correlated with the stored deployment conditions after completion of a Monte Carlo batch:

```

% Correlation generation
real_output = SimSensst.deploy_M_time -
SimSensst.g6_trigger_time2;
cor_par = zeros(sensst.nruns,1);
cor_par(:) = SimSensst.g6_trigger_time2 -
SimSensst.g8_trigger_time2;
lower_bound = SimSensst.deploy_M_time_min -
SimSensst.g6_trigger_time2;
upper_bound = SimSensst.deploy_M_time_max -
SimSensst.g6_trigger_time2;

poly_coef = polyfit(cor_par,real_output,1)
cor = [poly_coef(1,1) poly_coef(1,2)]
fit_reg = polyval(poly_coef,cor_par);
%Define the R^2
Correlation = corrcoef(real_output, fit_reg)
subplot(4,4,11); plot(cor_par,real_output,'o',cor_par,fit_reg)
title('Case 16')
xlabel('Last 8g-last 6g time [s]')
ylabel('Deploy time-last 6g time [s]')

% Determine the success rate of the specific correlation
fail=0;
success=0;
for n = 1:1:sensst.nruns
    if (lower_bound(n) < (poly_coef(1,1)*cor_par(n) +
poly_coef(1,2)))
        fail = fail + 1;
    elseif (upper_bound(n) > (poly_coef(1,1)*cor_par(n) +
poly_coef(1,2)))
        fail = fail + 1;
    else
        success = success+1;
    end
end

success
fail

```

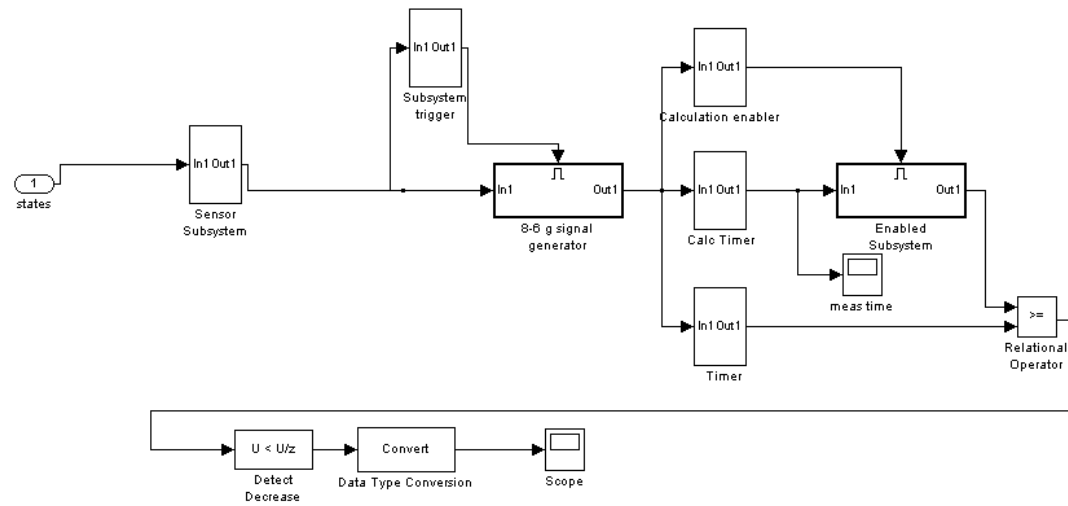
After the generation of the correlation a new Monte Carlo analysis is run to determine the deployment conditions as determined by the algorithm. These will then again be compared to the actual deployment conditions per Monte Carlo run:

```

% Case 16: 8g to 6g, last measurement time
g6_g8_meas = SimSensst.g6_trigger_time2(i_mc,1) -
SimSensst.g8_trigger_time2(i_mc,1);
g6_g8 = cor(1,1)*g6_g8_meas + cor(1,2);
g6_g8_index = find( SimOut_time(:,1) >
(SimSensst.g6_trigger_time2(i_mc,1) + g6_g8), 1,'first')-1;
g6_g8_deploy_m(i_mc,1) = ScopeOut_M(g6_g8_index,2);
g6_g8_deploy_alt(i_mc,1) = ScopeOut_alt(g6_g8_index,2);
g6_g8_deploy_qbar(i_mc,1) = ScopeOut_qbar(g6_g8_index,2);
g6_g8_deploy_time(i_mc,1) = ScopeOut_M(g6_g8_index,1);

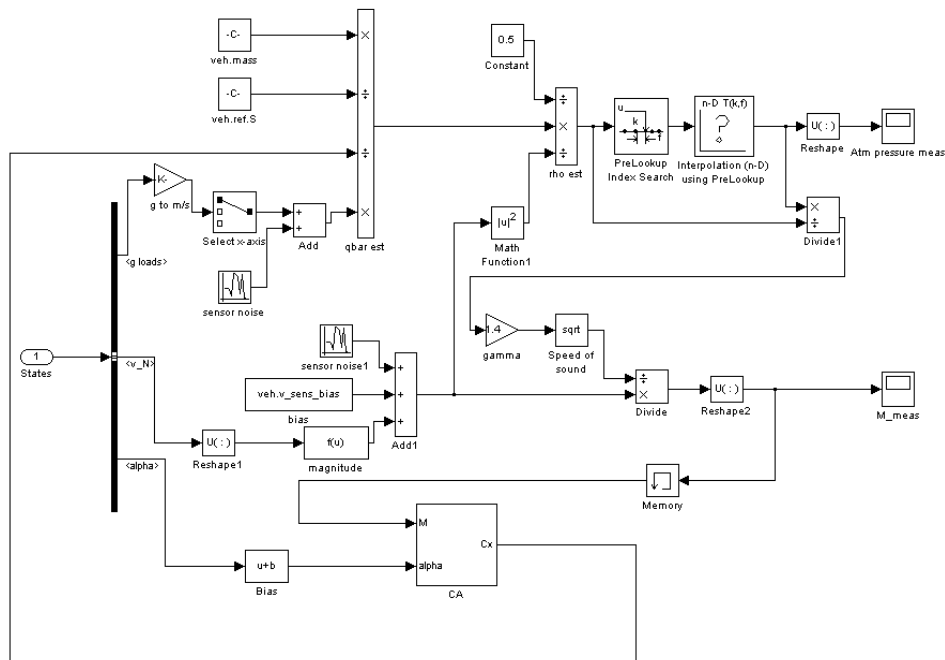
```

The best performing algorithms are converted to Simulink models. From the g-slope algorithm, the Simulink model is displayed below:

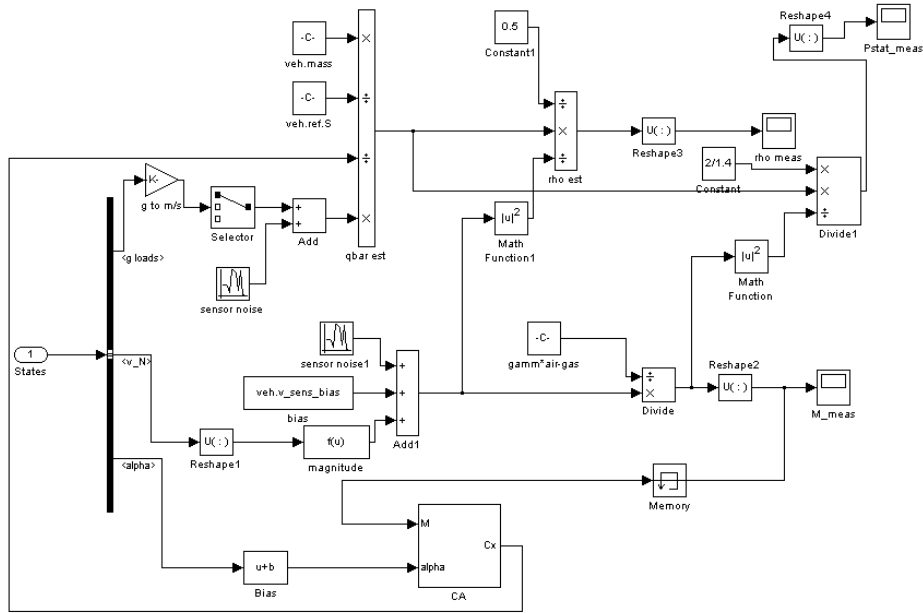


Investigation 2: A lifting re-entry trajectory on Earth

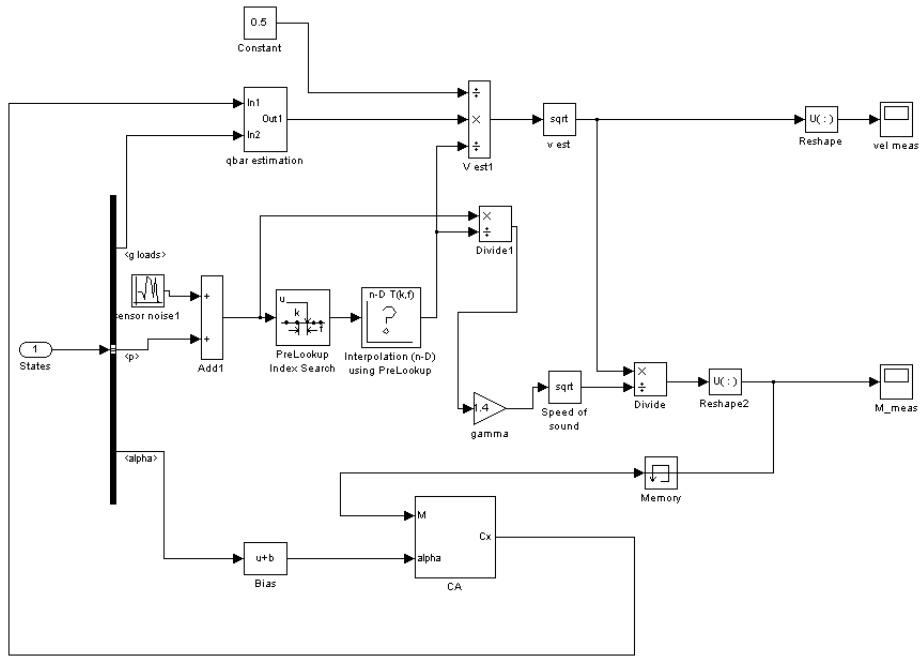
The second investigation involves only Simulink modeling concerning the drag derived measurements. From the velocity and the deceleration, the density is determined and this way, the speed of sound. The speed of sound is used with the velocity to determine the Mach number. The drag derived Mach estimation is depicted below:



The Mach estimation using constant temperature has a similar layout. However, it can be noticed $\gamma \cdot \text{air-gas}$ is inserted as a constant in the determination of the Mach number. In this case, the determined speed of sound is used together with the deceleration measurement to determine the density and the atmospheric pressure (and so, the altitude).



The velocity estimation using a drag derived measurement and a static pressure measurement is also derived from the previous models, however this time the static pressure is an input parameter, instead of the velocity:



For the open loop estimation a separate calculation file was made. The aerodynamic database of the Horus vehicle was inserted in this file and the trajectory is only estimated by assuming a constant decent rate and calculating the drag:

```

Cd = [0.10112  0.083694  0.0767114  0.0749679  0.0679942
0.0662418  0.0505598  0.0505598
0.124984  0.0953457  0.0831505  0.0726988  0.0639637
0.0639637  0.0482906  0.0482906
0.199444  0.141902  0.112272  0.0930854  0.0843504
0.0773856  0.059969  0.059969
0.329685  0.233787  0.181484  0.148341  0.125667
0.116941  0.0873472  0.0873472
0.520947  0.362285  0.285565  0.231518  0.200118
0.182702  0.14609 0.14609
0.774963  0.541334  0.426258  0.347821  0.304244
0.283322  0.236249  0.236249
1.08477 0.765712  0.607068  0.502461  0.448397  0.422254
0.357756  0.357756
1.08477 1.02671 0.820976  0.69197 0.622233  0.597816
0.51937 0.51937
1.08477 1.32083 1.06628 0.90764 0.825681  0.787343  0.710623
0.710623
1.08477 1.32083 1.3325  1.14596 1.05355 1.0152  0.922805
0.922805];

a = [0
5
10
15
20
25
30
35
40
45];

m = [1.2
1.5
2
3
5
10
20
30]';

```

```

v_fail = 3072;
rho_fail = 1E-3;
time1 = 1000;

time = 1303;
c = 26029/110*2;
v1(1) = v_fail;
rho1(1) = rho_fail;

for n=time1:1:time
mach_meas = v1/300;
aoa_meas = ScopeOut_aoa_meas(n*10,2);
Cd_int = griddata(m,a,Cd,mach_meas,aoa_meas);
gamma = rho1*v1^2/c*Cd_int;
v1 = v1-gamma;
drho = -80/6300*rho1;
rho1 = rho1 - drho;

Velocity(n) = v1;
rho(n) = rho1;
end

Velocity(time)
rho(time)

```

Investigation 3: A ballistic re-entry trajectory on Mars

The perfect navigation 'algorithm' stores all locations on a specific Mach number and then extrapolates the parachute phase and final position using a quadratic regression. A selecting algorithm sorts out which deployment Mach number was used after the Monte Carlo batch is performed: The geographic positions are extracted using:

```

SimSensst.deploy_M_index_16 = find(ScopeOut_M(:,2)<1.6,1,'first');
SimSensst.m16_lat(i_mc,1) =
ScopeOut_GEOpos(SimSensst.deploy_M_index_16,2);
SimSensst.m16_long(i_mc,1) =
ScopeOut_GEOpos(SimSensst.deploy_M_index_16,3);
SimSensst.m16_alt(i_mc,1) =
ScopeOut_alt(SimSensst.deploy_M_index_16,2);
SimSensst.m16_chute(i_mc,1) = -9E-
06*ScopeOut_v_N_magn(SimSensst.deploy_M_index_16,2)^2 +
0.0317*ScopeOut_v_N_magn(SimSensst.deploy_M_index_16,2) - 6.262;
SimSensst.m16_long_fin(i_mc,1) = SimSensst.m16_long(i_mc,1) +
atan(
(sin(ScopeOut_heading(SimSensst.deploy_M_index_16,2)/180*pi)*SimSe
nsst.m16_chute(i_mc,1)) / 3393)*180/pi;
SimSensst.m16_lat_fin(i_mc,1) = SimSensst.m16_lat(i_mc,1) + atan(
(cos(ScopeOut_heading(SimSensst.deploy_M_index_16,2)/180*pi)*SimSe

```

```

SimSensst.deploy_M_index_23 = find(ScopeOut_M(:,2)<2.3,1,'first');
SimSensst.m23_lat(i_mc,1) =
ScopeOut_GEOpos(SimSensst.deploy_M_index_23,2);
SimSensst.m23_long(i_mc,1) =
ScopeOut_GEOpos(SimSensst.deploy_M_index_23,3);
SimSensst.m23_alt(i_mc,1) =
ScopeOut_alt(SimSensst.deploy_M_index_23,2);
SimSensst.m23_chute(i_mc,1) = -9E-
06*ScopeOut_v_N_magn(SimSensst.deploy_M_index_23,2)^2 +
0.0317*ScopeOut_v_N_magn(SimSensst.deploy_M_index_23,2) - 6.262;
SimSensst.m23_long_fin(i_mc,1) = SimSensst.m23_long(i_mc,1) +
atan(
(sin(ScopeOut_heading(SimSensst.deploy_M_index_23,2)/180*pi)*SimSe
nsst.m23_chute(i_mc,1)) / 3393)*180/pi;
SimSensst.m23_lat_fin(i_mc,1) = SimSensst.m23_lat(i_mc,1) + atan(
(cos(ScopeOut_heading(SimSensst.deploy_M_index_23,2)/180*pi)*SimSe
nsst.m23_chute(i_mc,1)) / 3393)*180/pi;

SimSensst.deploy_M_index_3 = find(ScopeOut_M(:,2)<3,1,'first');
SimSensst.m3_lat(i_mc,1) =
ScopeOut_GEOpos(SimSensst.deploy_M_index_3,2);
SimSensst.m3_long(i_mc,1) =
ScopeOut_GEOpos(SimSensst.deploy_M_index_3,3);
SimSensst.m3_alt(i_mc,1) =
ScopeOut_alt(SimSensst.deploy_M_index_3,2);
SimSensst.m3_chute(i_mc,1) = -9E-
06*ScopeOut_v_N_magn(SimSensst.deploy_M_index_3,2)^2 +
0.0317*ScopeOut_v_N_magn(SimSensst.deploy_M_index_3,2) - 6.262;
SimSensst.m3_long_fin(i_mc,1) = SimSensst.m3_long(i_mc,1) + atan(
(sin(ScopeOut_heading(SimSensst.deploy_M_index_3,2)/180*pi)*SimSen
sst.m3_chute(i_mc,1)) / 3393)*180/pi;
SimSensst.m3_lat_fin(i_mc,1) = SimSensst.m3_lat(i_mc,1) + atan(
(cos(ScopeOut_heading(SimSensst.deploy_M_index_3,2)/180*pi)*SimSen

```

After the Monte Carlo analysis is completed the following script will select the Mach number required for deployment. This is done by comparing the longitude. Plus or minus 0.05 deg is set as the criterion.

```

long_min = SimSensst.m16_long_fin;
lat_min = SimSensst.m16_lat_fin;
long_nom = SimSensst.m177_long_fin;
lat_nom = SimSensst.m177_lat_fin;
long_max = SimSensst.m3_long_fin;
lat_max = SimSensst.m3_lat_fin;

( (max(long_nom) - min(long_nom))^2 + (max(lat_nom) -
min(lat_nom))^2)^0.5;

% Selector
for i_mc = 1:1:i_mc
select_comp = long_nom(i_mc) - long_cor;
if select_comp < -0.05
    selector(i_mc,1) = 1;
elseif select_comp > 0.05
    selector(i_mc,1) = 3;
else
    selector(i_mc,1) = 2;
end

if selector(i_mc,1) == 1
    deploy_alt(i_mc,1) = SimSensst.m16_alt(i_mc,1);
    deploy_long(i_mc,1) = long_min(i_mc,1);
    deploy_lat(i_mc,1) = lat_min(i_mc,1);
elseif selector(i_mc,1) == 2
    deploy_alt(i_mc,1) = SimSensst.m177_alt(i_mc,1);
    deploy_long(i_mc,1) = long_nom(i_mc,1);
    deploy_lat(i_mc,1) = lat_nom(i_mc,1);
elseif selector(i_mc,1) == 3
    deploy_alt(i_mc,1) = SimSensst.m21_alt(i_mc,1);
    deploy_long(i_mc,1) = long_max(i_mc,1);
    deploy_lat(i_mc,1) = lat_max(i_mc,1);
end
end

```

For the Mars re-entry g-load correlations the same methodology is used as for the Earth ballistic re-entry investigation, but now four correlations are required, one for the downrange and three for the 3 Mach estimations. The parachute phase trajectory are again modeled using the same quadratic regression.

```

% 0.3g time
SimSensst.g03_index =
find(ScopeOut_gloads_tot(:,2)>0.3,1,'first');
SimSensst.g03_trigger_time(i_mc,1) =
ScopeOut_M(SimSensst.g03_index);
% 3g time
SimSensst.g3_index = find(ScopeOut_gloads_tot(:,2)>3,1,'first');
SimSensst.g3_trigger_time(i_mc,1) =
ScopeOut_M(SimSensst.g3_index);
% 1g time
SimSensst.g1_index = find(ScopeOut_gloads_tot(:,2)>1,1,'last');
SimSensst.g1_trigger_time2(i_mc,1) =
ScopeOut_M(SimSensst.g1_index);
% 2g time
SimSensst.g2_index = find(ScopeOut_gloads_tot(:,2)>2,1,'last');
SimSensst.g2_trigger_time2(i_mc,1) =
ScopeOut_M(SimSensst.g2_index);
% 3g time
SimSensst.g3_index = find(ScopeOut_gloads_tot(:,2)>3,1,'last');
SimSensst.g3_trigger_time2(i_mc,1) =
ScopeOut_M(SimSensst.g3_index);
% 4g time
SimSensst.g4_index = find(ScopeOut_gloads_tot(:,2)>4,1,'last');
SimSensst.g4_trigger_time2(i_mc,1) =
ScopeOut_M(SimSensst.g4_index);

```

```

% Mach 1.6 deployment
m16_meas = SimSensst.g1_trigger_time2(i_mc,1) -
SimSensst.g3_trigger_time2(i_mc,1);
% m16 = 1.1601*m16_meas + 29.94; % viking chute correlation
m16 = 1.1542*m16_meas + 30.409;
m16_index = find( SimOut_time(:,1) >
(SimSensst.g4_trigger_time2(i_mc,1) + m16), 1,'first')-1;
m16_deploy_m(i_mc,1) = ScopeOut_M(m16_index,2);
m16_deploy_alt(i_mc,1) = ScopeOut_alt(m16_index,2);
m16_deploy_qbar(i_mc,1) = ScopeOut_qbar(m16_index,2);
m16_deploy_long(i_mc,1) = ScopeOut_GEOpos(m16_index,3);
m16_deploy_lat(i_mc,1) = ScopeOut_GEOpos(m16_index,2);
m16_dr_chute(i_mc,1) = -9E-06*ScopeOut_v_N_magn(m16_index,2)^2 +
0.0317*ScopeOut_v_N_magn(m16_index,2) - 6.262;
m16_long_fin(i_mc,1) = m16_deploy_long(i_mc,1) + atan(
(sin(ScopeOut_heading(m16_index,2)/180*pi)*m16_dr_chute(i_mc,1)) /
3393)*180/pi;
m16_lat_fin(i_mc,1) = m16_deploy_lat(i_mc,1) + atan(
(cos(ScopeOut_heading(m16_index,2)/180*pi)*m16_dr_chute(i_mc,1)) /
3393)*180/pi;

```

```

% Mach 2.3 deployment
m23_meas = SimSensst.g2_trigger_time2(i_mc,1)-
SimSensst.g3_trigger_time2(i_mc,1);
% m23 = 1.8499*m23_meas + 57.372; % viking chute
m23 = 1.9804*m23_meas + 37.973;
m23_index = find( SimOut_time(:,1) >
(SimSensst.g4_trigger_time2(i_mc,1) + m23), 1, 'first')-1;
m23_deploy_m(i_mc,1) = ScopeOut_M(m23_index,2);
m23_deploy_alt(i_mc,1) = ScopeOut_alt(m23_index,2);
m23_deploy_qbar(i_mc,1) = ScopeOut_qbar(m23_index,2);
m23_deploy_long(i_mc,1) = ScopeOut_GEOpos(m23_index,3);
m23_deploy_lat(i_mc,1) = ScopeOut_GEOpos(m23_index,2);
m23_dr_chute(i_mc,1) = -9E-06*ScopeOut_v_N_magn(m23_index,2)^2 +
0.0317*ScopeOut_v_N_magn(m23_index,2) - 6.262;
m23_long_fin(i_mc,1) = m23_deploy_long(i_mc,1) + atan(
(sin(ScopeOut_heading(m23_index,2)/180*pi)*m23_dr_chute(i_mc,1)) /
3393)*180/pi;
m23_lat_fin(i_mc,1) = m23_deploy_lat(i_mc,1) + atan(
(cos(ScopeOut_heading(m23_index,2)/180*pi)*m23_dr_chute(i_mc,1)) /
3393)*180/pi;

```

```

% Mach 3 deployment
m3_meas = SimSensst.g2_trigger_time2(i_mc,1)-
SimSensst.g3_trigger_time2(i_mc,1);
% m3 = 1.9246*m3_meas + 44.745; % viking chute
m3 = 2.0548*m3_meas + 20.479;
m3_index = find( SimOut_time(:,1) >
(SimSensst.g4_trigger_time2(i_mc,1) + m3), 1, 'first')-1;
m3_deploy_m(i_mc,1) = ScopeOut_M(m3_index,2);
m3_deploy_alt(i_mc,1) = ScopeOut_alt(m3_index,2);
m3_deploy_qbar(i_mc,1) = ScopeOut_qbar(m3_index,2);
m3_deploy_long(i_mc,1) = ScopeOut_GEOpos(m3_index,3);
m3_deploy_lat(i_mc,1) = ScopeOut_GEOpos(m3_index,2);
m3_dr_chute(i_mc,1) = -9E-06*ScopeOut_v_N_magn(m3_index,2)^2 +
0.0317*ScopeOut_v_N_magn(m3_index,2) - 6.262;
m3_long_fin(i_mc,1) = m3_deploy_long(i_mc,1) + atan(
(sin(ScopeOut_heading(m3_index,2)/180*pi)*m3_dr_chute(i_mc,1)) /
3393)*180/pi;
m3_lat_fin(i_mc,1) = m3_deploy_lat(i_mc,1) + atan(
(cos(ScopeOut_heading(m3_index,2)/180*pi)*m3_dr_chute(i_mc,1)) /
3393)*180/pi;

```

The selection algorithm is based on the downrange. The downrange was correlated to the g-loads. The script provided was used after the Monte Carlo batch in order to optimize the downrange criteria, in this case 818 and 824 Km. However also a script was made to make the control decision during the Monte Carlo simulations. Deployment below 818 Km would be at Mach 1.6, between 818 and 824 at Mach 2.3 and Above 824 at Mach 3.

```

% Selector
select_comp = (SimSensst.g3_trigger_time(i_mc,1) -
SimSensst.g03_trigger_time(i_mc,1))*3.3535 + 499.2;
if select_comp < 818
    selector(i_mc,1) = 1;
elseif select_comp > 824
    selector(i_mc,1) = 3;
else
    selector(i_mc,1) = 2;
end

if selector(i_mc,1) == 1
    deploy_alt(i_mc,1) = m16_deploy_alt(i_mc,1);
    deploy_qbar(i_mc,1) = m16_deploy_qbar(i_mc,1);
    deploy_m(i_mc,1) = m16_deploy_m(i_mc,1);
    deploy_long(i_mc,1) = m16_long_fin(i_mc,1);
    deploy_lat(i_mc,1) = m16_lat_fin(i_mc,1);
elseif selector(i_mc,1) == 2
    deploy_alt(i_mc,1) = m23_deploy_alt(i_mc,1);
    deploy_qbar(i_mc,1) = m23_deploy_qbar(i_mc,1);
    deploy_m(i_mc,1) = m23_deploy_m(i_mc,1);
    deploy_long(i_mc,1) = m23_long_fin(i_mc,1);
    deploy_lat(i_mc,1) = m23_lat_fin(i_mc,1);
elseif selector(i_mc,1) == 3
    deploy_alt(i_mc,1) = m3_deploy_alt(i_mc,1);
    deploy_qbar(i_mc,1) = m3_deploy_qbar(i_mc,1);
    deploy_m(i_mc,1) = m3_deploy_m(i_mc,1);
    deploy_long(i_mc,1) = m3_long_fin(i_mc,1);
    deploy_lat(i_mc,1) = m3_lat_fin(i_mc,1);
end

```

After all the geographic locations are stored, the data is post processed. For the generation of the ellipse, the “makeellipse” script was converted from FORTRAN code and the “ellipse” drawing script was taken from the Mathworks website.

```

% Spirit
long_cor = 175.6724;
lat_cor = -14.6391;
% oppertunity
long_cor = -5.5121;
lat_cor = -1.9774;

NASA_long = sin((175.47848)/180*pi)*3393;
NASA_lat = sin((-14.571892)/180*pi)*3393;

long_min = SimSensst.m16_long_fin;
lat_min = SimSensst.m16_lat_fin;
long_nom = SimSensst.m177_long_fin;
lat_nom = SimSensst.m177_lat_fin;
long_max = SimSensst.m3_long_fin;
lat_max = SimSensst.m3_lat_fin;

hold all
scatter(long_nom,lat_nom,'filled')
axis equal
xlabel('Longitude [deg]')
ylabel('Latitude [deg]')
scatter(deploy_long,deploy_lat,'filled')
el1 = makeellipse(long_nom,lat_nom,0.99);
el2 = makeellipse(deploy_long,deploy_lat,0.9973);
ellipse(el1(1,1),el1(1,2),el1(1,3),el1(1,4),el1(1,5))
ellipse(el2(1,1),el2(1,2),el2(1,3),el2(1,4),el2(1,5))

% scatter(175.47848, -14.571892,'filled') % actual Spirit
% scatter(175.3, -14.59,'filled') % nasa target
% scatter(175.801,-14.603,'r','filled') % nominal
% scatter(354.47417-360, -1.948282,'filled') % actual Oppertunity
% scatter(-5.4356, -1.9716,'filled') % nominal oppertunity
% scatter(354.23-360,-1.98,'filled') % Nasa dispersion center
axis equal
hold off

```